Julius-Maximilians-
UNIVERSITÄT
WÜRZBURG

Numerical simulations on limitations and optimization strategies of organic solar cells

Dissertation zur Erlangung des
naturwissenschaftlichen Doktorgrades
der Bayerischen Julius-Maximilians-Universität Würzburg

vorgelegt von
Alexander Johannes Wagenpfahl
aus
Würzburg

Würzburg 2013

Eingereicht am 24. Juni 2013
bei der Fakultät für Physik und Astronomie

1. Gutachter: Prof. Dr. Vladimir Dyakonov
2. Gutachter: Prof. Dr. Jean Geurts
der Dissertation.

1. Prüfer: Prof. Dr. Vladimir Dyakonov
2. Prüfer: Prof. Dr. Jean Geurts
3. Prüfer: Prof. Dr. Karl Mannheim
im Promotionskolloquium.

Tag des Promotionskolloquiums: 20. Dezember 2013

Doktorurkunde ausgehändigt am:

Contents

1. Introduction

Continuously increasing energy prices have considerably influenced the cost of living over the last decades. At the same time increasingly extreme weather conditions, drought-filled summers as well as autumns and winters with heavier rainfall and worsening storms have been reported. These are possibly the harbingers of the expected approaching global climate change. Considering the depletability of fossil energy sources and a rising distrust in nuclear power, investigations into new and innovative renewable energy sources are necessary to prepare for the coming future.

In addition to wind, hydro and biomass technologies, electricity generated by the direct conversion of incident sunlight is one of the most promising approaches. Up to 43.5 % of all incoming photons are converted into electric power in top performing state-of-the-art multi stacked inorganic concentrator solar cells [1]. Despite their high efficiency, these devices generally require complex and laborious production processes that limit their suitability to high-end applications. Standard single-layered inorganic roof-top solar cell panels offer power conversion efficiencies of approximately up to 23.5 % at more moderate prices [1].

Since the syntheses and detailed studies of organic semiconducting polymers were intensified in the early seventies, with fullerenes becoming of greater interest in the mid-eighties, a new kind of solar cell fabrication became conceivable [2–4]. In addition to classical vacuum deposition techniques, organic cells were now also able to be processed from a solution, even on flexible substrates like plastic, fabric or paper [5–7]. To date, power conversion efficiencies of up to 10 % have been reached showing a steadily increasing trend [1, 8].

In comparison to highly efficient solar cell technologies based on silicon (Si) or gallium arsenide (GaAs) for instance, organic semiconductors suffer from charge carrier mobilities orders of magnitudes lower than in inorganics [9]. This is caused mainly by the high disorder accompanied by a higher number of trap states in organic active layers. The light absorption capability of organics is however superior. Active layers of about 100 nm and below are already sufficient to absorb most of the incident light. Thus, for usage as solar cells, more charge carriers have to be transported over shorter distances in organic solar cells making them a serious competitor to inorganic technologies.

An organic solar cell represents a complex electrical device influenced for instance by light interference for charge carrier generation. Also charge carrier recombination and transport mechanisms are important to its performance. Charge carriers are also injected from metal electrodes into the semiconductor. In accordance to Coulomb interaction, this results in a specific distribution of the charge carriers and the electric field, which finally yield the measured current–voltage characteristics. Changes of certain parameters result in a complex response in the investigated device due to interactions between the physical processes. Consequently, it was necessary to find a way to generally predict the response of such a device to temperature changes for example.

In this work, a numerical, one-dimensional simulation has been developed based on the drift–diffusion equations for electrons, holes and excitons. The generation and recombination rates of the single species are defined according to a detailed balance approach. The Coulomb interaction between the single charge carriers is considered through the Poisson equation. An analytically non-solvable differential equation system is consequently set-up. With numerical approaches, valid solutions describing the macroscopic processes in organic solar cells can be found. An additional optical simulation is used to determine the spatially resolved charge carrier generation rates due to interference.

Concepts regarding organic semiconductors and solar cells are introduced within Chap. 2 to 4 of this work. All chapters are based on previous ones and logically outline the basic physics, device architectures, models of charge carrier generation and recombination as well as the mathematic and numerical approaches to obtain valid simulation results.

Beginning in Chap. 5, the simulation is used to elaborate issues of current interest in organic solar cell research. This includes a basic understanding of how the open circuit voltage is generated and which processes limit its value. S-shaped current–voltage characteristics are explained assigning finite surface recombination velocities at metal electrodes piling-up local space charges (Chap. 6). The power conversion efficiency is identified as a trade-off with charge carrier extraction, leading to high extracted currents and charge accumulation enhancing the open circuit voltage (Chap. 7). Differences between recombination rates determined by different interpretations of identical experimental results are assigned to a spatially inhomogeneous recombination, relevant for all low mobility semiconductor devices (Chap. 8).

Part I.

Theory

2. Organic photovolatics

The use of organic semiconductors in solar cells represents a relatively new concept in comparison to more well established inorganic photovoltaic (PV) technologies. Instead of well-ordered crystalline structures as used in most solar cells, active layers of organic devices often consist of randomly arranged molecules. This disorder influences the charge carrier transport and facilitates innovative device architectures such as bulk heterojunction solar cells. Models of charge transport in organic semiconductors as well as possible organic solar cell architecture are introduced in this chapter.

2.1. Organic semiconductors

Organic semiconductors have been known and studied for about 100 years. In more recent years, a strong focus on organic semiconductors and photovolatics could be observed. From the first detailed investigation of the electrical conductivity of doped Polyacetylene for instance [2], a broad scientific field was developed which was awarded the Nobel Prize in Chemistry in 2000. Today, a huge variety of semiconducting organic compounds are known and studied [8].

Organic semiconductors gained economic importance mainly through their application in organic light emitting diodes (OLEDs) for display applications. Their excellent light absorbing properties however were also observed. The majority of incident photons can be absorbed by relatively thin films of approximately 100 nm [10]. This inspired the idea that solar cells could be created out of organic semiconductors.

The currently available organic semiconductors can be separated roughly into two different classes. Small molecules are compounds of a certain, discrete size with a generally poor solubility. A thermal evaporation is therefore often required upon processing. In contrast, fullerenes with chemically attached side groups and conjugated polymers based on periodic sequences of monomers are processable out of solution. Large substrate areas can be coated by spin coating, a doctor blade or other roll-to-roll-printing techniques. A future inexpensive, large scale production of organic solar cells therefore seems to be feasible [11]. The first commercial products are already available on today's market.

The electrical conductivity of organic semiconductors is based on conjugated double bonds between carbon atoms as illustrated in Fig. 2.1. The carbon atoms along the structure are sp^2-hybridized and offer three σ-bonds to their neighboring atoms. Under ideal conditions, they form binding angles of 120 degrees in the plane [9]. The remaining p_z-orbitals arrange perpendicularly to this plane. A π-bond is created by the overlap of two adjacent p_z-orbitals. A chain of sp^2-hybridized carbon atoms will result in a periodic sequence of single and double bound carbon atoms according to Peierls' theorem since each p_z-orbital contributes one valence electron [12]. Current transport in this simplified picture is established by turning a double bond to the next single bond.

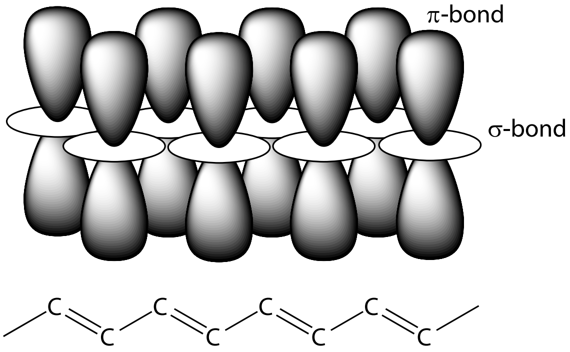

Figure 2.1.: (top) Schematic of p_z-orbitals from a sequence of sp^2-hybridized carbon atoms of Polyacetylene. (bottom) Corresponding structural formula neglecting adjacent hydrogen atoms. A conjugated system is created by overlapping p_z-orbitals.

This explanation has to be improved in terms of quantum mechanics. In inorganic semiconductors, such as silicon or gallium arsenide, the highly ordered crystal structure generates a periodic atomic core potential. Fourier transformed and inserted into the steady state Schrödinger equation, this results in one-dimensional periodic Bloch-waves in reciprocal space. Bloch-waves describe the probabilities of presence of delocalized quasi-free valence electrons. Two independent solutions are obtained by the interference of a Bloch-wave with its own Bragg-reflection. One solution corresponds to a localization of charge carriers between the lattice atoms and represents a strong chemical bond with an enhanced binding energy. Conversely, the second solution shows a high probability of presence of the electrons next to the atom cores. These bonds are energetically weakened. For a system containing many valence electrons, the sum of all enhanced and reduced binding energies defines the charge transport bands. An energy band gap E_g lacking of available states is generated between both bands. The higher energy band is termed the conduction band, in contrast to the lower valence band. Electrons are thermally excited from the valence into the conduction band. The electrons in the conduction band as well as the remaining holes in the valence band are mobile and participate in the current flow. The Fermi energy E_F denotes the highest energy an electron can possess at $T = 0$ K. For an undoped semiconductor this energy is located approximately in the middle of the energy gap [13].

The Bloch formalism is however hardly applicable to conjugated polymers due to the less distinct lattice periodicity. An example of such a polymer is Polyacetylene which is shown in Fig. 2.1. A commonly mentioned but still one-dimensional approach explaining the semiconductive properties of polymers is the extension of the Bloch formalism to a repeating base of two carbon atoms. This corresponds to the periodic sequence of single and double bonds in conjugated polymer chains. Two solutions with different binding energies are obtained in analogy to the Bloch formalism. Interpreted in terms of the electron probability of presence, the result implies spatially shorter binding distances between double bonded carbon atoms and longer distances between single bonded partners. These Peierls distortions are attributed to be the origin of the semiconductive property of conjugated systems in the classic concept [9]. The charge carriers are delocalized within the conjugation length which denotes the segment of a polymeric semiconductor without defect.

Since all organic semiconductors are at least 2-dimensonal compounds, more complex models are required for an accurate description of their semiconductive properties. A commonly made assumption for calculating individual molecules is the localization of valence electrons to their corresponding atomic cores. The overlapping, quasi-bound valence electron wave functions can be added in terms of the linear combination of atomic orbitals (LCAO) model. The effective yielded molecular orbitals result in an energy level splitting. Orbitals on which electrons are located between atomic cores stabilize the molecular structure and are called binding orbitals. Conversely, anti-binding orbitals with a high charge carrier probability of presence next to the atom cores destabilize the molecular structure. Since for conjugated carbon compounds each atom contributes one valence electron to the delocalized π-bond system, all binding orbitals are usually filled while anti-binding molecular orbitals are vacant. The lowest unoccupied molecular orbital is abbreviated as the LUMO, the highest occupied one as the HOMO. In addition to the LCAO method, other mathematical models such as the Heitler–London approximation or the density functional theory exist. The latter is particularly interesting when considering the influence of excess charge carriers on molecules. Due to Coulomb interactions of such charges with the molecule, the molecule is distorted and binding energies are changed. The term polarons is often used here instead of electrons and holes, alluding to this correlation. Polarons and the term electron (or hole) is used synonymously whenever charge carriers on organic semiconductors are denoted.

Adjacent molecules attract one another due to Van-der-Waals interaction which leads to a locally ordered structure denoted as π-stacking. The p_z orbitals weakly overlap due to the spatial proximity of the molecules and an intermolecular charge transport is made possible. Even though the π-stacking facilitates charge transport, it is not necessarily required for an intermolecular charge transport.

Organic semiconductors for solar cell applications are shown in Fig. 2.2. As a standard material system, the polymer P3HT and the $PC_{61}BM$ fullerene have been widely investigated. Other examples are PCDTBT and $PC_{71}BM$ or combinations of small molecules such as CuPc and C_{60}. The full chemical names of these organic compounds can be found in the caption of Fig. 2.2.

2.2. Charge transport in disordered solids

Layers of organic semiconductors possess more complex physical properties than single atoms or molecules. For most inorganic semiconductors, the current transport is based on delocalized charge carriers. The charge carrier mobility μ is defined as the proportionality factor between an applied electric field F and the yielded charge carrier velocity v_d,

$$v_d = \mu F. \tag{2.1}$$

The mobility in inorganic semiconductors is expected to be relatively high in comparison with more disordered organic semiconductors. In inorganic semiconductors, the mobility is limited by scattering of charge carriers with ionized impurities for low temperatures ($\mu \propto T^{3/2}$) or by phonon scattering at higher temperatures ($\mu \propto T^{-3/2}$) [13].

In organic solar cells, many individual organic molecules are combined to form a solid. The molecules either create a highly ordered organic crystal with material properties compa-

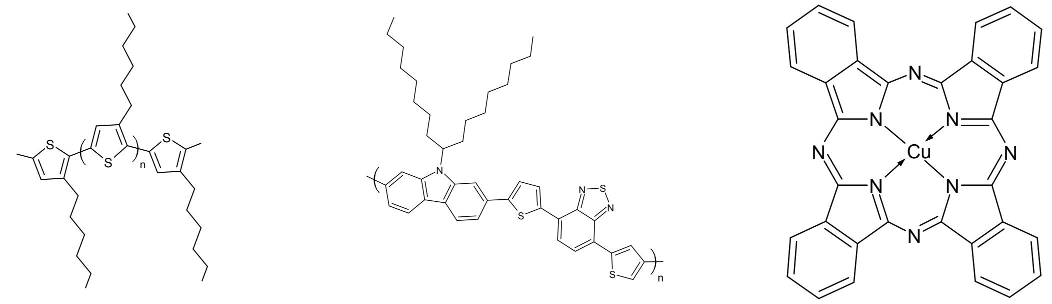

(a) P3HT (b) PCDTBT (c) CuPc

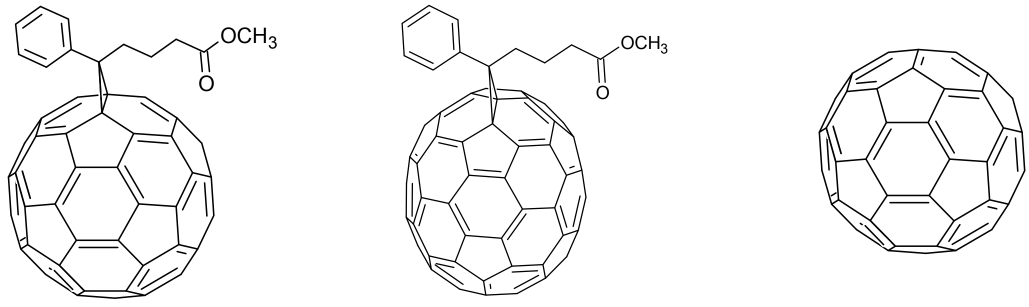

(d) $PC_{61}BM$ (e) $PC_{71}BM$ (f) C_{60}

Figure 2.2.: Examples of organic semiconductors. Electron donors are given by (a), (b), and (c), acceptors by (d), (e) and (f). The small molecules (c) CuPc and (f) C_{60} need to be evaporated upon processing. The names of the compound are (a) Poly(3-hexylthiophene-2,5-diyl), (b) Poly[[9-(1-octylnonyl)-9H-carbazole-2,7-diyl]-2,5-thiophenediyl-2,1,3-benzothiadiazole-4,7-diyl-2,5-thiophenediyl], (c) copper phthalocyanine, (d) [6,6]-phenyl C_{61} butyric acid methyl ester, (e) [6,6]-phenyl C_{71} butyric acid methyl ester, and (f) C_{60}.

rable to crystalline inorganic semiconductors, or they form a disordered solid with randomly arranged molecules. The arrangement of the molecules, especially in the latter case strongly depends on the processing conditions of the active layer. The density of states of such solids is defined by the sum of all available states for electrons and holes. The resulting energy bands are denoted as the LUMO and HOMO in contrast to the conduction and valence band of inorganic semiconductors. In terms of device physics, these bands and not the orbitals of individual molecules are termed. The formation of such a density of state distribution is illustrated in Fig. 2.3.

Semiconductors with high disorder possess an also high amount of spatially and energetically localized states. Gaussian shapes of the HOMO and LUMO energies are commonly expected due to this disorder [14]. Charge carriers reside on the localized states which are continuously being rearranged by vibronic excitations. The charge transport in disordered organic materials is therefore mediated by a strong electron–phonon interaction [9]. Only in exceptional cases where the critical density of states has exceeded a critical value, delocalized states are formed over the entire extent of the device [15].

Many investigations and models on the charge transport have been presented since the early days of organic semiconductor research. In 1956, Marcus et al. proposed a theoretical model dealing with a tunnel transport of charge carriers from one localized energy state E_i to another E_j [16]. For such a variable-range hopping (VRH) model, the overlap between two wave functions had to be considered in terms of a transfer integral. Based on this model, a temperature activated tunnel transport between energetically and spatially discrete states is expected [9, 17–19].

In 1960, Miller and Abrahams presented an extended model of the phonon stimulated tunneling charge carrier transport [20, 21]. According to their simplified master equation,

$$\nu_{ij}\left(E_i,E_j,R_{ij}\right) = \nu_0 \exp\left(-2\gamma R_{ij}\right) \begin{cases} \exp\left(-\frac{E_j-E_i}{k_B T}\right) & E_j > E_i \\ 1 & E_j < E_i, \end{cases} \tag{2.2}$$

two fundamental cases have to be distinguished in order to determine the transition rate ν_{ij} between two sites. If the initial state E_i is energetically situated below the target state E_j, thermal energy is required to stimulate a charge transfer. This is described by the Boltzmann factor. The Boltzmann constant k_B and the temperature T are required as parameters. Conversely, a transition is enabled without any restriction if the target state is energetically located below the initial state. The spatial distance between both states R_{ij} needs to be overcome by absorption or emission of phonons described by the „attempt-to-escape frequency“ ν_0. The actual tunnel transport is represented by the inverse localization radius γ, a parameter proportional to the transfer integral. The charge transport in organic semiconductors is therefore defined as a thermally activated tunnel process by the Miller–Abrahams equation. The consequences of this hitherto used model have been explicitly studied [14, 22–24].

A simple analytical expression for the charge carrier transport cannot be calculated simply due to the discrete form of Eqn. (2.2). A Gaussian shaped density of states (GDOS) is often assumed for organic semiconductors because of the statistical nature of disorder. In 1993, Bässler combined the Miller–Abrahams equation (Eqn. (2.2)) with such a Gaussian distribution $g(E)$ [14]. It is defined by

$$g(E) = \frac{N_t}{\sqrt{2\pi\sigma}} \exp\left(-\left[\frac{E-\mu_o}{2\sigma}\right]^2\right). \tag{2.3}$$

The parameters required are the effective density of states N_t, the width of the distribution σ and the location of the maximum amplitude μ_o. This approach is commonly known as the Gaussian disorder model (GDM). An empirical analytical solution of the charge carrier mobility was found by Monte–Carlo simulations,

$$\mu = \mu_0 \exp\left(-\left[\frac{2\sigma}{3k_B T}\right]^2\right) \begin{cases} \exp\left(C\left[\left(\frac{\sigma}{k_B T}\right) - \Sigma^2\right]\sqrt{F}\right), & \Sigma > 1.5, \\ \exp\left(C\left[\left(\frac{\sigma}{k_B T}\right) - 2.25\right]\sqrt{F}\right), & \Sigma < 1.5. \end{cases} \tag{2.4}$$

In terms of disorder, σ is also called the (energy) disorder parameter. In addition, a spatial disorder parameter Σ, a constant scaling factor C and a mobility prefactor μ_0 were introduced [14]. Today, the GDM model is commonly used to describe the temperature dependence of charge carrier mobility in organic semiconductors. The transport of a charge generated by light within the GDM model is schematically depicted in Fig. 2.3. Hopping sites are not correlated in the GDM model. The electric field dependence of Eqn. (2.4) is

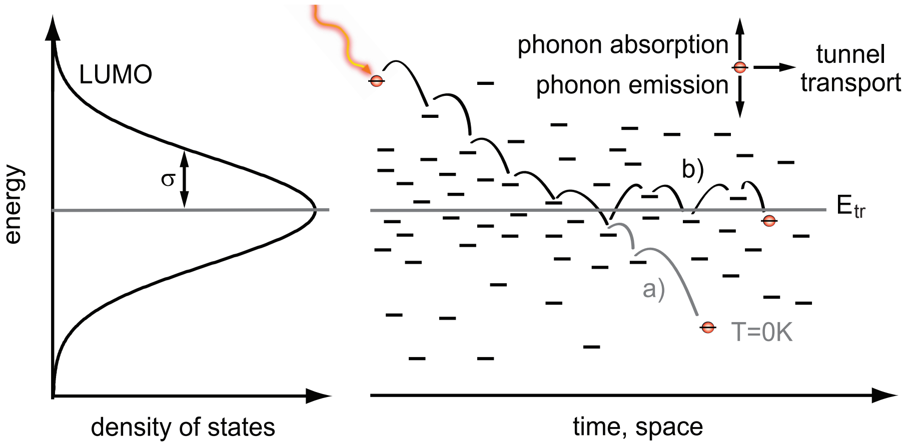

Figure 2.3.: In the GDM model the discrete energy states are Gaussian distributed around a maximum defined by the disorder parameter σ. For simplicity's sake, the maximum was set equal to the transport energy E_{tr}. A charge carrier generated by light relaxes due to phonon assisted tunneling according to Eqn. (2.2). All charge carriers relax to the lowest available energetic state (a) at $T = 0$ K. At a higher temperature (b), a detailed balance between relaxation and thermal activation is established. In the MTR model, this equilibrium energy is denoted as transport energy E_{tr}.

often neglected in practical applications. The charge carrier mobility equation is therefore simplified to

$$\mu = \mu_0 \exp\left(- \left[\frac{2\sigma}{3k_B T} \right]^2 \right). \tag{2.5}$$

The GDM model predicts an exponential dependence of the charge carrier mobility on temperature which is in agreement with experimental findings [25].

By 2005, experiments had shown charge carrier density dependent mobilities as well as a high density of immobile charge carriers in amorphous organic semiconductors [26]. Thus, the transport edge concept, known from inorganic semiconductors [27], was added to the GDM model [22, 28, 29]. The result is known as the multiple trapping and release (MTR) model.

Charge carriers in this model are transported in the LUMO and HOMO bands. Excited charge carriers thermalize by hopping to the lowest available energetic state at $T = 0$ K as illustrated in Fig. 2.3(a). At higher temperatures (Fig. 2.3(b)), charge carriers are additionally thermally excited according to Eqn. (2.2). The energy at which the probability that a charge carrier will thermalize to a lower state is identical to the probability of thermal excitation is denoted as transport energy E_{tr} [30].

The MTR model allows charge carriers located in states below and above the transport energy to be distinguished from one another. Charge carriers on states below E_{tr} are assumed to be currently trapped as long as they are not thermally excited over the transport energy. Conversely, charge carriers above E_{tr} are interpreted as being mobile and delocalized over the whole active layer. A charge carrier can change between being mobile and being trapped by capture and release events. This kind of charge transport is shown in Fig. 2.4. The consequences of the MTR model are of crucial importance to simulating organic solar cells as two major implications can be concluded.

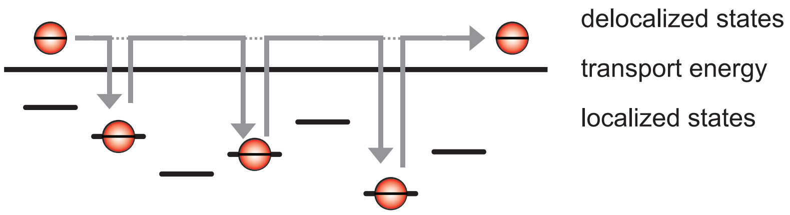

Figure 2.4.: In terms of the MTR model, charges below the transport energy are assumed to be trapped in localized states. Charges above the transport energy are interpreted as being delocalized, thus, mobile. A current transport is accompanied by multiple capture and release events of the charge carriers.

First, not all charge carriers are able to contribute to an electric current. An adjacent unoccupied state is always required for a charge transfer. A charge carrier is therefore permanently trapped in a tail state if no unoccupied state is in reach of thermal activation or thermalization to a lower state. In contrast to the GDM model, this correlation of the electrons in the MTR model defines a share of immobile charge carriers. The difference between both models is schematically summarized in Fig. 2.5. The ratio between conductive and deeply trapped charges ϑ can be calculated by a detailed balance approach [31, 32]. The total charge carrier density n is therefore split into conductive n_c and trapped n_t shares,

$$n = n_c + n_t = \frac{n_c}{\vartheta}. \tag{2.6}$$

Second, all conductive charge carriers above the transport energy are assumed to be delocalized. This enables the application of the charge carrier band transport equations derived for crystalline, inorganic semiconductors [13]. These well-studied equations enable fast and accurate numerical calculations in order to predict the electrical properties of organic solar cells [33].

The transport of charge carriers in organic solar cells is generally described by the simplified Boltzmann transport equations [9]. If charge transport by thermal gradients is neglected, the resulting drift–diffusion equations for electron n and hole p charge carrier densities read,

$$J_n = qn\mu_n F + qD_n \frac{\partial n}{\partial x} \tag{2.7}$$

$$J_p = qp\mu_n F - qD_p \frac{\partial p}{\partial x}. \tag{2.8}$$

The current densities of electrons J_n and holes J_p are generated by two contributions. Either charge carriers follow an electric field F which defines a drift current, or a diffusive current is generated by the compensation of charge carrier gradients $\partial n/\partial x$, $\partial p/\partial x$. The drift current is defined by the charge carrier mobilities of electrons μ_n and holes μ_p. The diffusion constants

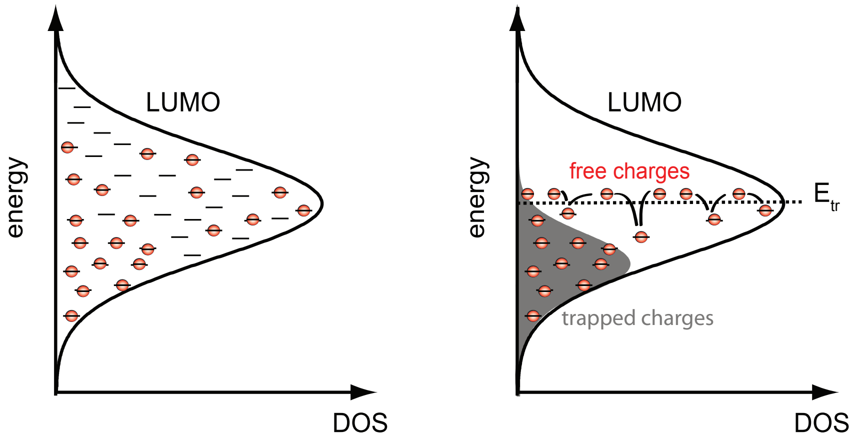

(a) GDM model (b) MTR model

Figure 2.5.: Comparison between the GDM and the MTR model. In the GDM model (a), the hopping of charge carriers is calculated independently of other charge carriers. Adjacent states are assumed to be unoccupied, thus, all charge carriers are mobile. The MTR model (b) considers multiple electrons simultaneously. All mobile charge carriers are effectively transported at the transport energy E_{tr}. A share of charge carriers is permanently trapped due to the absence of free adjacent states.

D_n and holes D_p are given by the Einstein equations [34],

$$D_n = \mu_n \cdot \frac{k_B T}{q}, \quad D_p = \mu_p \cdot \frac{k_B T}{q}. \tag{2.9}$$

The drift–diffusion equations describe solely the transport of mobile charge carriers. This implies that charge carrier mobility is defined only for free charge carriers. An alternative description is possible due to the linearity of the drift–diffusion equation with mobility. Thus, the total charge carrier density can also be inserted into the drift–diffusion equation if an effective mobility is used. This effective mobility is the average mobility of all charge carriers located in the semiconductor. Both representations are equivalent in terms of the MTR model [30].

The MTR model is not restricted to a specific shape of the density of state distribution. Even though absorption measurements show Gaussian density of states [35], exponential DOS distributions are also in use [36–38]. A detailed overview of the different charge transport models can be found in Ref. [39].

2.3. Organic solar cell architectures

Despite the fact that organic semiconductors have been known of since the early seventies, the initial idea of using solution processed organic semiconductors in solar cells came up in 1992 when semiconducting polymers and fullerenes were blended to observe light absorption by photogenerated charge carriers [4, 40]. During these experiments, a charge transfer from polymer to fullerene molecules was observed.

Absorbed photons generate Coulomb-bound pairs of polarons (electron and hole) on the organic molecules with binding energies of about 0.3 to 0.5 eV, denoted as excitons [41, 42]. The relatively high binding energies originate from the low relative dielectric permittivity ε_r of organic compounds of about 3 to 4 [43, 44]. From various investigations, exciton lifetimes in the nanosecond time regime are reported [4]. The excitons can be separated into free charge carriers which are then transported to the electrodes of the solar cell. Such a device can be designed either as a planar or as a bulk heterojunction solar cell.

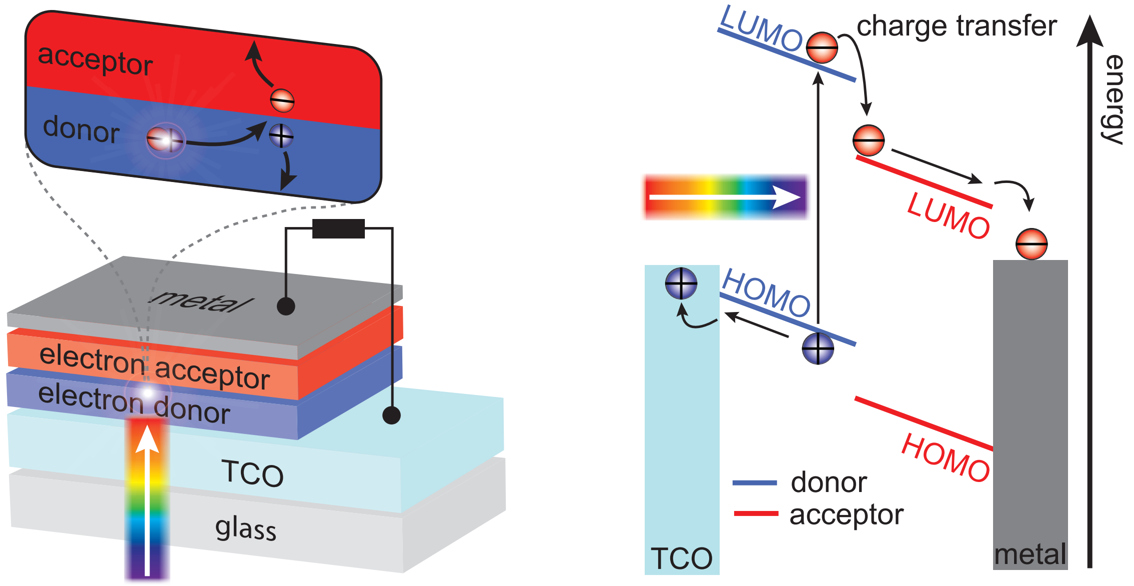

(a) PHJ device layout

(b) PHJ energy structure at short circuit

Figure 2.6.: The planar heterojunction (PHJ) solar cell is based on two neat semiconductor layers sandwiched between two metallic electrodes. Excitons are generated by light and diffuse within the pure phases. If excitons reach the heterointerface within their lifetime, they are separated. The generated polarons are subsequently transported to the electrodes.

For a planar heterojunction (PHJ) solar cell, two layers of pure semiconductors are stacked as shown in Fig. 2.6 (a). Excitons are created and diffuse in both layers. In order to create a working device, the LUMO and HOMO energies of both semiconductors must offer an energetic advantage to transfer either one of the charge carriers of the exciton to the other semiconductor. Such a case is shown in Fig. 2.6 (b). The semiconductor on which the electron is located after the separation process is denoted as the (electron) acceptor whereas the other is called the donor. The charge transfer is completed on a femtosecond time scale [4].

A weaker but still Coulomb-bound quasi-particle is created after the charge transfer. Electron and hole polaron of these polaron pairs are located on different molecules. This state is also denoted as charge transfer (CT) complex [45, 46]. Polaron pairs can be further separated into free polarons by an electric field or by residual energy from the exciton separation [47–49]. However, a direct generation of polarons from excitons was also observed, possibly without the intermediate polaron pair state [50, 51].

The required electric field is generated by two electrodes with different work functions. Highly doped transparent conducting oxides (TCOs) with low work functions such as indium tin oxide (ITO) are usually used as transparent anodes. Evaporated metals with higher work functions such as silver or aluminum are used as cathodes. An electric field is established in the active layers if a load is applied or both contacts are short-circuited. Such a short circuit is shown in Fig. 2.6 (b).

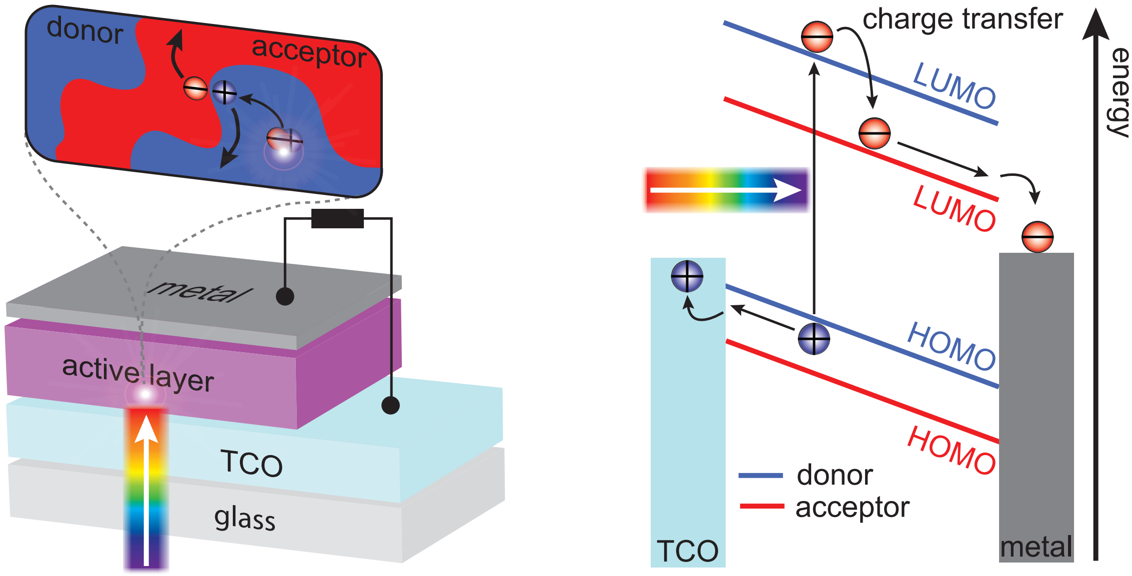

(a) BHJ device layout (b) BHJ energy structure at short circuit

Figure 2.7.: A bulk heterojunction (BHJ) solar cell consists of only one blended active layer. The blend is made from donor and acceptor molecules in an arbitrary arrangement forming an interpenetrating network of acceptor and donor molecules. Light absorption and exciton separation are made possible at every location throughout the active layer. Free charge carriers are transported along the percolation paths of pure material.

Bulk heterojunction (BHJ) solar cells are based on a blend of donor and acceptor molecules in one active layer. Such a device is depicted in Fig. 2.7 (a). Charge carriers are transported between adjacent molecules of the same semiconductor type, thus electrons on acceptor and holes on donor molecules. Due to the random arrangement of these molecules, an interpenetrating network of donor and acceptor molecules is created. Charge carriers are transported on this network on percolation paths which strongly depend on the microscopic morphology of the blended material. In addition to well blended phases, domains of pure material can also exist. The morphology can be influenced by the choice of the solvents, additives or thermal annealing during the device preparation [52–54]. The charge carrier mobility of semiconductor blends is lower compared to that of pure semiconductor layers [55].

The energetic structure of a BHJ solar cell is described according to the effective medium approach. This is shown in Fig. 2.7 (b). The semiconductor blend is interpreted as one single effective material. Photons are absorbed over the (optical) band gaps of donor and acceptor molecules. The generated excitons are separated very effectively due to the free availability of donor–acceptor heterojunctions. All electrons are consequently transported on the LUMO of the acceptor, holes on the HOMO of the donor. The energy difference between these two energies is denoted as the effective band gap E_g.

A BHJ solar cell offers a more efficient charge carrier generation in comparison with PHJ devices. However, also the recombination probability of charge carriers is higher in a BHJ device due to a lower effective mobility and the proximity of electrons and holes. A comparison between both device types is given in Chapter 5.

2.4. Current–voltage characteristics

Solar cells produce a measurable current dependent on the applied voltage and illumination intensity. This is depicted in Fig. 2.8. Solar cells in the dark show a rectifying current–voltage characteristics expected for diodes. An additional photocurrent is generated under illumination.

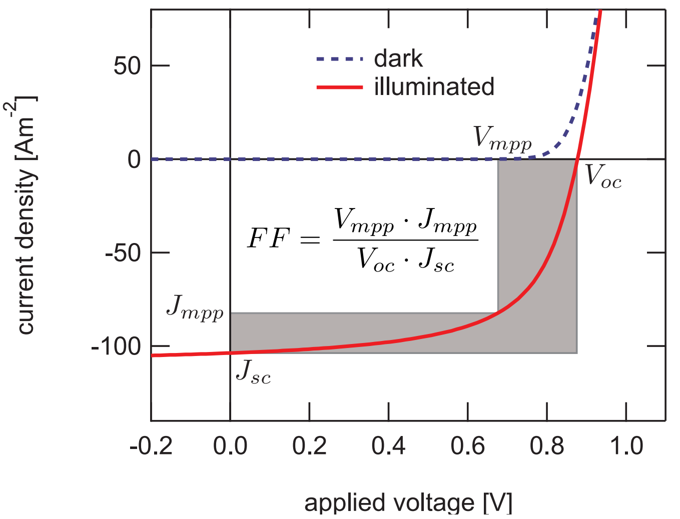

Figure 2.8.: Rectifying diode characteristics retrieved from organic solar cells. The open circuit voltage V_{oc}, the short circuit current J_{sc} and the fill factor FF are of special interest for characterization and comparison purposes. The fill factor defines the relation between V_{oc} and J_{sc} to the maximum extractable power. The maximum power point is defined by its components V_{mpp} and J_{mpp}.

The illuminated device generates the open circuit voltage V_{oc} if the electrodes are not connected to a load. The short circuit current J_{sc} is extracted if both electrodes are shorted. A point of maximum power $P_{mpp} = J_{mpp} \cdot V_{mpp}$ is found between an applied voltage of $V(J_{sc}) = 0$ V and V_{oc}. The fill factor FF correlates this maximum power point to V_{oc} and J_{sc},

$$FF = \frac{P_{mpp}}{V_{oc} \cdot J_{sc}}. \tag{2.10}$$

The electric power conversion efficiency η of the solar cell is determined by

$$\eta = \frac{P_{mpp}}{P_L} = \frac{V_{oc} \cdot J_{sc} \cdot FF}{P_L}. \tag{2.11}$$

The power of the incident light is given as P_L. For a level of illumination corresponding to one sun on earth (AM1.5g spectrum), P_L is approximately 1000 W/m^2.

The maximum photocurrent is extracted from a solar cell if all incident photons are converted into free charge carriers and extracted from the device. This current is extracted from organic solar cells at high reverse-biases where charge extraction is faster than charge carrier recombination processes. If at short circuit conditions only moderate recombination losses of charge carriers are assumed, J_{sc} can be approximated by the generation rate G and the active layer thickness L,

$$J_{sc} \approx qGL. \tag{2.12}$$

The equation is used to estimate the charge carrier generation rate for measured solar cells. The work function difference between the neat anode and cathode materials is denoted as the built-in potential V_{bi}.

3. Generation and recombination of charge carriers

The charge carrier densities are of crucial importance for the performance of organic solar cells. In organic semiconductors, charge carriers are generated steadily by thermal excitation and by injection by metal electrodes. Excess charge carriers are generated, for instance, by the absorption of light. From a perfect solar cell, all excess charge carriers would be extractable. Recombination however limits the amount of charge carriers in organic solar cells. A mathematical description of the charge carrier densities is therefore required. This allows the definition of generation and recombination models that can be used to simulate organic solar cells.

3.1. Thermal activation of charge carriers

In an organic solar cell, a small amount of thermally activated charge carriers is consistently present at temperatures above $T = 0$ K. These charge carriers are thermally excited over the energetic band gap E_g. Their amount is obtained by multiplying the density of state distributions $D_{LUMO}(E)$ and $D_{HOMO}(E)$ with the Fermi–Dirac statistic $f_{ED}(T, E_F, E)$ and integrating over all relevant energies E,

$$\begin{aligned} n &= \int_{-\infty}^{\infty} D_{LUMO}(E) \cdot f_{FD}(T, E_F, E) \mathrm{d}E & (3.1) \\ p &= \int_{-\infty}^{\infty} D_{HOMO}(E) \cdot [1 - f_{FD}(T, E_F, E)] \,\mathrm{d}E. & (3.2) \end{aligned}$$

The Fermi energy E_F is identical for electrons and holes in this case. According to the Schrödinger equation when applied for a 3-dimensional electron gas contained in an infinite potential well, square root dependent density of state distributions $D(E) \propto \sqrt{E}$ are expected [13]. Even though this approximation is deduced from inorganic semiconductors, it has been shown that it can also be used to simulate organic semiconductors. The systematical error introduced here is known to be small from experience [56]. This approximation allows the application of very efficient numerical calculation methods. As a consequence, the integrals in Eqns. (3.1) and (3.2) can be simplified to [13]

$$n = N_c \cdot \exp\left(\frac{E_F - E_{LUMO}}{k_B T}\right), \tag{3.3}$$

$$p = N_v \cdot \exp\left(\frac{E_{HOMO} - E_F}{k_B T}\right). \tag{3.4}$$

This simplification is valid for temperatures lower than $k_BT \ll E_F - E_{LUMO}$ and $k_BT \ll E_{HOMO} - E_F$, which usually includes room temperature. N_c and N_v denote the effective density of states of LUMO and HOMO. The product of electron and hole charge carrier density is equal to the square of the intrinsic charge carrier density n_i as no excess charge carriers are generated,

$$n_i^2 = n \cdot p. \tag{3.5}$$

The intrinsic charge carrier density is consequently defined as

$$n_i = \sqrt{N_c \cdot N_v} \exp\left(-\frac{E_g}{2 \cdot k_BT}\right). \tag{3.6}$$

Additional charge carriers ($np \gg n_i^2$) are generated in organic semiconductors, for example by illumination. These excess charge carriers can be incorporated in Eqns. (3.3) and (3.4), by allowing the Fermi energy to split up. Thus, two independent quasi-Fermi energies for electrons E_{Fn} and holes E_{Fp} are defined,

$$n = N_c \cdot \exp\left(\frac{E_{Fn} - E_{LUMO}}{k_BT}\right), \tag{3.7}$$

$$p = N_v \cdot \exp\left(\frac{E_{HOMO} - E_{Fp}}{k_BT}\right). \tag{3.8}$$

According to the latter definition, all charge carriers present are assigned to a thermal activation without considering their actual origin.

An important simplification of the drift–diffusion equations (Eqns. (2.7), (2.8)) is found by inserting the charge carrier density definitions. The electron and hole currents consequently read

$$J_n = q\mu_n n \frac{\partial E_{Fn}}{\partial x}, \tag{3.9}$$

$$J_p = -q\mu_p p \frac{\partial E_{Fp}}{\partial x}. \tag{3.10}$$

This result is important in terms of band diagrams. An example is given in Fig. 3.1. A band diagram shows the spatially resolved energy distributions of the LUMO and HOMO as well as the quasi-Fermi energies and the work functions of the metal electrodes. From these diagrams, the spatially resolved charge carrier densities as well as the current densities can be estimated according to Eqns. (3.7) to (3.10). The local electric field F corresponds to the spatial derivative of the HOMO or LUMO energy distribution,

$$F = -\frac{\partial E_{LUMO}}{\partial x} = -\frac{\partial E_{HOMO}}{\partial x}. \tag{3.11}$$

The difference between the metal Fermi energies on the left and right end of the solar cell indicates the applied voltage. The spatial dependence (x) of charge carrier densities, energies and electric field was not explicitly stated for a clearer notation.

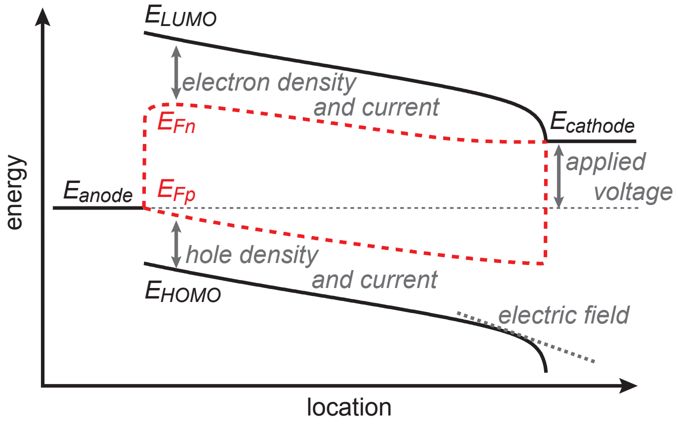

Figure 3.1.: Band diagram of an organic BHJ solar cell showing the HOMO and LUMO energies (E_{LUMO}, E_{HOMO}), the quasi-Fermi energies (E_{Fn}, E_{Fp}) as well as the Fermi energies of the electrodes (left and right). It can be used to estimate the local electric field F, the charge carrier densities n, p as well as the current densities J_n, J_p. The electric field is given by the slope of the LUMO and HOMO bands according to Eqn. (3.11). The electron n and hole p densities are defined by the energy difference between the semiconductor bands and their corresponding quasi-Fermi energies (Eqns. (3.7) and (3.8)). The current densities are proportional to the product of charge carrier densities and the slope of the quasi-Fermi energies (Eqns. (3.9) and (3.10)). The applied voltage is the energy difference between both electrode Fermi energies.

3.2. Charge carrier injection

Charge carriers are injected into the semiconductor by metal electrodes. The contact properties are defined by the energy offset between the Fermi energy of the metal and the HOMO and LUMO energies of the semiconductor. Such offsets are denoted as injection barriers. According to the thermionic emission theory, charge carriers are injected from the free electron gas of the metal into the bands of the semiconductor by thermal activation.

Only one injection barrier is usually defined for each contact denoting the smaller of both possible offsets. For a cathode with injection barrier Φ_n, this is depicted in Fig. 3.2 (b). The injected charge carrier densities are given by

$$n_{th} = N_c \cdot \exp\left(-\frac{q\,\Phi_n}{k_B T}\right) \tag{3.12}$$

$$p_{th} = N_v \cdot \exp\left(-\frac{q\,(E_g - \Phi_n)}{k_B T}\right). \tag{3.13}$$

Significantly more electrons than holes are injected at the cathode. The product of electron and hole density is still in agreement with the intrinsic charge carrier density, $n \cdot p = n_i^2$. Thus, no excess charge carriers are injected into the semiconductor, but the electron–hole ratio has been changed. The term selective contact was therefore established. An anode is described accordingly,

$$n_{th} = N_c \cdot \exp\left(-\frac{q\,(E_g - \Phi_p)}{k_B T}\right) \tag{3.14}$$

$$p_{th} = N_v \cdot \exp\left(-\frac{q\,\Phi_p}{k_B T}\right). \tag{3.15}$$

Regions containing mainly electrons or holes are created since injected charge carriers diffuse into the semiconductor. The charge carrier type that exceeds the other is denoted as the majority, the other as the minority charge carrier density. Eqns. (3.12) - (3.15) represent Schottky contacts, whereas an Ohmic contact denotes the special case of a vanishing injection barrier [13].

The impact of a metal electrode attached to an undoped semiconductor is depicted in Fig. 3.2. In a neat semiconductor (a), charge carriers are thermally activated into the HOMO and LUMO. The electron–hole ratio is changed by injected charge carriers (b) at an electrode. Injected charge carriers diffuse into the semiconductor and generate a repulsive electric field $F(x)$ according to the Poisson equation [57],

$$\frac{\partial}{\partial x}\left[\varepsilon_r(x)F(x)\right] = \frac{q}{\varepsilon_0}\left[n(x) - p(x) + C(x)\right]. \tag{3.16}$$

This electric field is indicated by band bending (BB) in band diagrams. The relative permittivity is given by ε_r. An optional doping of the semiconductor is considered by $C(x)$. Excess charge carriers introduced by illumination or an applied voltage result in a split-up of the quasi-Fermi levels (Fig. 3.2 (c)).

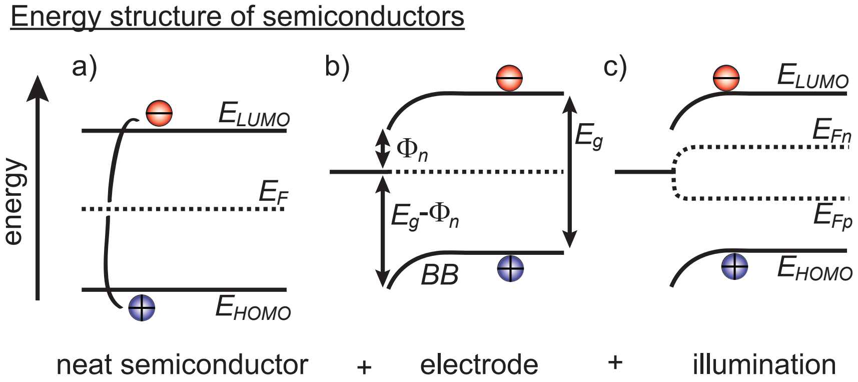

Figure 3.2.: Energetic structure of (a) an undoped semiconductor with thermally activated charge carriers. From (b) a metal electrode (cathode) with an injection barrier Φ_n, electrons are injected and diffuse into the semiconductor. The generated charge carrier gradients create a repulsive electric field indicated by band bending (BB). Illumination (c) generates excess charge carriers in the device and splits-up the quasi-Fermi levels E_{Fn} and E_{Fp}.

3.3. Generation and geminate recombination

Photogenerated charge carriers in organic solar cells are created by a multi-level process starting with the absorption of light. Absorbed photons generate excitons on organic molecules. If these excitons reach a semiconductor heterojunction, one charge is transferred to the other organic semiconductor and a weaker bound polaron pair is created. Subsequently the polaron pair is separated into free charge carriers. Several processes limiting the efficiency of the generation process are imaginable. Excitons that do not reach a heterointerface within their statistical lifetime will recombine. The same applies to polaron pairs whose separation process fails. Since electron and hole of these quasi-particles were generated by the same absorbed photon, such recombination processes are denoted as geminate recombination.

Exciton decay

Excitons are generated by the absorption of light with the generation rate G. This rate defines the amount of generation events per volume and second. An exciton decays to the ground state after a statistical lifetime τ_x if it is not separated. The recombination rate R of an exciton density X to the ground state is defined by

$$R = \frac{X}{\tau_x} = k_x X. \tag{3.17}$$

The lifetime τ_x can be transformed into a rate k_x by inversion of the lifetime in the case of quasi-particles.

The Onsager–Braun theory

The separation of polaron pairs in BHJ solar cells requires a more detailed formalism. In 1938, Onsager investigated the recombination of Coulombic bound ion pairs of weak electrolytes in aqueous solution under the influence of an applied electric field [58]. The ion pairs observed either mutually recombined or were separated. In 1983, Braun extended this model and applied it to charge carrier generation in electrical conductive polymers [59]. He defined a precursor state to free charge carriers, the charge transfer complex in its lowest excited state CT_1. Today, this state is often called a polaron pair. The Onsager–Braun theory has been successfully used to describe the photocurrent in organic solar cells [60]. Small divergences to experimental findings have however been documented [61].

According to the theory, polaron pairs with binding distance r under an applied electric field F are separated with the rate k_D,

$$k_D(r,T,F) = \frac{3\gamma}{4\pi a^3} \exp\left(-\frac{E_B(r)}{k_B T}\right) \frac{J_1(2-\sqrt{-2b})}{\sqrt{-2b}}. \tag{3.18}$$

The latter equation introduces the first order Bessel function J_1 with its argument b as well as the Coulomb binding energy E_B between the two charged partners,

$$b = \frac{q^3 F}{8\pi\varepsilon_0\varepsilon_r k_B^2 T} \quad \text{and} \quad E_B(r) = \frac{q^2}{4\pi\varepsilon_0\varepsilon_r r}. \tag{3.19}$$

Thus, the Onsager–Braun model considers Coulomb attraction between both polaron pair partners as well as the separating effect of an applied electric field. The Langevin capture rate γ is required in case the separation process fails. The Langevin capture rate is derived in the next Section. For numerical calculations, J_1 is replaced by its Taylor series. The states and rates considered by the Onsager–Braun theory are summarized in Fig. 3.3.

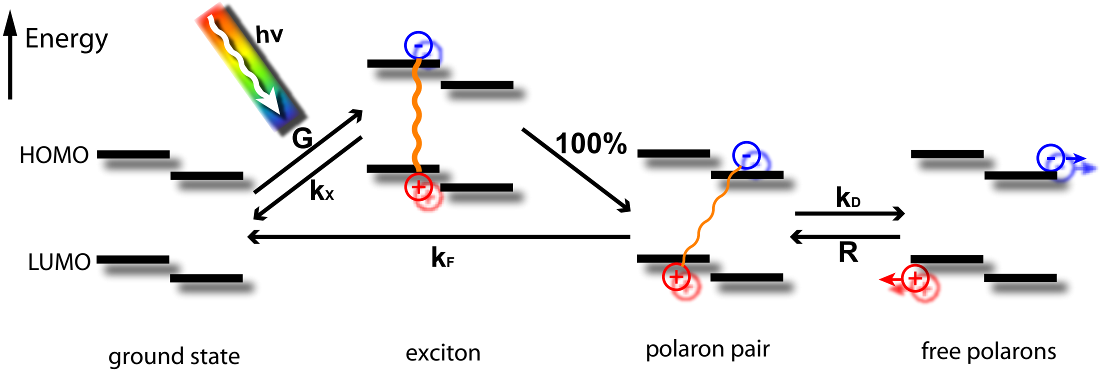

Figure 3.3.: Charge carrier generation according to the Onsager–Braun model. Excitons are generated by light with the generation rate G. The separation process of polaron pairs in BHJ solar cells is assumed to be very (100%) effective since semiconductor heterojunctions are available throughout the entire active layer. Exciton decay (k_x) is therefore negligible. The polaron pairs are subsequently separated into free polarons (k_D). Charge carriers are lost due to mutual recombination to a precursor state (R, k_F).

The polaron pair separation $k_D(r,T,F)$ competes a temperature dependent polaron pair decay to the ground state $k_F(T)$. The separation probability of a polaron pair with a binding distance r under an external electric field F is defined by

$$p(r,T,F) = \frac{k_D(r,T,F)}{k_D(r,T,F) + k_F(T)}. \tag{3.20}$$

If the HOMO and LUMO levels of organic semiconductors are of Gaussian shape, a similar distribution of the polaron pair binding distance is also expected. The Onsager–Braun model was therefore extended by a Gaussian distribution of the polaron pair binding distances [60]. Considering the most probable binding distance a, the integral over all binding distances r results in an average polaron pair separation probability P,

$$P(a,T,E) = \int_0^\infty p(r,T,E) \cdot \frac{4}{\sqrt{\pi} a^3} r^2 \exp\left(-\frac{r^2}{a^2}\right) \mathrm{d}r. \tag{3.21}$$

In a BHJ solar cell, the generation of free polarons is described by the (exciton) generation rate G multiplied by the probability of free charge carrier generation P. For a PHJ device, the rate of separated excitons at the heterointerface has to be used instead of G.

3.4. Nongeminate recombination

Free charge carriers usually originate from different generation events. The recombination of such independent charge carriers is denoted as nongeminate. Several such processes are known from literature. Especially Langevin, Shockley-Read-Hall (SRH) and tail state recombination have been shown to be important for organic solar cells. Whereas the Langevin theory describes recombination between free charge carriers, trap states mediate the SRH recombination. The recombination of charge carriers trapped in tail states according to the MTR model is usually treated separately. Auger recombination is not expected to play a major role in organic electronics [9, 62, 63]. The differences between the recombination mechanisms are summarized in Fig. 3.4.

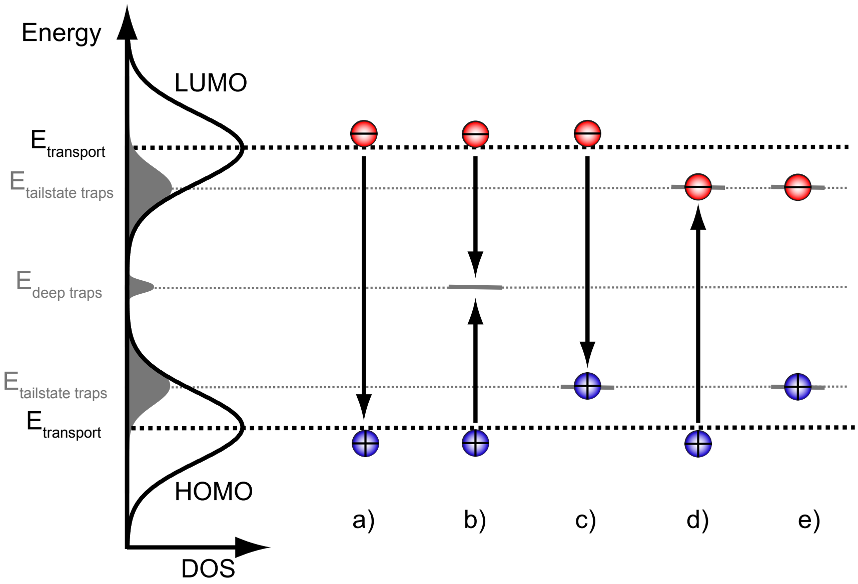

Figure 3.4.: Possible recombination paths in organic semiconductors. A direct recombination of free charge carriers (a) is described by the Langevin theory. The SRH recombination (b) defines a recombination mediated by mid-gap traps. In terms of the MTR model, charge carriers trapped in tail states (shallow traps) and mid-gap traps (deep traps) can be distinguished. The recombination paths including tail state traps, (c) and (d), are usually treated separately. Two trapped charges (e) are assumed not to recombine due to their immobility [38].

Langevin recombination

The most basic model for charge carrier recombination in organic semiconductors is the Langevin recombination [64]. Proposed in 1903, it defines the direct recombination of free charges with a mean free path smaller than their capture radius. This condition is fulfilled in narrow band semiconductors with mobilities of less than 1 cm^2/Vs, leading to scattering lengths on the order of the lattice constant [9].

According to Langevin's assumptions, two mutually attracted charge carriers inevitably recombine if the energy of their Coulomb attraction E_{cb} exceeds the thermal energy E_{th}

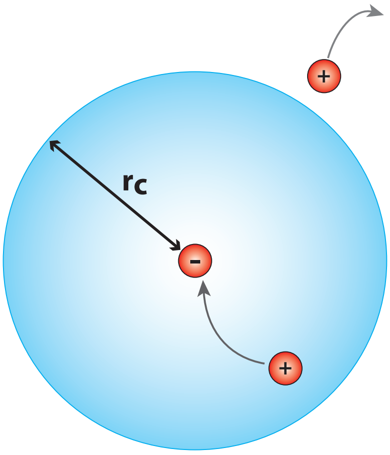

Figure 3.5.: According to the Langevin theory, two oppositely charged charge carriers will inevitably recombine if the distance between both charges is smaller than the Coulomb radius r_c. This radius describes the equilibrium between Coulomb attraction and the thermal energy of both charge carriers.

which is responsible for the Brownian motion of charge carriers. The Coulomb radius r_c is defined as the distance at which both energies are identical,

$$E_{cb} = E_{th}, \tag{3.22}$$

consequently,

$$\frac{q^2}{4\pi\varepsilon_0\varepsilon_r r_c} = k_B T. \tag{3.23}$$

Written in terms of r_c, this yields the minimal distance between two charges at which they will not inevitably recombine with each other,

$$r_c = \frac{q^2}{4\pi\varepsilon_0\varepsilon_r k_B T}. \tag{3.24}$$

The Coulomb radius is illustrated in Fig. 3.5. A Coulomb radius of 14 to 17 nm is obtained in organic semiconductors at room temperature with relative dielectric permittivities of around 3.4 to 4.0. Assuming a virtually stationary hole, an attracted electron moves with the effective mobility of both charge carriers, $\mu_n + \mu_p$. The drift current density j towards the hole caused by the electric Coulomb-field F_{cb} reads

$$j = qp(\mu_n + \mu_p)F_{cb} = qp\,(\mu_n + \mu_p)\,\frac{q}{4\pi\varepsilon_0\varepsilon_r r_c^2}. \tag{3.25}$$

In a 3-dimensional space, the critical binding distance corresponds to a surface of a sphere with radius r_c. The recombination current J is therefore given by

$$J = qp\frac{q(\mu_n + \mu_p)}{\varepsilon_0\varepsilon_r} = qp\,\gamma. \tag{3.26}$$

This defines the Langevin recombination factor γ as

$$\gamma = \frac{q}{\varepsilon_0 \varepsilon_r} (\mu_n + \mu_p) . \tag{3.27}$$

The Langevin recombination rate R_L reads

$$R_L = \gamma \left(np - n_i^2 \right) . \tag{3.28}$$

Thus, R_L is proportional to the sum of electron and hole mobilities as well as to the electron and hole densities. The steadily generated intrinsic charge carrier density n_i^2 is excluded from recombination.

In recent years, experiments have shown recombination rates lower than predicted by the Langevin theory [51, 65]. Attempts to modify the Langevin theory have consequently been made. A first approach was to limit the recombination to the lower of both mobilities [66]. In terms of a more general attempt, a Langevin reduction factor ζ has been introduced later [67, 68],

$$R_L = \gamma \, \zeta \left(np - n_i^2 \right) . \tag{3.29}$$

If electron and hole densities are assumed to be equal, there is an expected recombination rate quadratically dependent on the charge carrier density. This theoretical recombination order of 2 usually differs in experiments [69]. The origin of this effect is discussed in Chapter 8.

Shockley–Read–Hall recombination

In inorganic and especially indirect semiconductors, trap assisted recombination is assigned to be the main recombination mechanism. Assuming recombination centers approximately in the middle of the effective band gap, Shockley, Read and Hall (SRH) derived a detailed balance rate equation considering the capture and thermal release of electrons and holes into these mid-gap traps [70, 71].

According to the SRH theory, free charge carriers are captured and released by trap states of density N_t and energy E_t. The probability of charge carriers moving with a thermal velocity of v_{th} to be captured is described by the capture cross sections for electrons σ_n and holes σ_p. The SRH recombination rate is defined by [13],

$$R_{SRH} = \frac{\sigma_n \sigma_p v_{th} N_t \left(np - n_i^2 \right)}{\sigma_n \left[n + n_i \exp\left(\frac{E_t - E_i}{k_B T} \right) \right] + \sigma_p \left[p + n_i \exp\left(\frac{E_i - E_t}{k_B T} \right) \right]} \tag{3.30}$$

The intrinsic Fermi energy of the semiconductor is given by E_i. Trap energies identical to this Fermi energy (approximately in the middle of the band gap) result in maximum recombination probability [13].

For numerical simulations, the SRH recombination is often simplified. If the semiconductor layer is doped, the capture cross sections and the thermal velocity can be transformed into effective charge carrier lifetimes $\tau_n = 1/(\sigma_n v_{th} N_t)$ and $\tau_p = 1/(\sigma_p v_{th} N_t)$ [33, 72]. This simplifies Eqn. (3.30) to

$$R_{SRH} = \frac{np - n_i^2}{\tau_p \left[n + n_i \exp\left(\frac{E_t - E_i}{k_B T} \right) \right] + \tau_n \left[p + n_i \exp\left(\frac{E_i - E_t}{k_B T} \right) \right]}. \tag{3.31}$$

Recently, the SRH recombination was applied to explain the influence of tail state traps in organic solar cells [73]. SRH recombination was also observed in organic semiconductors at very low light intensities. [37, 63]. The results were however revoked later due to errors in the experimental setup [74]. In amorphous silicon (a-Si), similar to organic semiconductors due to its disorder, SRH is widely used to describe recombination caused by impurities in the crystal structure [75, 76]. Whether or not deep trap recombination is a relevant contribution to recombination in organic semiconductors is still a matter of controversial discussion.

Tail state recombination

According to the MTR model, charge carriers are trapped in tail states of the HOMO and LUMO bands. The charge carriers are located energetically closer to the transport energies than the deep traps mentioned in the derivation of the SRH model [77]. The difference is illustrated in Fig. 3.4. Recombination mediated by these shallow traps is either described according to the SRH formalism [73] or by a Langevin like process. In the latter case, the zero mobility of the trapped charge carriers inhibiting trap–trap recombination must be taken into account [38]. Tail state recombination could explain reduced recombination rates found in experiments, as well as recombination orders ($\lambda + 1$) higher than two [38, 69, 78–80],

$$R_{exp} = k_{\lambda+1} n^{\lambda+1}. \tag{3.32}$$

All recombination processes presented will occur simultaneously in an organic solar cell, albeit in different orders of magnitude. For most numeric simulations it is sufficient to determine the main recombination paths. At illumination intensities from the sun, we assume that Langevin recombination as well as the Onsager–Braun theory are the dominant recombination processes [9, 62, 63].

3.5. Surface recombination

In addition to recombination processes in semiconductors, losses of charge carriers also occur at surfaces and electrodes [81]. Two charge carriers with opposite signs will inevitably recombine if both simultaneously enter a metal electrode or a surface trap state. The surface recombination currents of excess electrons $J_{surf,\,n}$ and holes $J_{surf,\,p}$ are given by

$$J_{surf,\,n} = qS_n(n - n_{th}), \tag{3.33}$$

$$J_{surf,\,p} = qS_p(p - p_{th}). \tag{3.34}$$

A recombination process is defined if the electron and hole surface recombination currents at a surface or an electrode are equal and non-zero. The surface recombination velocities S_n, S_p denote the speed and thusly the efficiency of the recombination process.

At metal electrodes, both surface recombination velocities can differ from one another. The difference between both surface recombination currents is identical to the measurable current that is extracted from or injected into the solar cell. Since these currents have to also overcome the metal–organic interface, they are limited by the surface recombination velocities as well. The surface recombination velocities therefore represent generally slowed-down current transport across the metal–organic interfaces. Most models that do not explicitly mention surface recombination implicitly assume infinitely fast surface recombination velocities.

Mirror charge effects at metal–organic interfaces were successfully described by finite surface recombination velocities [82]. Finite surface recombination velocities were also found to limit the power conversion efficiencies of organic solar cells. This is discussed in Chapters 5 and 7.

3.6. The continuity equations

For device simulations, the amount of electrons, holes, excitons and polaron pairs has to be determined. All generation and recombination processes populating and depopulating a specific state are added in terms of the net recombination rate U,

$$U = \sum_i R_i - \sum_i G_i. \tag{3.35}$$

The continuity equations describe the resulting charge carrier densities taking additional currents into account. For electrons and holes the continuity equations read

$$\frac{\partial n}{\partial t} - \frac{1}{q}\frac{\partial J_n}{\partial x} = -U, \tag{3.36}$$

$$\frac{\partial p}{\partial t} + \frac{1}{q}\frac{\partial J_p}{\partial x} = -U. \tag{3.37}$$

The derivative with respect to time t is set to zero in order to obtain the steady state solution.

4. Numerical approaches

Current–voltage characteristics of organic solar cells can be calculated by combining models for charge carrier transport with models for generation and recombination of charge carriers. Such models were introduced in the previous chapters. A coupled differential equation system of second order is yielded if all required equations are summarized. Since the equation system is not analytically solvable, a numerical approach needs to be developed.

4.1. Definition of the numerical problem

An organic solar cell is mathematically described by the differential equation system of drift–diffusion equations (Eqns. (2.7), (2.8)), continuity equations (Eqns. (3.36), (3.37)), as well as the Poisson equation (Eqn. (3.16)). These equations connect the local electric field with the flux of charge carriers. Furthermore, correlations between the quasi-Fermi energies and the charge carrier densities (Eqns. (3.7), (3.8)) are required. In order to reliably find a numerical solution, this differential equation system must first be transformed into a more convenient form. This is achieved by transforming all energies to corresponding electric potentials. The electric field as well as the LUMO and HOMO energies are replaced by the electric potential $F = -\partial\Psi/\partial x$. The quasi-Fermi energies are exchanged for the quasi-Fermi potentials φ_n and φ_p [13, 33]. The resulting equation system reads

$$\frac{\partial}{\partial x}\left(\varepsilon_r \frac{\partial}{\partial x}\Psi\right) = \frac{q}{\varepsilon_0}\left[n - p + C\right], \tag{4.1}$$

$$J_n = -qn\mu_n\frac{\partial\Psi}{\partial x} + qD_n\frac{\partial n}{\partial x}, \qquad J_p = qp\mu_p\frac{\partial\Psi}{\partial x} + qD_p\frac{\partial p}{\partial x}, \tag{4.2}$$

$$n = n_i \cdot \exp\left(\frac{q\left[\Psi - \varphi_n\right]}{k_BT}\right), \qquad p = n_i \cdot \exp\left(\frac{q\left[\varphi_p - \Psi\right]}{k_BT}\right), \tag{4.3}$$

$$\frac{1}{q}\frac{\partial J_n}{\partial x} = \frac{\partial n}{\partial t} + U, \qquad -\frac{1}{q}\frac{\partial J_p}{\partial x} = \frac{\partial p}{\partial t} + U. \tag{4.4}$$

All information on the absolute energies is lost due to this transformation. However, it enables a numerically favorable symmetric definition of the mathematical problem in space by defining reasonable Dirichlet boundary conditions.

For an active layer with a thickness of L, an applied voltage V is equally distributed between both boundaries, $\Psi(0) = -V/2$ and $\Psi(L) = V/2$. Injection barriers are subtracted separately for each contact. The surface recombination currents (Eqns. (3.33) and (3.34)), written in terms of the charge carrier densities are used as boundary conditions for the charge carrier density distributions. For the diffusion of excitons and polaron pairs, an equivalent equation system can be set up if required.

4.2. Discretizing and scaling of variables

Two further adjustments must be made in order to implement the given equation system in a simulation program. First, all equations have to be discretized from their analytical form to a discrete grid. Second, all variables have to be scaled.

The active layer of the solar cell is discretized by equidistant grid points in one dimension perpendicular to the layer structure. The equation system is solved at each point. The distance h between two grid adjacent points must not exceed the Debye length $\lambda_D = \sqrt{\varepsilon_0 \varepsilon_r k_B T / q^2 n_i}$ [33]. For organic semiconductors at room temperature, the Debye length is commonly in the order of several nanometers. The discretization of the equation system was implemented according to the finite difference method [83]. Derivatives are defined by the linear centered approximation approach. Thus, the first derivative of an arbitrary function $f(x)$ on the i-th grid point can be written as

$$\left.\frac{\partial f(x)}{\partial x}\right|_i = \frac{1}{h}\left[f(x)|_{i-1/2} - f(x)|_{i+1/2} \right]. \tag{4.5}$$

The error generated here is proportional to h^2 which represents an accuracy of second order [83]. Derivatives of second order are obtained by the iterative use of Eqn. (4.5). Function values of $f(x)$ at fractional grid distances are approximated by linear interpolation. Integrals are solved using a self-converging trapezoidal method [84].

Furthermore, numerical errors must be avoided. An example of such an error is the addition of two numbers of different orders of magnitude. If the smaller value stored in a variable is not representable within the discrete range of the larger value, the higher number is returned without performing any mathematical operation. Consequently, all variables have to be scaled.

Several possible approaches to this scaling can be found in literature [33, 85–87]. A combination of the scaling by DeMari and Selberherr was empirically found to be the most suitable for the purposes of simulating organic solar cells [33, 86]. The scaling parameters are listed in Table 4.1. Scaled variables are without dimension. The scaling in combination with the representation of charge carrier densities by quasi-Fermi potentials enables numerically stable solutions within an applied voltage range of $|V| \lesssim 37\ V$. The Slotboom representation for charge carrier densities must be selected for calculations at higher voltages, although this results in an reduced simulation accuracy [85]. Any approach to solving the equation system (4.1) - (4.4) without scaling will either fail or require extensive calculation times.

4.3. The Gummel method

The Gummel method is widely used in computational science to solve the Poisson equation [88]. It obtains the electric potential distribution according to the Poisson equation for arbitrarily given charge carrier densities.

A given and error-prone electric potential distribution Ψ differs by an error of $\delta\Psi$ from the

parameter	scaling factor	value	description
x	x_0	1 nm	space
Ψ	Ψ_0	$k_B \cdot T/q$	potential
n, p	n_0	$\varepsilon_0 \cdot \varepsilon_r \cdot k_B \cdot T/(q^2 \cdot x_0^2)$	charge carrier densities
μ_n, μ_p	μ_0	$\max(\mu_n, \mu_p)$	mobilities
D_n, D_p	D_0	$\mu_0 \cdot \Psi_0$	diffusion constants
U, G, R	G_0	$D_0 \cdot n_0/x_0^2$	rates per volume
t	t_0	x_0^2/D_0	time

Table 4.1.: Scaling parameters for efficient numerical calculations. All parameters not mentioned here can be scaled by appropriate combinations of the given scaling parameters.

exact solution of the Poisson equation,

$$\Psi_{exact} = \Psi + \delta\Psi. \tag{4.6}$$

In order to determine the deviation from the exact result $\delta\Psi$, the latter equation is inserted in the Poisson equation,

$$\frac{\partial^2}{\partial x^2}\Psi_{exact}(x) = \frac{q}{\varepsilon_0\varepsilon_r}\Big[n(x) - p(x)\Big]. \tag{4.7}$$

Doping and spatial variations in the relative permittivity are neglected for demonstration purposes. The charge carrier densities are also a function of the error-prone electrical potential distribution according to Eqns. (4.3). The Poisson equation consequently reads

$$\frac{\partial^2}{\partial x^2}[\Psi(x) + \delta\Psi(x)] = \frac{q}{\varepsilon_0\varepsilon_r} n_i \left\{\exp\left(\frac{\Psi + \delta\Psi - \varphi_n}{V_t}\right) - \exp\left(\frac{\varphi_p - (\Psi + \delta\Psi)}{V_t}\right)\right\}. \tag{4.8}$$

The thermal potential is denoted by $V_t = k_B T/q$. The charge carrier densities can be transformed back into their original form, excluding the previously included error $\delta\Psi$,

$$\frac{\partial^2}{\partial x^2}[\Psi(x) + \delta\Psi(x)] = \frac{q}{\varepsilon_0\varepsilon_r}\left\{n \cdot \exp\left(\frac{\delta\Psi}{V_t}\right) - p \cdot \exp\left(-\frac{\delta\Psi}{V_t}\right)\right\}. \tag{4.9}$$

A numerically useful result is found by replacing the exponential functions by Taylor series, truncated after the second member,

$$\frac{\partial^2}{\partial x^2}[\Psi(x) + \delta\Psi(x)] = \frac{q}{\varepsilon_0\varepsilon_r}\left\{n \cdot \left(1 + \frac{\delta\Psi}{V_t}\right) - p \cdot \left(1 - \frac{\delta\Psi}{V_t}\right)\right\}. \tag{4.10}$$

Written in terms of the error included $\delta\Psi$, the error can be determined. Discretized, this equation reads

$$\underbrace{\frac{1}{h^2}\left(\delta\Psi_{i-1}-2\delta\Psi_i+\delta\Psi_{i+1}\right)-\frac{q}{\varepsilon_0\varepsilon_r}\left(\frac{n_i+p_i}{V_t}\right)\delta\Psi_i}_{\boldsymbol{A}\cdot\overrightarrow{\delta\Psi}}=\underbrace{\frac{q}{\varepsilon_0\varepsilon_r}\left(n_i-p_i\right)-\frac{1}{h^2}\left(\Psi_{i-1}-2\Psi_i+\Psi_{i+1}\right)}_{\frac{q}{\varepsilon_0\varepsilon_r}\left(\vec{n}-\vec{p}\right)-\frac{1}{h^2}\left(\overrightarrow{\Psi''}\right)}. \tag{4.11}$$

The spatially resolved error $\overrightarrow{\delta\Psi}$ is calculated by multiplying the right part of Eqn. (4.11) with the inverted tridiagonal matrix $\boldsymbol{A}$. A large number of effective solving algorithms can be found in literature regarding this particular issue [33, 83–85, 89].

The Gummel method is based on the assumption that the electric potential changes solely linearly between two grid points. Due to the Taylor series included, the Gummel method has to be iteratively repeated until the remaining error vanishes. The overall truncation error of this method is of the order of one to the grid distance h. Experience however, has shown significantly smaller errors [33].

4.4. The Scharfetter–Gummel approximation

Instead of a linear dependence of the electric potential on the spatial position, the charge carrier densities generally show an exponential behavior. Linear solution approaches are consequently prone to errors. In 1969, Scharfetter and Gummel presented a non-trivial method to solve the drift–diffusion and continuity equation based on heuristically observations [90]. Proof of the uniqueness of the retrieved solutions was found years later [33].

In contrast to the charge carrier densities, the related current densities show a relatively linear dependence on spatial variations. The current density (shown here for electrons) between two grid points $x \in [x_i, x_{i+1}]$ can consequently be linearly interpolated,

$$J_n(x) = J_n\big|_{i+1/2} + \left(x - x_i - \frac{h}{2}\right)\cdot\frac{\partial}{\partial x}J_n\bigg|_{i+1/2}. \tag{4.12}$$

Assuming that the Einstein relations and charge carrier mobilities are spatially invariant, Eqn. (4.12) is inserted into the drift–diffusion equation (Eqn. (4.2)). Written in terms of the charge carrier density $n(x)$, the spatially resolved charge carrier distribution is given by

$$n(x) = (1 - g_i(x,\Psi))n_i + g_i(x,\Psi)n_{i+1}. \tag{4.13}$$

The charge carrier densities are only known at the grid points, n_i and n_{i+1}. The growth function $g_i(x,\Psi)$ is used for interpolations between two adjacent grid points,

$$g_i(x,\Psi) = \frac{1-\exp\left(\frac{\Psi_{i+1}-\Psi_i}{V_t}\cdot\frac{x-x_i}{h}\right)}{1-\exp\left(\frac{\Psi_{i+1}-\Psi_i}{V_t}\right)}. \tag{4.14}$$

The (scaled) current density between two grid points is consequently defined as

$$J_n|_{i+1/2} = D_n|_{i+1/2} \cdot \frac{B\left(\frac{\Psi_i - \Psi_i + 1}{V_t}\right) \cdot n_i - B\left(\frac{\Psi_{i+1} - \Psi_i}{V_t}\right) n_{i+1}}{h} + \\ + h\left(\frac{1}{2} \cdot \coth\left(\frac{\Psi_{i+1} - \Psi_i}{2 \cdot V_t}\right) - \frac{V_t}{\Psi_{i+1} - \Psi_i}\right) \cdot \frac{\partial}{\partial x} J_n|_{i+1/2} \cdot \tag{4.15}$$

The Bernoulli function $B(x)$ is introduced for a more efficient notation,

$$B(x) = \frac{x}{e^x - 1}. \tag{4.16}$$

The derivative of the electric current required in the continuity equation can be described according to Eqn. (4.15). If the higher-order terms are neglected, the steady state continuity equation for electrons reads

$$D_n|_{i+1/2} \cdot \frac{2 \cdot \left[B\left(\frac{\Psi_{i+1} - \Psi_i}{V_t}\right) \cdot n_{i+1} - B\left(\frac{\Psi_i - \Psi_{i+1}}{V_t}\right) \cdot n_i\right]}{h^2} - \\ - D_n|_{i-1/2} \cdot \frac{2 \cdot \left[B\left(\frac{\Psi_i - \Psi_{i-1}}{V_t}\right) \cdot n_i - B\left(\frac{\Psi_{i-1} - \Psi_i}{V_t}\right) \cdot n_{i-1}\right]}{h^2} + U(\Psi, n, p)|_i = 0. \tag{4.17}$$

The overall truncation error generated by this approach is linearly proportional to the grid spacing h [33].

In analogy to the Gummel method, Eqn. (4.17) defines a linear equation system with a tridiagonal matrix. This Scharfetter–Gummel approximation calculates the charge carrier density distribution according to a given electric potential and a net generation rate distribution. In contrast to literature, it was empirically found that calculating the equation system for electrons and holes sequentially is more advantageous than solving the system in parallel. This yields faster and more stable convergence behavior because the updated charge carrier densities can already be used to define the net generation rate U in the subsequent step. More detailed analyses of the equation system, truncation errors and numerical stability can be found in the books of Selberherr [33] and Mock [85], which both provide excellent overviews.

4.5. Multi-layer structures

Most semiconductor devices are constructed from multiple layers of different semiconductors. The band parameters for electrons Θ_n and holes Θ_p are defined to describe such heterojunctions [91]. They are applied to refer the charge carrier densities in each layer to one arbitrarily defined base layer with the intrinsic charge carrier density n_i^{base}. The definition of charge carrier densities is modified to

$$n = n_i^{base} \cdot \exp\left(\frac{q\left[\Psi - \varphi_n + \Theta_n\right]}{k_B T}\right) \quad \text{and} \quad p = n_i^{base} \cdot \exp\left(\frac{q\left[\varphi_p - \Psi + \Theta_p\right]}{k_B T}\right). \tag{4.18}$$

The band parameters are given by

$$\Theta_n = \Delta E_{LUMO} + \ln\left(\frac{N_c}{n_i^{base}}\right) \text{ and } \Theta_p = \Delta E_{HOMO} + \ln\left(\frac{N_v}{n_i^{base}}\right). \tag{4.19}$$

The band parameters have to be determined separately for each layer. Offsets between the energy levels ΔE_{HOMO} and ΔE_{LUMO} as well as differences between the effective density of states N_c and N_v are all taken into consideration due to this definition. The offsets ΔE_{HOMO} and ΔE_{LUMO} are defined by the HOMO and LUMO energies of the base layer minus the corresponding energy of the calculated semiconductor layer. The band parameters are zero for the selected base layer. A detailed description of the equations mentioned can be found in Ref. [72].

4.6. Optical interference

The thicknesses of the single material layers in organic solar cells commonly tend to be within the coherence length of light. Interference effects consequently result in spatially dependent profiles of the charge carrier generation rate $G(x)$. The standard approach to determine interference is the transfer matrix formalism [92–94]. It calculates the transmission, reflection and absorption of photons in the entire solar cell based on the complex refraction index of each material,

$$\tilde{n}(\lambda) = n'(\lambda) + i\kappa(\lambda). \tag{4.20}$$

The real part n' is a measure for the speed of light in a medium whereas the imaginary part defines the absorbance of light. Both are dependent on the wavelength λ.

An organic solar cell is generally described as a stack of plane-parallel layers with different optical properties. A photon is either transmitted or reflected at interfaces between two layers [92]. The sum of the probability of transmission T and reflection R at such an interface is one,

$$T + R = 1. \tag{4.21}$$

In a multilayer device, light is transmitted and reflected several times. A schematic example is depicted in Fig. 4.1. The transfer matrix method considers solely the electric field component of an electromagnetic wave since the magnetic component barely interacts.

In terms of the transfer matrix formalism, the device is separated into a sequence of alternating interface ($\boldsymbol{I}_{ij}$) and layer ($\boldsymbol{L}_i$) matrices. The indexes i and j refer to the layer number. The propagation of light is defined by a matrix equation,

$$\begin{bmatrix} E_0^+ \\ E_0^- \end{bmatrix} = \underbrace{\left(\prod_{i=0}^{m} \boldsymbol{I}_{(i-1)i} \cdot \boldsymbol{L}_i\right) \cdot \boldsymbol{I}_{m(m+1)} \cdot}_{\boldsymbol{S}} \begin{bmatrix} E_m^+ \\ E_m^- \end{bmatrix}. \tag{4.22}$$

A superscripted plus indicates a wave that propagates from the left to the right whereas a minus indicates the opposite. A surrounding atmosphere is expected on both sides (0 and m) of the solar cell. A light wave that incidents from the left E_0^+ (right E_m^-) finally leaves the device on both sides (E_0^-, E_m^+) after multiple reflection and transmission events. The

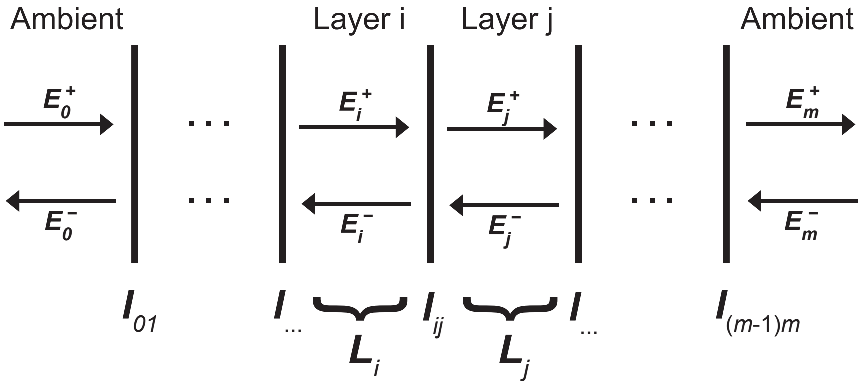

Figure 4.1.: Interference in a plane-parallel structure. An incident wave E_0^+ is either transmitted through, or reflected back from a material interface. The transfer matrix algorithm defines interface matrices $\boldsymbol{I}_{ij}$ and layer matrices $\boldsymbol{L}_i$ in order to describe the propagation of light.

product of all layer and interface matrices is denoted as scattering matrix $\boldsymbol{S}$. Light is either transmitted t_{ij} or reflected r_{ij} at a smooth interface $\boldsymbol{I}_{ij}$,

$$\boldsymbol{I}_{ij} = \frac{1}{t_{ij}} \begin{bmatrix} 1 & r_{ij} \\ r_{ij} & 1 \end{bmatrix}. \tag{4.23}$$

For an electromagnetic wave with an electric field component perpendicular to the interface normal, the Fresnel coefficients are defined by

$$r_{ij} = \frac{q_i - q_j}{q_i + q_j}, \quad t_{ij} = \frac{2q_i}{q_i + q_j}. \tag{4.24}$$

If the magnetic field component is perpendicular, the Fresnel coefficients read

$$r_{ij} = \frac{\tilde{n}_j^2 q_i - \tilde{n}_i^2 q_j}{\tilde{n}_j^2 q_i + \tilde{n}_i^2 q_j}, \quad t_{ij} = \frac{2\tilde{n}_i \tilde{n}_j q_i}{\tilde{n}_j^2 q_i + \tilde{n}_i^2 q_j}. \tag{4.25}$$

In the case coherent light incidents from the left side (E_0^+), q_j is given by

$$q_j \quad = \quad \sqrt{\tilde{n}_j^2 - n_0'^2 \sin\alpha}, \tag{4.26}$$

This equation requires the angle of incidence α at the first layer as well as the real refraction index of the surrounding ambient atmosphere n_0'. Despite the uncommon definition, Eqns. (4.23) to (4.26) represent the common Fresnel equations used in geometric optics [92].

The imaginary part of the complex refraction index defines the absorbance of light. It is used to define the layer matrices $\boldsymbol{L}_j$ which therefore describe interference and absorption effects [92],

$$\boldsymbol{L}_j = \begin{bmatrix} \exp(-i\frac{2\pi}{\lambda} q_j d_j) & 0 \\ 0 & \exp(i\frac{2\pi}{\lambda} q_j d_j) \end{bmatrix}. \tag{4.27}$$

The number of absorbed photons $G(x)$ is derived from Eqn. (4.22) by separating the scattering matrix $\boldsymbol{S}$ at layer j,

$$\begin{bmatrix} E_0^+ \\ E_0^- \end{bmatrix} = \boldsymbol{S}_j' \boldsymbol{L}_j \boldsymbol{S}_j'' \cdot \begin{bmatrix} E_m^+ \\ E_m^- \end{bmatrix}. \tag{4.28}$$

All matrices on the left side of layer j are summarized in the scattering matrix $\boldsymbol{S}_j'$, all contributions on the right side to $\boldsymbol{S}_j''$. This enables the transformation of the incident light on the solar cell into the share that enters and leaves layer j,

$$\begin{bmatrix} E_{j-1}^+ \\ E_{j-1}^- \end{bmatrix} = \boldsymbol{L}_j \cdot \begin{bmatrix} E_j^+ \\ E_j^- \end{bmatrix}. \tag{4.29}$$

The total electric field generated by an electromagnetic wave at the location x corresponds to the sum of the electric field components propagating in either direction. It is obtained by separating $\boldsymbol{L}_j$ at $0 \leq x \leq d_j$,

$$E_j(x) = E_j^+(x) + E_j^-(x) = E_{j-1}^+ \exp\left(i\frac{2\pi}{\lambda}q_j x\right) + E_j^- \exp\left(i\frac{2\pi}{\lambda}q_j(d_j - x)\right). \tag{4.30}$$

The number of photons absorbed $Q_j(x)$ generated by the dissipated electric field is given by [92, 95]

$$Q_j(x) = 0.5c\varepsilon_0 \frac{4\pi\kappa_j}{\lambda} n_j' \left|E_j(x)\right|^2. \tag{4.31}$$

The speed of light is denoted by c. The total generation rate $G(x)$ is obtained by integrating the amount of absorbed photons over all wavelengths in the incident light spectrum. For most simulations it is appropriate to assume that each photon absorbed generates an exciton in the active layer.

Additional details on the derivation of the transfer matrix formalism in solar cells can be found in Ref. [95]. More general overviews are given in Refs. [92–94].

Interference effects do not have a strong influence on the current–voltage characteristics of organic solar cells if the device thickness remains unchanged. Compared with spatially averaged generation rates, only minor differences have been observed. It therefore can be useful to assume constant generation rates in order to reduce the complexity of a simulated device.

4.7. Iterative solving scheme

Current–voltage characteristics of organic solar cells can be calculated by applying the presented approaches. It should not be forgotten that poorly set parameters such as the discretization with h will tremendously influence the simulation accuracy. A detailed knowledge of the limitations of the presented approaches is therefore useful. The calculation scheme used is outlined in Fig. 4.2. The optical simulation is optional and simpler models such as averaged generation rates can be used.

The electric potential distribution, as well as the charge carrier distributions, are guessed at first to initialize the equation system. The Poisson equation is solved according to the Gummel method. Since this approximation includes truncated Taylor series, the Gummel method has to be iteratively repeated until the residual error $\delta\Psi$ is lower than an acceptable convergence criterion ε.

After the electric potential is determined, the corresponding charge carrier distributions are calculated according to the Scharfetter-Gummel approach. This adjusts the charge carrier density distributions according to the drift–diffusion equations and the system has to be iteratively restarted from the beginning. The scheme is repeated until the charge carrier densities converge and a valid solution is obtained.

Starting with this result, the boundary conditions are changed to consider for example changes in illumination or applied voltage. Changes in the applied voltage have to be smaller than the thermal potential $V_t = k_B T/q$ in order to maintain a stable convergence behavior. The generation rate G is adjustable without restriction [33].

The simulation is also applicable to transient conductivity experiments. Time dependent solutions are found through the difference between the steady state solution $n(t=0)$ and $n(t)$ as defined in the continuity equations (Eqns. (4.4)) [85]. Transient simulations have not been used in the scope of this thesis.

The presented simulation program was implemented in the C++ programming language as a fast and platform independent software had been requested. Due to the object orientation, it was possible to build a modularized differential equation solver. This allows a simple definition of new models as well as cascading multiple models to describe complex physical interactions. OpenMP support was included for parallelized calculations on multiple computer cores. For multidimensional parameter fits, a differential evolution algorithm was implemented [96]. An optional graphical user interface was developed by C. Wick. The simulation is currently available for Windows and OsX operating systems.

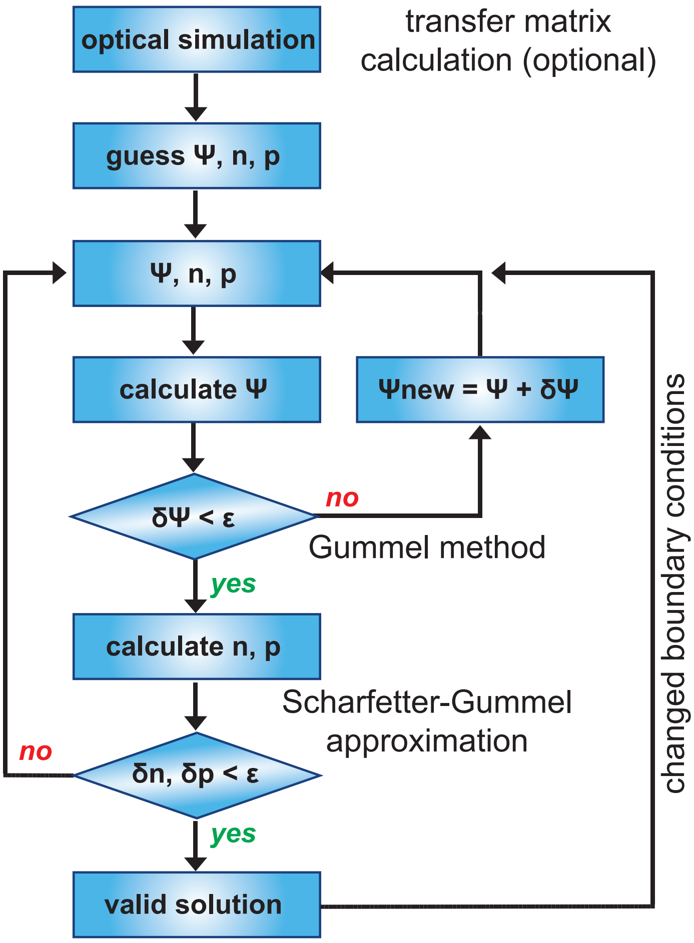

Figure 4.2.: Iterative solving scheme. The simulation begins with distributions of electric potential Ψ, electron n and hole p density initially being guessed. First, the electric potential is adjusted to the given charge carrier distributions according to the Poisson equation. Thus, the Gummel method is iteratively repeated until the difference between the old and new solution $\delta\Psi$ is smaller than an acceptable convergence criterion ε. Second, the continuity equation is solved using the Scharfetter–Gummel approximation. The calculation is repeated until the charge carrier densities converge. The calculation of an optical generation profile is optional. Starting with a valid steady state solution, the boundary conditions can be changed in order to simulate current–voltage characteristics or time transients.

Part II.

Results

5. Open circuit voltage of planar and bulk heterojunction solar cells

In addition to the short circuit current and the fill factor, the open circuit voltage is one key parameter of an organic solar cell optimization. Limited by the charge carrier mobilities, charge carrier densities, recombination rates or injection barriers, V_{oc} is the topic of many detailed investigations [39, 97–99]. An optimization of V_{oc} could help to increase the power conversion efficiency of the device. Since two different solar cell architectures are available, the question is raised of which device layout is advantageous for specific applications.

Generally, V_{oc} is known to be a function of the effective band gap E_g, but is significantly lower [99]. When the work functions of the electrodes of BHJ solar cells are changed, seemingly contradictory impacts on the yielded V_{oc} were found. Some experiments with BHJ solar cells claimed a linear dependence of V_{oc} on the electrodes work functions [99–101] whereas others yielded injection barrier independent results [102, 103]. In contrast, V_{oc} of PHJ solar cells was always observed to be independent of the selected electrodes [97]. Analytic approximations for an injection barrier independent V_{oc} exist for both device types [97, 98].

The fact that V_{oc} is always 0.3 to 0.5 V lower than E_g at room temperature led to various explanations. From absorption measurements, E_g was attributed to charge transfer states with a lower gap than the band gap of free charge carriers [104, 105]. Additional contributing effects which limit V_{oc} were assigned to recombination in the bulk of the semiconductor as well as charge carrier diffusion [100, 104, 106, 107]. However, a complete explanation of the impact of all losses on V_{oc} has not yet been presented.

The relation between the open circuit voltage, the device architecture and the corresponding losses is discussed in this chapter. A numeric fit to a set of measured current–voltage characteristics in dark and illuminated conditions is calculated for both device architectures. Different slopes of V_{oc} with increasing illumination intensity result in an intersection of the observed V_{oc} curves.

In the subsequent part, the fundamental parameters responsible for limiting V_{oc} are studied. Different regimes of V_{oc}, only some of which depend on the injection barriers, are found for both device architectures. Going beyond known models, the basic limitations for V_{oc} are separated and an analytical model for calculating V_{oc} is presented.

Finally, an evaluation of temperature dependent V_{oc} measurements is presented, demonstrating the application of the found relations.

5.1. Experimental

The current–voltage characteristics of BHJ and PHJ solar cells were measured in order to extract a valid parameter set for simulations. The solar cells were processed on structured ITO substrate, which was successively cleaned in water, acetone and isopropyl. After a

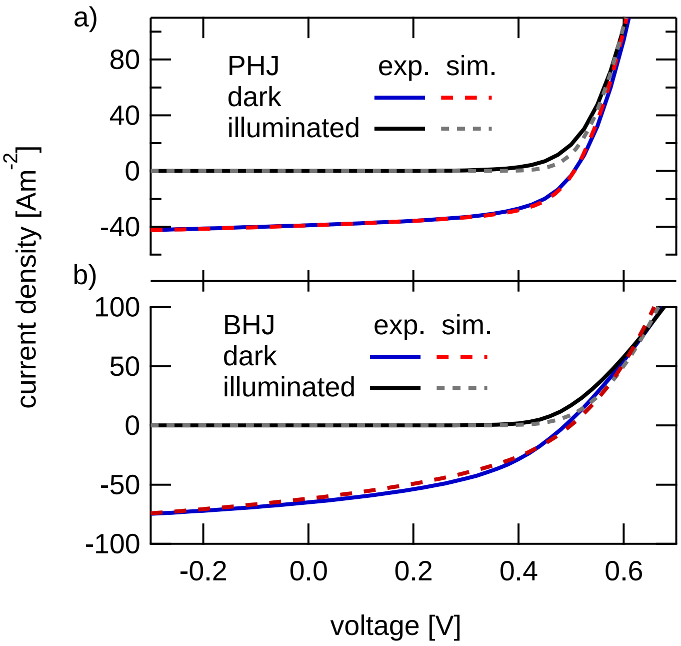

Figure 5.1.: Measured and fitted current–voltage characteristics of a PHJ (a) and a BHJ (b) solar cell. A single parameter set was used for the simulation.

15 minutes UV-ozone treatment, an organic bathocuproine (BCP) hole transport layer was evaporated. In order to create comparable organic solar cells, both device types were produced by a vacuum deposition of CuPc (donor) and C_{60} (acceptor) within a single run. The thicknesses of the active layers were measured to 25/25 nm for the PHJ and 50 nm for the BHJ device. The blend ratio of the BHJ active layer was set to 1:1. A silver (Ag) electrode was deposited on top. A white high power light emitting diode, calibrated by an AM1.5 sun simulator, was used to illuminate the devices. The samples were produced by D. Cheyns from IMEC and measured by A. Förtig [108]. The retrieved current–voltage characteristics are depicted in Fig. 5.1. The illumination intensity dependent V_{oc} is shown in Fig. 5.2.

The simulation was used to simultaneously fit the measured current–voltage characteristics with a single set of parameters. The generation rate of excitons was calculated with an AM1.5 spectrum. At donor–acceptor heterojunctions, excitons are converted into polaron pairs within 100 fs. Their diffusion was calculated assuming an exciton lifetime of τ_x = 1 ns and a diffusion constant of D_x = 0.025 m^2/s. The decay of excitons did not limit the generation of polarons pairs. The separation of polaron pairs was set to be a function of the local electric field according to the Onsager–Braun theory. Free polarons form polaron pairs during their recombination. The corresponding rate was given by the Langevin theory [60].

The measured thickness of the BHJ solar cell had to be shortened by 5 nm during the fitting process in order to yield comparable results. However, this adjustment is still within a reasonable regime considering the included experimental and theoretical errors. The relatively high injection barrier at the anode of $\Phi_p = 0.25$ eV was roughly estimated by the V_{oc} vs. temperature dependence described in Section 5.6 [109]. The obtained fit parameters are listed in Tab. 5.1 and are all within a reasonable range of previous experimental findings [110]. The absolute value of the decay rate k_F should not be overestimated since it includes microscopic parameters instead of directly measurable parameters, for instance high local mobilities which are required for effective charge carrier separation [111, 112]. The data on the complex refraction index as well as the charge carrier mobilities was provided by our partners from IMEC. The calculated generation rate of the BHJ solar cell was adjusted by a factor of 0.71 so as to fit the measured short circuit current. This might be caused by an inaccurately set exciton diffusion constant. The direct comparison between fitted and measured current–voltage characteristics is shown in Fig. 5.1.

parameter	symbol	CuPc	C_{60}	CuPc:C_{60}	unit
temperature	T	300	300	300	K
LUMO energy	E_{LUMO}	-3.0	-4.05	-4.05	eV
HOMO energy	E_{HOMO}	-5.1	-6.15	-5.1	eV
layer thickness	L	25	25	45	nm
balanced mobilities	μ_n, μ_p	1.7×10^{-8}	3.0×10^{-6}	3.0×10^{-9}	V/m^2
relative dielectric permittivity	ε_r	3.4	4.0	3.4	
effective density of states	N_c, N_v	5.0×10^{26}	5.0×10^{26}	5.0×10^{26}	1/m^3
Onsager–Braun theory:					
- binding distance	a	1.2	1.2	1.2	nm
- decay rate	k_F	1.4×10^{-5}	1.4×10^{-5}	1.4×10^{-5}	1/s
electrodes:					
- anode	$E_{ITO/BCP}$	-4.848	—	-4.848	eV
- cathode	E_{Ag}	—	-4.05	-4.05	eV

Table 5.1.: Simulation parameters for CuPc:C_{60} solar cells. The parameters were retrieved by a simultaneous fit to measured current–voltage characteristics of PHJ and BHJ devices.

5.2. Comparison of V_{oc} in bulk and planar heterojunction solar cells

At an illumination intensity of 1 sun, both devices yield comparable power conversion efficiencies of 1.1 % for the PHJ device and 1.4 % for the BHJ solar cell. However, the BHJ solar cell shows a higher V_{oc} compared to the PHJ device at illumination levels below 0.3 suns, and vice versa above (Fig. 5.2). This trend is well reproduced by the simulation as shown in Fig. 5.3 (a).

Mathematically V_{oc} can be expressed for both device architectures as the effective band gap E_g, reduced by all potential losses. These losses include injection barriers Φ_n and Φ_p as well as an energy loss E_{loss} caused by an electric field in the device,

$$qV_{oc} = E_g - \Phi_n - \Phi_p - E_{loss}. \tag{5.1}$$

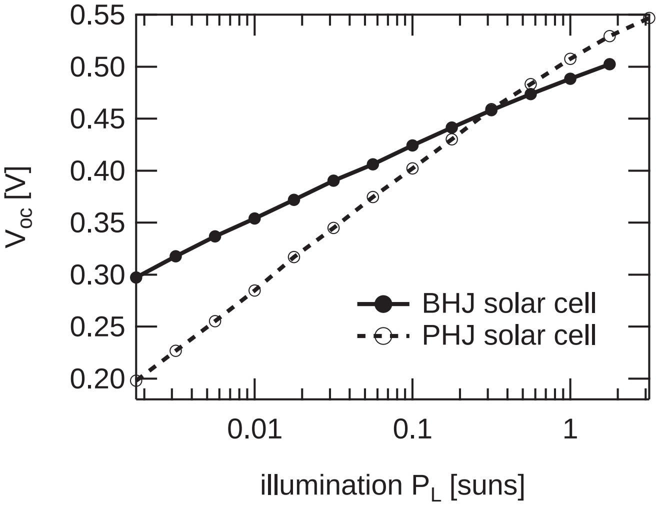

Figure 5.2.: Measured open circuit voltages for different illumination intensities. The PHJ solar cell shows a significantly higher V_{oc} than the BHJ device above 0.3 suns and vice versa at lower values.

This approach is based on a simple energetic picture. V_{oc} of organic solar cells is often described as an energy difference between both quasi-Fermi energies. According to Eqns. (3.7) and (3.8), this difference is a function of the charge carrier densities as well as the effective band gap. E_g can consequently be used as a reference parameter to describe V_{oc}. The energy differences between the quasi-Fermi levels and the band energies must not fall below k_BT for a valid definition [13].

The V_{oc} of organic solar cells is extracted at the metal electrodes. This necessarily defines V_{oc} as the electric potential difference between anode and cathode. The potential difference differs from E_g by at least the value of the injection barriers under ideal flat-band conditions. Thus V_{oc} can be reduced by Φ_n and Φ_p.

In addition, the influence of the charge carriers and their recombination has to be considered. Charge carriers in the device generate an electric field $F(x)$ according to the Poisson equation (Eqn. (3.16)). The electric field can be transformed into an energy loss between both electrodes, E_{loss}, by a spatial integration,

$$E_{loss} = q\int_0^L F(x)\,\mathrm{d}x. \tag{5.2}$$

The electric field distribution $F(x)$ is determined by the drift–diffusion equations. The sum of electron and hole currents can be set to zero ($J_n + J_p = 0$) since the net current flow at open circuit conditions has to vanish,

$$qn\mu_nF + qD_n\frac{\partial n}{\partial x} + qp\mu_pF - qD_p\frac{\partial p}{\partial x} = 0. \tag{5.3}$$

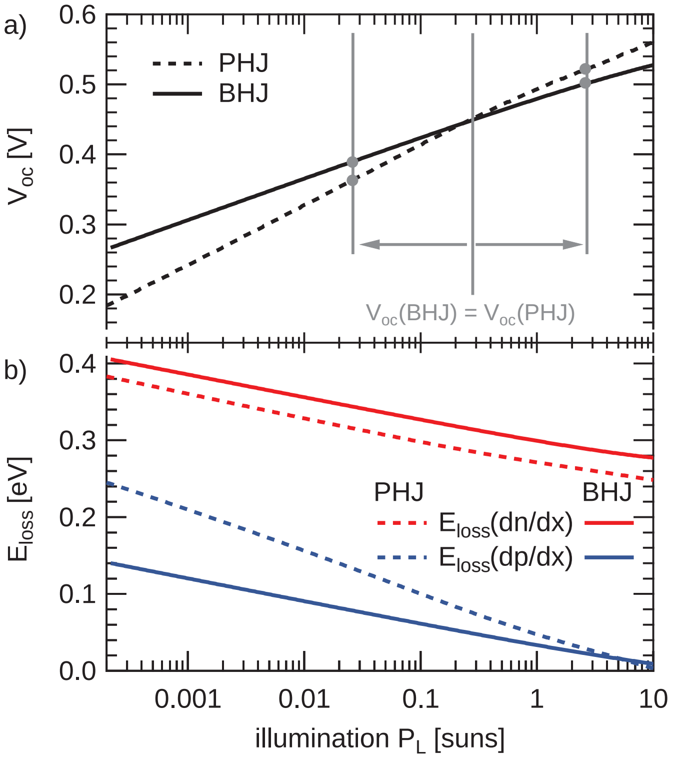

Figure 5.3.: Simulated V_{oc} (a) and energy losses (b) as a function of illumination in BHJ und PHJ solar cells. The vertical lines before and after the V_{oc} is crossed mark the intensities at which the charge carrier distributions are shown (Fig. 5.4). Due to a relatively high hole injection barrier (b) mainly the gradient of the electron density according to Eqn. (5.4) is accountable for the losses in the electric field.

Written in terms of the electric field, the overall lost energy reads

$$E_{loss} = -q \int_0^L \frac{D_n \frac{\partial n(x)}{\partial x} - D_p \frac{\partial p(x)}{\partial x}}{\mu_n n(x) + \mu_p p(x)} \, \mathrm{d}x. \tag{5.4}$$

Thus, V_{oc} is identified as a function of the charge carrier densities n, p, their gradients, the electron and hole mobilities μ_n, μ_p as well as the related diffusion constants D_n, D_p and the active layer thickness L. According to Eqn. (5.4), high charge carrier density gradients are responsible for losses of V_{oc} whereas high charge carrier densities increase the open circuit voltage. In order to pinpoint the origin of the measured V_{oc} vs. light intensity dependence, the integral of Eqn. (5.4) can be separated into two parts: one for each of the derivative of electrons and holes. The denominator of both the separated integrals is identical. The results are shown in Fig. 5.3 (b). The corresponding charge carrier profiles for BHJ and PHJ devices are presented in Fig. 5.4 in the dark as well as for the two light intensities marked in Fig. 5.3 (a) below and above the light intensity which generated equal V_{oc} values.

The BHJ device has a higher open circuit voltage at low light intensities. However, due to the lesser slope of V_{oc} vs. illumination in comparison with the PHJ solar cell, the BHJ

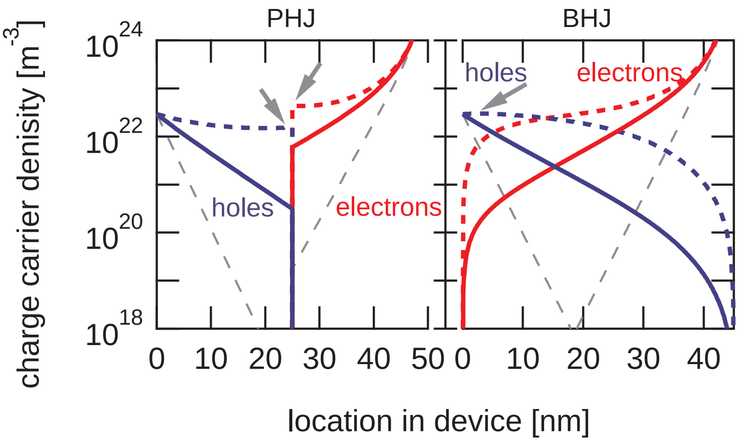

Figure 5.4.: Charge carrier density distribution due to photogeneration and injection for a PHJ (left) and a BHJ (right) device at zero (thin dashed lines), low (solid lines) and high (dashed lines) illumination intensity, corresponding to the leftmost and rightmost markers in Fig. 5.3. With increasing light intensity, charges are accumulated at the heterointerface in contrast to the fixed boundary conditions at the electrodes. At high illumination levels, space charge regions marked by grey arrows can be observed.

device has the lower V_{oc} above 0.3 suns (Fig. 5.3 (b)). The charge carrier concentration profiles (Fig. 5.4) show a fundamental difference. Holes and electrons in PHJ solar cells are well separated from each other. Minority charge carriers, i.e., electrons in the p-conducting material as well as holes in the n-conducting material, possess a charge carrier density of not more than 10^5 m^{-3}. In contrast, charge carriers in BHJ solar cells reside together in one effective medium with a high concentration of both charge carrier types across the whole extent of the device. This leads to a slightly higher overall charge carrier density in BHJ solar cells compared to PHJ devices.

A metal electrode generally injects electrons as well as holes into a semiconductor. This injection is described as thermal activation in terms of the thermionic emission theory (Eqns. (3.12) and (3.13)). The ratio between injected electrons and holes is consequently an exponential function of the offsets between the metal work function and the LUMO and HOMO levels of the semiconductor. For the anode, where holes are the majority charge carriers, this can be stated as

$$p \propto \exp(-\Phi_p) \quad \text{and} \quad n \propto \exp(-E_g + \Phi_p). \tag{5.5}$$

Hence, in Fig. 5.4 the rightmost and leftmost charge carrier densities (i.e. at the electrodes) are constant for all illumination levels. Photogenerated charge carriers are accumulated inside the active layers, especially in proximity of the donor–acceptor heterointerface.

The BHJ solar cells are described by an effective medium with an effective band gap E_g. The injection of majority carriers at the anode therefore corresponds to hole injection into CuPc, whereas the minority carriers at this interface are electrons injected into C_{60}. In contrast, only one of the two photoactive materials is adjacent to a given electrode in PHJ devices, e.g. CuPc (anode). Thus, while the majority (hole) injection barrier corresponds to the BHJ case, the minority carriers have a larger injection barrier of the whole CuPc band gap less Φ_p. Consequently, less minority charge carriers are present in a PHJ solar cell. The situation at the cathode is equivalent, considering that electrons are majorities there. The higher a certain injection barrier is, the lower the difference is between injected majority and minority charge carriers (see also Eqn. (5.5)).

The charge carrier profiles of BHJ and PHJ devices (Fig. 5.4) can be interpreted in terms of Eqn. (5.4). In PHJ devices, the type of majority charge carriers always changes at the heterointerface. Both majority charge carrier densities at this interface commonly differ due to the different properties of the neat semiconductor layers (compare to Fig. 5.4). In BHJ solar cells, the location where the majority charge carrier density type is changed is found at a random position at which electron and hole charge carrier density are equal. The difference between electron and hole majority charge carrier densities at the heterointerface in PHJ solar cells is filled with additional charge carriers in the BHJ device which shifts the point of equal electron and hole densities. The charge carrier densities in a BHJ solar cell are therefore higher and their slopes flatter at low light levels. The V_{oc} of BHJ solar cells consequently exceeds the V_{oc} of PHJ devices at illumination intensities below 0.3 suns.

With increasing light intensity, photogenerated charge carriers are accumulated faster at the donor–acceptor heterojunction than in the effective layer of a BHJ device where photogeneration is allowed within the whole extent of the active layer. In terms of V_{oc}, this leads to a weaker charge carrier gradient in PHJ solar cells, a stronger reduction of the energy loss (Fig. 5.3 (b)) and an open circuit voltage exceeding that of the BHJ device at intensities above 0.3 suns (Fig. 5.3 (a)).

Above an illumination intensity of one sun, space charges start piling up in both device architectures. Their location is indicated by arrows in Fig. 5.4. In the PHJ device, the space charge is built up at the CuPc/C_{60} interface due to the localized photogeneration. In BHJ solar cells, the space charge region forms at the anode with its small injection barrier. Thus, the open circuit voltage and, potentially, also the short circuit current is further lowered.

5.3. Basic derivation of V_{oc}

The generic difference between the two device architectures can be used to derive an analytical estimation of V_{oc}. A basic expression for V_{oc} of PHJ solar cells was found by Cheyns et al. [97] if electrons and holes are solely located in the acceptor and donor phase, respectively. This is shown in Fig. 5.4 with respect to the exponential charge carrier density axis. The amount of electrons and their gradients in the C_{60} layer are orders of magnitudes higher than the corresponding values for holes. In the CuPc phase, this electron–hole ratio is inverted. Hence, Eqn. (5.4) can be separated at the heterointerface and simplified by neglecting influences of minority charge carriers. Assuming the validity of the Einstein relation, this yields

$$E_{loss} = \begin{cases} k_B T \int\limits_{0}^{x_{int}} \frac{\partial p}{\partial x} \frac{1}{p}\, \mathrm{d}x = k_B T \Big[\ln(p) \Big]_{0}^{x_{int}} & \text{p-phase (CuPc)} \\ -k_B T \int\limits_{x_{int}}^{L} \frac{\partial n}{\partial x} \frac{1}{n}\, \mathrm{d}x = -k_B T \Big[\ln(n) \Big]_{x_{int}}^{L} & \text{n-phase (C}_{60}\text{).} \end{cases} \tag{5.6}$$

The open circuit voltage can therefore be calculated by the amount of electrons and holes at the electrodes and at the heterointerface. The spatial location of the heterointerface between the device extent 0 and L is indicated by x_{int}. Since the electron and hole charge carrier densities are mainly optically generated at the donor–acceptor interface, they are referred to as n_o and p_o. The charge carrier densities at the electrodes are given by the thermionic emission theory (Eqns. (3.12) and (3.13)). The total energy lost due to the charge carrier distributions reads

$$E_{loss} = k_B T \left\{ \Big[\ln(p)\Big]_0^{x_{int}} - \Big[\ln(n)\Big]_{x_{int}}^{L} \right\} \tag{5.7}$$

$$= k_B T \left\{ \ln\left(N_v \exp\left(-\frac{\Phi_p}{k_B T}\right)\right) + \ln\left(N_c \exp\left(-\frac{\Phi_n}{k_B T}\right)\right) - \ln(n_o p_o) \right\}. \tag{5.8}$$

The latter equation can be inserted in Eqn. (5.1), which results in

$$qV_{oc} = E_g - \Phi_n - \Phi_p - E_{loss} \tag{5.9}$$

$$= E_g - k_B T \ln\left(\frac{N_c N_v}{n_o p_o}\right). \tag{5.10}$$

Consequently, V_{oc} is defined by the effective band gap, the effective charge carrier densities and the amount of optically generated charge carriers at the heterointerface, but not by the injection barriers [97]. The injection barriers cancel out during the transformation of Eqn. (5.9) in Eqn. (5.10). Simulations show that this statement is only valid in a certain regime of small injection barriers. Therefore, a more general model is required.

The V_{oc} of BHJ solar cells can be defined accordingly. The density of electrons and holes is equal at a certain location x_{int} inside the solar cell. At this point, the local current flow can be expected to be zero in good approximation. Thus, the charge carrier density is solely defined by charge carrier generation as well as recombination according to the continuity equations (Eqns. (3.36) and (3.37)). For an arbitrary recombination rate defined by $R = k_F(np - n_i^2)$, the product of optically generated charge carriers $n_o p_o$ is determined by

$$\frac{1}{q}\frac{\partial J_n}{\partial x} = G - k_F(n_o p_o - n_i^2) = 0, \tag{5.11}$$

$$n_o p_o = \frac{G}{k_F} + n_i^2. \tag{5.12}$$

In the case of a Langevin recombination, k_F has to be substituted by the Langevin prefactor γ. Inserted in Eqn. (5.10), this defines an injection barrier independent V_{oc} for BHJ devices,

$$qV_{oc} = E_g - k_B T \ln\left(\frac{N_v N_c}{\frac{G}{k_F} + n_i^2}\right). \tag{5.13}$$

A similar result was presented by Koster at al. [98].

5.4. Open circuit voltage of organic BHJ solar cells

Even though V_{oc} was predicted to be independent of the injection barriers, simulations show contrary results for both device types. V_{oc} as a function of the anode injection barrier is shown in Fig. 5.5. The parameter set for the simulated BHJ device was slightly changed in contrast to the parameter set given in Tab. (5.1). A direct generation of free charge carriers was used instead of the Onsager-Braun model. The generation rate was set to $G = 3.76 \cdot 10^{28}\ \mathrm{m}^{-3}\mathrm{s}^{-1}$, which is the spatially averaged generation rate at one sun illumination. The recombination was described according to the Langevin theory.

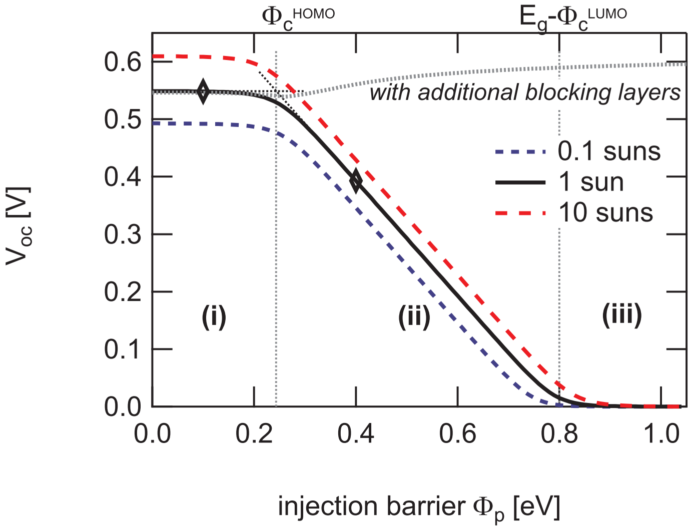

Figure 5.5.: Open circuit voltage of a BHJ solar cell as a function of the anode injection barrier. Three regimes are found: A constant V_{oc} (i) is found for low injection barriers. At higher values (ii), a linear reduction of V_{oc} is observed until a second saturation plateau (iii) at zero is reached. The transition between the regimes is assigned to the critical injection barriers Φ_c^{LUMO} and Φ_c^{HOMO}. V_{oc} is not decreased if an electron blocking layer is applied at the anode. Band structures and charge carrier distributions at the black diamond markers are given in Fig. 5.7.

Three different V_{oc} regimes are found by changing the anode injection barrier as depicted in Fig. 5.5 [102]. A V_{oc} independent of the injection barrier is obtained for the small injection barriers in region (i). In a second regime (ii), a directly proportional decrease of V_{oc} with the injection barrier is observed. Lastly, V_{oc} saturates at zero in a third region (iii). The transitions between the single regimes are indicated by the gray vertical lines and are denoted as critical injection barriers Φ_c^{HOMO} and Φ_c^{LUMO}.

The critical injection barriers correspond to the ratio between injected majority charge carriers and the amount of optically generated charges as shown in Fig. 5.6 (a). The injected charge carrier density exceeds the optical generation by orders of magnitude for low injection barriers (i) and a constant V_{oc} is yielded. Conversely, if the amount of optically generated charge carriers exceeds the injected charge carrier density (ii), V_{oc} linearly decreases with the injection barrier. In regime (iii), the metal work function approaches the semiconductor LUMO energy. The offset is comparable to that of region (i), however in relation to the

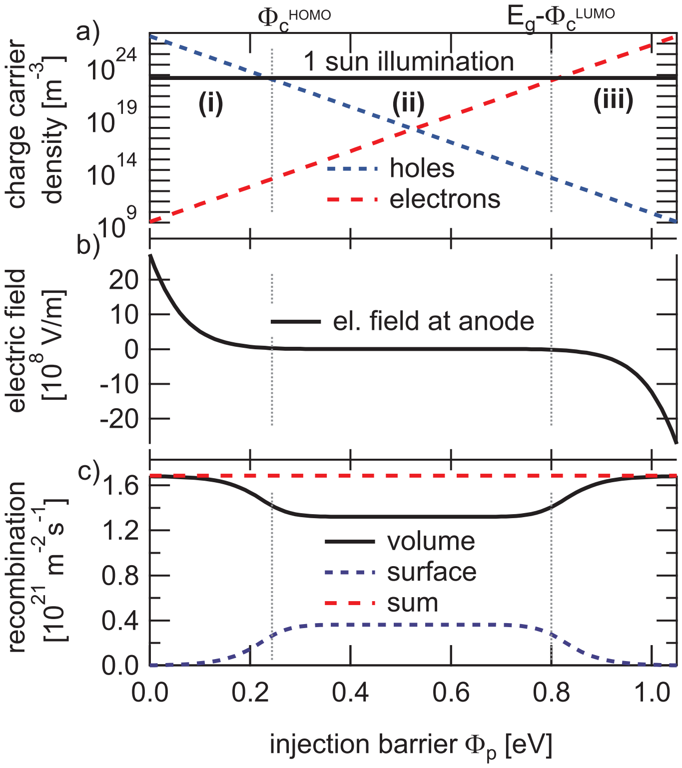

Figure 5.6.: Origin of the different V_{oc} regimes. If V_{oc} is saturated in region (i) and (iii), the amount of injected charge carriers (a) exceeds the density of optically generated charge carriers in the active layer. Due to the high charge carrier gradient a band bending (b) is generated in the regimes (i) and (iii) in proximity to the anode. In regime (ii), the injection barriers are dominant, which leads to a flat band around the particular contact. Due to the decreasing electric field an increasing surface recombination (c) is observed which is highest in region (ii). The amount of charge carriers recombined in the volume decreases since the sum of both rates must equal the generation rate in thermal equilibrium. In order to compare bulk and surface recombination, the bulk recombination was normalized to a surface recombination by dividing the given rate by the device thickness.

LUMO band instead of the HOMO band. Thus, an equivalent condition as in region (i) is created.

For injection barriers of 0.1 and 0.4 eV, marked in Fig. 5.5 by diamond symbols, the corresponding band structures and charge carrier density distributions are depicted in Fig. 5.7. In regime (i), a band bending BB_p is observed at the anode which vanishes in regime (ii). The electric field close to the anode is also depicted in Fig. 5.6 (b) and corresponds to this band bending. In order to retrieve the constant V_{oc} in regime (i), the sum of band bending and injection barrier must be constant. This was implicitly predicted by Eqn. (5.13).

The recombination rates are influenced by band bending. At low injection barriers, the high electric field inhibits minority charge carriers from diffusing into the metal electrodes (compare to Fig. 5.7 (a)). Since at V_{oc} conditions electrons and holes must be simultaneously transported, a surface recombination at the electrodes is minimized and the recombination of

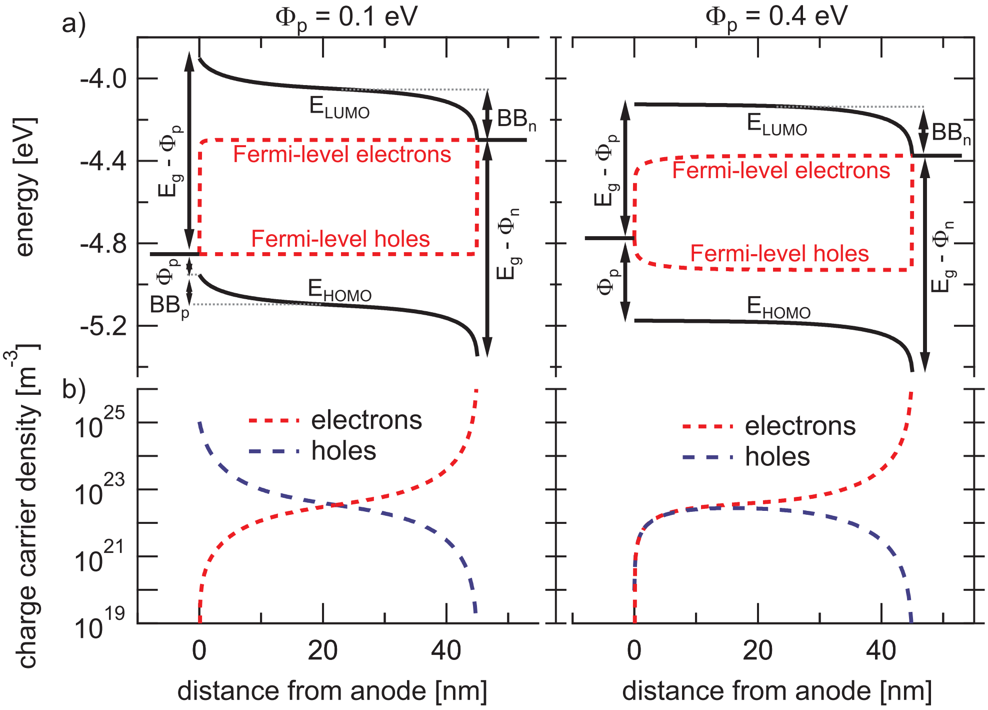

Figure 5.7.: Band structures (a) and charge carrier density distributions (b) for two injection barriers of 0.1 and 0.4 eV at an illumination intensity of 1 sun. A V_{oc} independent of the injection barrier is generated if the injected charge carrier densities exceed the optically generated charges (left). This generates a band bending (BB) close to the electrodes. For higher injection barrier (right), the optically generated charge carrier density exceed the injected charge carrier density which results in a vanishing band bending (BB_p) and flat-band conditions around the anode.

charge carriers is located mostly in the bulk of the active layer as depicted in Fig. 5.6 (c). With an increasing injection barrier, the band bending is reduced or even inverted and a significant diffusion of minority and majority charge carriers into the anode and a subsequent surface recombination is observed. Since in thermal equilibrium the generation rate must be equal to the recombination rate, the sum of the recombination is constant. The V_{oc} in regime (ii) is directly limited by the injection barriers.

Critical injection barrier

The critical injection barrier (at the anode) is determined by the injected majority charge carrier density (holes) at the anode p_{th} and the optically generated (hole) charge carrier density at a certain location in the device p_o,

$$p_{th} = p_o. \tag{5.14}$$

Electron and hole density are equal at the latter mentioned position. Any optical excitation generates an equal amount of electrons and holes. Thus, the latter equation can be modified to

$$p_{th} = \sqrt{n_o p_o}. \tag{5.15}$$

Through this transformation, Eqn. (5.12) can be used to determine the optically generated charge carrier density p_o. The injected charge carrier density p_{th} is defined by the thermionic emission theory (Eqn. (3.15)). Consequently, we retrieve

$$N_v \exp\left(-\frac{\Phi_p}{k_B T}\right) = \sqrt{\frac{G}{k_F} + n_i^2}. \tag{5.16}$$

Written in terms of the injection barrier, the critical injection barrier for an anode Φ_c^{HOMO} is

$$\Phi_c^{HOMO} = -k_B T \ln\left(\frac{\sqrt{\frac{G}{k_F} + n_i^2}}{N_v}\right). \tag{5.17}$$

For an equivalent calculation for a cathode with a Fermi level closer to the LUMO energy instead to the HOMO level, N_v has to be replaced by N_c to yield Φ_c^{LUMO}.

The critical injection barrier denotes the minimum loss of electric potential a solar cell has to suffer due to a metal electrode. This minimum loss is generated by injected charge carriers which diffuse into the solar cell and generate an electric field. If an injection barrier is smaller than the critical barrier, the critical injection barrier has to be subtracted from E_g. If the optically generated charge carrier density exceeds the injected charge carrier density, the influence of band bending vanishes due to the homogeneous optical generation. E_{loss} approximates zero and, according to Eqn. (5.9), the actual injection barrier has to be subtracted from E_g.

The maximum yieldable V_{oc} of an organic solar cell in region (i) is therefore defined as

$$qV_{oc} = E_g - \Phi_c^{HOMO} - \Phi_c^{LUMO}. \tag{5.18}$$

The latter definition is equivalent to Eqn. (5.13). However, the influence of each metal–semiconductor interface is separated. The result of Eqn. (5.18) is compared to simulated V_{oc} vs. injection barrier dependences for several charge carrier mobilities in Fig. 5.8. Differences between both methods are observed especially for higher charge carrier mobilities. They originate from local currents which were neglected in the derivation of Eqn. (5.18). Even though the determination of the critical injection barrier is therefore error-prone, it can be used to approximate the maximum V_{oc} yieldable from an organic solar cell.

Implications for BHJ solar cells

For an interpretation of experimental results as well as an optimization of organic BHJ solar cells, the formalism found allows several relevant conclusions. Assuming a certain effective energy gap E_g, the retrieved V_{oc} is limited due to the charge carrier gradient between injected charges at the electrodes and the charge carrier density in the device. For injection barriers smaller than the critical injection barrier (i), this results in an injection barrier independent and constant potential loss. This constant loss is well known in literature with values between 0.3 eV and 0.5 eV stated in many publications, e.g. in Ref. [39, 99]. For the C_{60}:CuPc solar

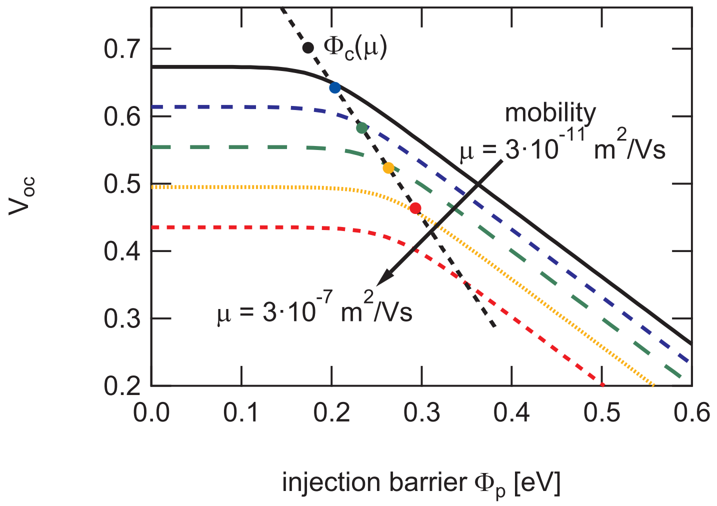

Figure 5.8.: Injection barrier dependent V_{oc} for different balanced charge carrier mobilities. The charge carrier mobility is decupled between each line. The critical injection barrier can be used to estimate the transition point between the regimes (i) and (ii) in Fig. 5.5. The determination of Φ_c is error-prone due to neglected drift and diffusion currents.

cell used in this chapter, this intrinsic loss was calculated to be 0.5 V at room temperature and an illumination intensity of one sun. Additional limiting contributions might exist [113].

For injection barriers exceeding the critical injection barrier (ii), the diffusion of injected charge carriers into the semiconductor is maximized. The metal electrodes within this regime act as recombination centers, diminishing the stored charge carrier density through surface recombination. Since E_{loss} approaches zero due to the low charge carrier gradients, V_{oc} decreases linearly with the injection barriers. Additional blocking layers are able to maintain V_{oc} (Fig. 5.5).

Due to the distinct regimes, experiments have been interpreted with contradicting models. A Fermi level pinning could be concluded if V_{oc} appears to be independent of the electrodes work function. However, linear dependences have also been measured [99, 113]. Both results are in agreement with the presented model and can be attributed to the influence of injection barriers on V_{oc}.

5.5. Open circuit voltage of PHJ solar cells

In analogy to the BHJ solar cell, this formalism can be applied to PHJ devices as well. Certain assumptions have to be refined due to the different device architecture. An exemplary PHJ band structure is shown in Fig. 5.9. In contrast to the BHJ device, the effective band gap E_g is only defined directly at the heterojunction interface. The effective band gap is correlated to the optical band gaps of the neat semiconductors E_{gp} and E_{gn} by the energy offsets ΔE_{LUMO} and ΔE_{HOMO}. Thus, each injection barrier solely refers to one material. The injection of minority charge carriers is restrained due to the larger band gap of the neat materials. In contrast to the parameters given in Tab. 5.1, the LUMO level of CuPc was set to -3.6 eV for the simulation.

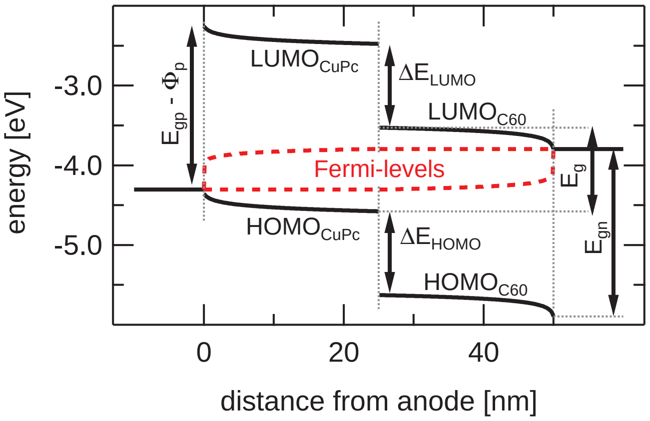

Figure 5.9.: Energy band structure of a PHJ device. In addition to the band bending at the injection barriers equivalent to the BHJ solar cell (Fig. 5.7) the bilayer device possesses two discrete semiconductive layers with independent optical band gaps E_{gp} and E_{gn}. Each injection barrier refers to only one material. The effective band gap E_g is solely defined directly at the heterojunction interface. The energetic offsets which connects the effective with the optical band gaps are denoted by ΔE_{LUMO} and ΔE_{HOMO}.

The influence of an increased anode injection barrier is shown in Fig. 5.10 (a). A first (i1), but extended (i2) saturated V_{oc} level is observed similar to that of the BHJ device. It is followed by a linearly decreasing regime limited by the injection barrier (ii) until a second saturation region (iii) around zero is reached. The origin of the regimes is identical to the BHJ device except for in region (i2). Thus, similar to the BHJ device, the injected majority charge carrier densities intersect the optical generated charge carrier densities (Fig. 5.10 (b)).

In region (i2), a band bending in proximity to the anode does not exist (Fig. 5.10 (c)). However, V_{oc} remains constant which implies the absence of surface recombination. The device architecture splits excitons into electrons on the acceptor side of the heterojunction and holes on the donor side. Minority charge carriers in the neat materials are rare due to the high optical band gaps. Thus, even though an electric field (BB) does not hinder optically generated charge carriers to diffuse away from the heterointerface, missing minority charge carriers inhibit any charge transport at V_{oc} conditions. The generated charge carriers are stored within the solar cell and V_{oc} is maintained.

The only possibility to inject minority charge carriers at the heterointerface is through thermal activation over the energy band offsets ΔE_{LUMO} and ΔE_{HOMO}. For the anode contact, the thermally activated electron charge carrier density in CuPc at the heterointerface $n_{o(donor)}$ reads

$$n_{o(donor)} = n_o \exp\left(-\frac{\Delta E_{LUMO}}{k_B T}\right). \tag{5.19}$$

Only if the thermally activated minority charge carrier density at the heterojunction is identical to the injected majority current density ((Fig. 5.10) (b)), can a surface recombination current be established. Consequently, starting from a critical injection barrier Φ_c^{PHJ} (Fig. 5.10),

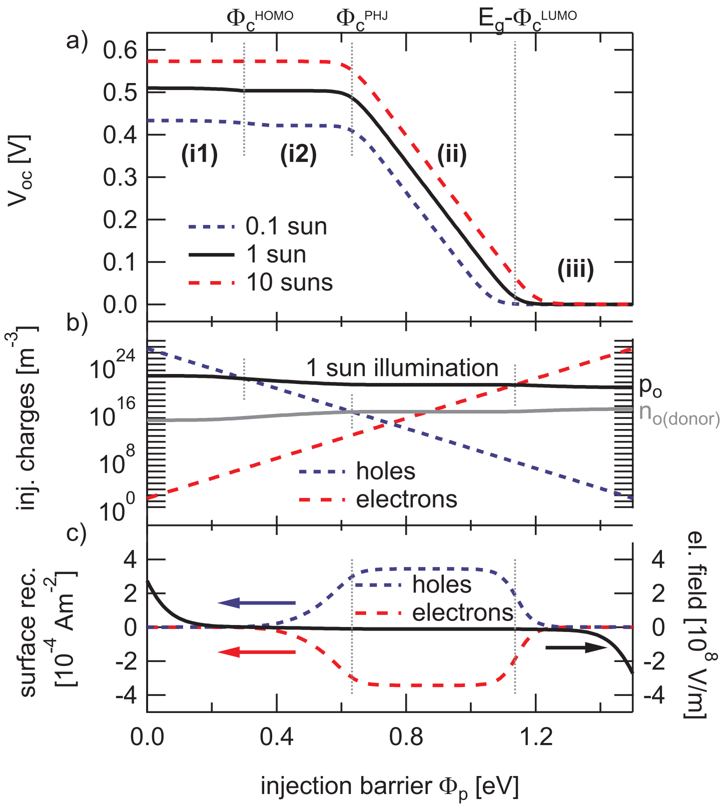

Figure 5.10.: Influence of the anode injection barrier on V_{oc} of a PHJ device. For different illumination levels (a), a comparable behavior to the BHJ solar cell is found. However, an additional extended V_{oc} plateau regime (i2) is observed which depends on the energy band offset ΔE_{LUMO}. For 1 sun illumination, the conditions which separate the different regimes are found by comparing the injected charge carriers (b) with the charge carriers densities at the heterointerface on the donor side (n_o, $p_{o(donor)}$). The surface recombination currents as well as the electric field close to the anode are shown in (c).

surface recombination is enabled and regime (ii) is reached,

$$\Phi_c^{PHJ} = \Delta E_{LUMO} + \Phi_c^{HOMO}. \tag{5.20}$$

An equivalent equation can be derived for the cathode. The result implies that PHJ solar cells possess an implicit surface passivation due to their bilayer structure. As long as the offsets between the energy bands ΔE_{LUMO} and ΔE_{HOMO} are high enough, PHJ devices will not show any influence of the injection barriers on V_{oc}. In contrast to certain assumptions in literature [97], PHJ solar cells however possess a dependence of the injection barriers on V_{oc}.

5.6. Application in experiments

In the previous sections, an equation system for determining the maximum yieldable V_{oc} of an organic solar cell was derived. The critical injection barriers were shown to be a function of the band gap, injection barriers, temperature and the charge carrier densities.

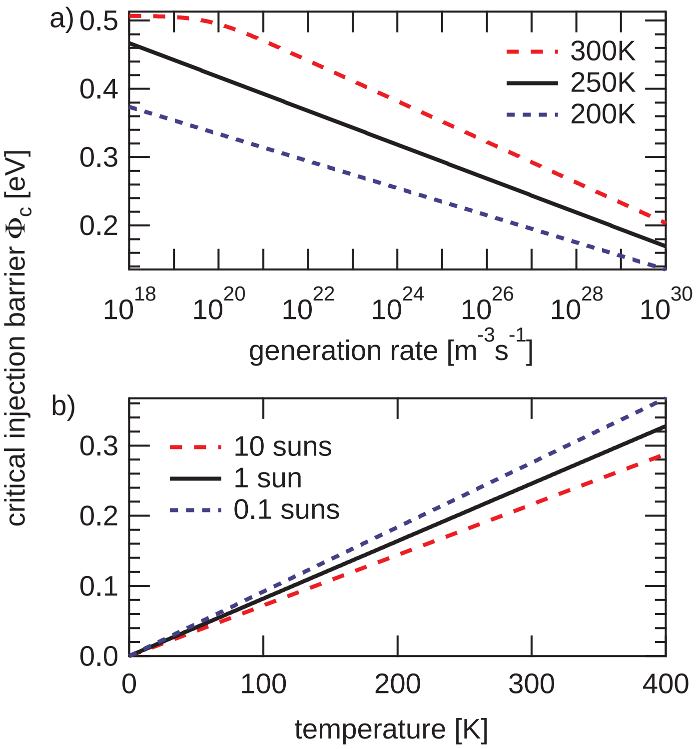

Figure 5.11.: Critical injection barrier of a BHJ solar cell according to Eqn. (5.17) for different (a) light intensities and (b) temperatures. The parameters of Tab. 5.1 were used for the simulation.

The critical injection barrier according to Eqn. (5.17) is shown in Fig. 5.11 for a bulk heterojunction solar cell. In order to obtain V_{oc}, the larger value, either the real or the critical injection barrier has to be subtracted from E_g for each electrode. The actual injection barriers are assumed to be independent of variations in temperature or illumination. Thus, kinks in the V_{oc} vs. temperature and illumination dependencies indicate transitions between critical and real injection barriers as dominating loss mechanism of V_{oc}. The high critical injection barrier will dominate V_{oc} especially at low generation rates and high temperatures. With decreasing temperature or increasing illumination, the critical injection barrier is reduced. This enhances V_{oc} until the real injection barrier is matched and V_{oc} saturates.

A measured example is shown in Fig. 5.12. The data was taken from three representative 200 nm thick P3HT:PC_{61}BM (1:1 ratio) and P3HT:bisPC_{61}BM (1:0.8 ratio) solar cells, which were assembled and measured by D. Rauh [109]. Patterned ITO coated glass which had been cleaned in solvents was used as substrate. On the substrate, an additional PEDOT:PSS blocking layer was spin coated and annealed for 10 minutes at 130° C. The active layers were subsequently spin coated from chlorobenzene solutions in a nitrogen atmosphere and likewise annealed. On top, a Ca (3 nm)/Al (100 nm), and respectively, a Cr (3 nm)/Al (100 nm) electrode were evaporated. Due to the different cathodes and acceptor materials, a variation of the effective band gap and the electron injection barrier was intended. The single materials were purchased from Rieke Metals (P3HT P200), Solene (PC_{61}BM, bisPC_{61}*BM*) and

CLEVIOS (PEDOT P VP AI 4082). The devices were illuminated using a 10 W white LED simulating an illumination intensity which is equivalent to 1 sun [109].

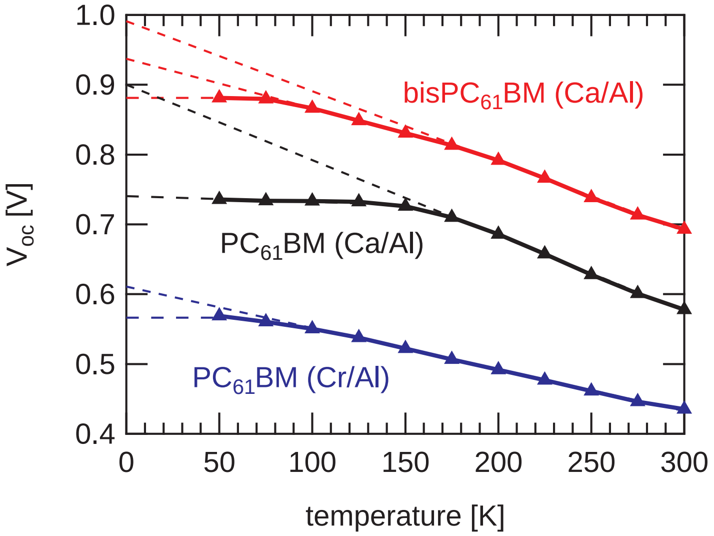

Figure 5.12.: Measured temperature dependent open circuit voltages of different BHJ solar cells. V_{oc} saturates at low temperatures to a maximum yieldable value according to Eqn. (5.18). The saturated V_{oc} is identical to the built-in potential V_{bi}. If the critical injection barriers exceed the actual injection barriers at higher temperatures, a linear decrease of V_{oc} is yielded. Extrapolations to $T = 0$ K enable a rough estimation of E_g as well as the injection barriers.

The saturated V_{oc} values at low temperatures shown in Fig. 5.12 indicate the built-in potential V_{bi}. The interpolations of the linearly decreasing regimes of V_{oc} with raising temperature yield the effective band gap at T= 0 K. Thus, an E_g of 1.0 eV for the bisPC$_{61}$BM:P3HT blend and 0.9 eV for the PC$_{61}$BM:P3HT blend is found. However, these extrapolated values have to be considered merely as estimations as the recombination rate generally changes with temperature. The sum of both injection barriers is the difference between E_g and V_{bi}. This sum can be separated into the contribution of each injection barrier if two independent V_{oc} slopes are detected.

Thus, for the bisPC$_{61}$BM blend, a total injection barrier of 0.11 eV is yielded with two contributions of 53 meV and 56 meV. The Ca/Al contacted PC$_{61}$BM device reveals only one detectable injection barrier of 0.16 eV. The same device with a Cr/Al electrode shows a drastically lower slope of V_{oc}. This suggests that the critical injection barrier already exceeded one of the built-in injection barriers. Compared to the Ca/Al contacted device, this implies a high injection barrier of at least 0.29 eV as well as a second barrier of not more than 0.05 eV. The results are comparable to findings in literature [114].

In many V_{oc} vs. temperature measurements, a decrease of V_{oc} is observed at very low temperatures [109]. This is attributed to an electric field dependent charge carrier generation process. If the thermal potential at low temperatures is not sufficient to split-up polaron pairs, the charge carrier density is reduced and V_{oc} is decreased. This effect was shown by temperature dependent charge extraction measurements and is visible in the simulation as well [109]. An equivalent determination of V_{bi} and E_g is possible for PHJ devices.

5.7. Conclusion

For organic photovoltaics the question whether a bulk or a planar heterojunction solar cell is advantageous for an optimized device in terms of V_{oc} has as yet not been answered. Experimental and theoretical results regarding both device types show a fundamental difference. The well separated layers of a PHJ device allow a good separation and a low recombination of charge carriers. In a BHJ solar cell, more charge carriers are accumulated, however, with an increased recombination probability. Consequently, BHJ solar cells yield higher V_{oc} values especially for low light conditions. The PHJ solar cell is less influenced by injection barriers. Combined with the generally lower recombination rate, this leads to a higher V_{oc} at high illumination conditions. In contrast to literature [97], it was shown that also the V_{oc} of PHJ solar cells is a function of the injection barriers.

Critical injection barriers were found to limit the open circuit voltage of both device types. Due to charge carrier injection at the electrodes, charges diffuse into the solar cell and create a repulsive electric field. This electric field, the band bending, represents an intrinsic loss mechanism which limits V_{oc} for small injection barriers. It mainly depends on the optical generation and bulk recombination of charge carriers. For small injection barriers, this leads to an injection barrier independent, maximum V_{oc} which is significantly smaller than E_g. These losses likely correspond to the empirically defined constant factor between 0.3 V and 0.5 V which is known from literature [99]. At higher injection barriers, V_{oc} is additionally influenced by injection barriers as well as by surface recombination. The optically generated charge carrier density exceeds the injected charge carrier density at the electrodes and V_{oc} is linearly decreased with the injection barrier.

The found correlation of V_{oc} allows the interpretation of temperature and illumination dependent measurements in order to determine the effective band gap, the injection barriers as well as the built-in potential.

The presented results have been published in Refs. [109] and [108].

6. S-shaped current–voltage characteristics of bulk heterojunction solar cells

A detailed analysis of the open circuit voltage of organic solar cells was presented in the previous chapter. The intention was that the performance of the solar cell can be improved by finding an optimization strategy for V_{oc}. Optimizing V_{oc} in terms of the injection barriers and maximizing the charge carrier densities, however, does not necessarily lead to enhanced power conversion efficiencies.

Experiments with innovative organic semiconductors, but also well-known systems, sometimes show an S-shaped deformation of the device current–voltage characteristic. Instead of an exponential current–voltage ratio as expected for diode structures, the response of such a device in forward direction shows a local saturation and a later again increasing current around at a certain applied voltage region. This leads to a reduction of the fill factor and of the power conversion efficiency even though V_{oc} and J_{sc} are not necessarily affected. A similar behavior was reported for inorganic copper indium gallium diselenide (CIGS) based devices. Here, the effect was attributed to the influence of a chargeable cadmium sulfide buffer layer which creates an illumination dependent energetic barrier [115]. In organic multilayer solar cells this deformation was observed several times in literature and was attributed to surface dipoles [116–118].

For numeric simulations, a careful description of device interfaces should therefore lead to a double diode characteristic. In most publications, metal–organic interfaces are described by a Schottky contact. The boundary condition for the charge carrier densities therefore is defined by the thermionic emission theory which results in fixed charge carrier densities at the interfaces [33, 60, 119]. Restrictions in the ability to transfer charges from one side of a junction to the other can be expressed by the surface recombination rate [81]. For the latter, models such as mirror charge effects at metal–organic interfaces can be described, resulting in surface charge carrier densities different from those predicted by the thermionic emission theory [82]. For organic solar cells, the importance of low surface recombination rates on the power conversion efficiency has already been discussed, mainly for minority charges [120, 121].

In addition to these boundary conditions at the interfaces, various models for physical effects inside the active layers of solar cells are available for numerical simulations. Optical interference calculations are applied to determine the spatial charge carrier generation by absorbed light [95, 122]. If the existence of charge transfer states during the generation process is expected, an electric field dependent separation can be calculated based on the assumption of Gaussian distributed exciton binding distances [60]. Charge transport models for the mobility of electrons and holes are deduced by Monte Carlo simulation techniques [14, 36, 123]. Combinations of these models are often used to compare and evaluate experimental data [124, 125]. Nevertheless none of these models is able to predict S-shaped current–voltage characteristics in simple device geometries as discussed here.

To combat the matter above, an experiment was developed in order to create organic bulk heterojunction solar cells which reproducibly show S-shaped current–voltage characteristics. The experiment is based on an extended oxygen plasma etching of the indium tin oxide (ITO) anode. The S-shape was qualitatively reproduced by assuming reduced surface recombination velocities in the simulation.

6.1. Experimental methods

In order to measure S-shaped current–voltage characteristics, bulk heterojunction solar cells were assembled on structured ITO coated glass. The glass was successively cleaned for 10 minutes each in water, acetone and isopropanol in an ultrasonic bath. The anode was subsequently exposed to an oxygen plasma etching which contained low amounts of moisture for various time scales to change the ITO work function [126]. Hydroxide anions and more complex chemical groups are able to bind to open dangling bonds of the ITO surface during this process [127, 128]. On this substrate, an optional layer of poly (3,4-ethylenedioxythiophene) poly(styrenesulfonate) (PEDOT:PSS) was spincoated and transferred into a nitrogen atmosphere before annealing the PEDOT:PSS for 10 minutes at 130 °C. The active layer consisting of poly (3-hexyl thiophene) (P3HT) as donor and [6,6]-phenyl-C61 butyric acid methyl ester (PCBM) as acceptor was spin coated from a chlorobenzene solution (ratio 1:0.7). Finally, a second annealing step at 130 °C for 10 minutes and the evaporation of the metal

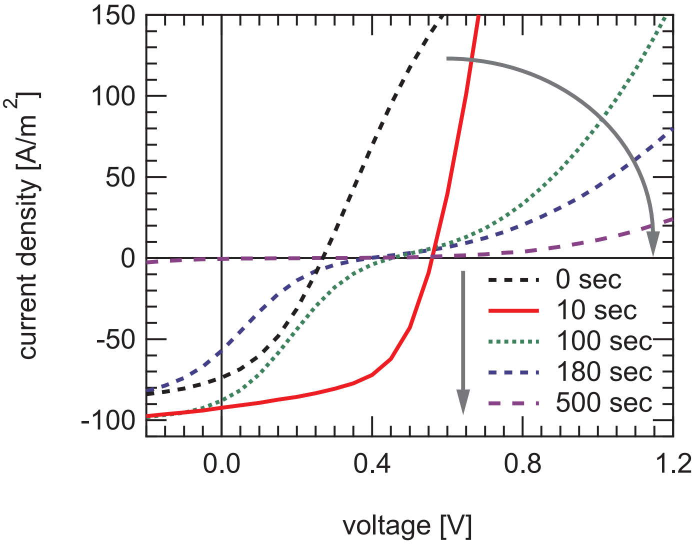

Figure 6.1.: Measured current–voltage characteristics of illuminated bulk heterojunction solar cells without PEDOT:PSS layer. The solar cell with a 10 second oxygen plasma treatment of the ITO substrate shows a regular current–voltage behavior. Extended treatment durations lead to an S-shape which reduces the solar cell efficiency.

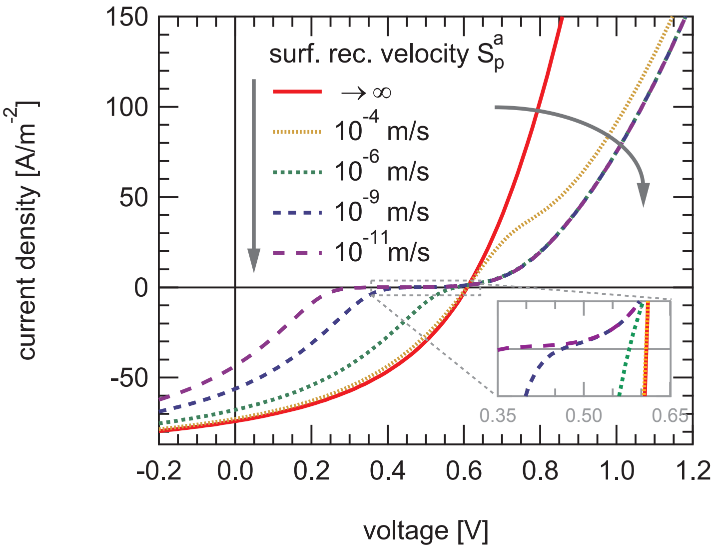

Figure 6.2.: Simulated S-shaped current–voltage characteristics caused by a reduced majority surface recombination velocity S_p^a for holes at the hole conducting anode. With decreasing velocity, the S-shape becomes more distinctive and limits the power conversion efficiency by diminishing open circuit voltage, fill factor and short circuit current. A magnification of the V_{oc} dependence on the decreasing surface recombination velocity is shown in the bottom right corner.

Ca/Al cathode completed the solar cell assembly. The materials were purchased from H.C. Starck (PEDOT:PSS), Rieke Metals (P3HT) and Solenne (PCBM).

The current–voltage characteristics were recorded by a Keithley 237 source measurement unit under an artificial AM1.5 sun spectrum with a spectral radiance of 100 mW/cm^2. This illumination was simulated by a 300 W xenon lamp adjusted by a mismatch factor. Layer thicknesses and the ITO roughness were determined by a Veeco Dektak 150 profilometer. The devices were assembled and measured by M. Binder and D. Rauh [129, 130].

A typical result is shown in Fig. 6.1 (a) for an illuminated BHJ solar cell without a PEDOT:PSS layer. Within the first ten seconds of plasma etching, the power conversion efficiency increased from 0.72 to 2.9 %. The open circuit voltage is enhanced from 270 to 560 mV, the fill factor from 0.36 to 0.56 and the short circuit current from 7.37 to 9.23 mA/cm^2.

After 500 seconds of oxygen plasma treatment, the samples undergo an efficiency loss to 0.0017 %. This can be attributed to the drastic drop in short circuit current to 0.047 mA/cm^2. The open circuit voltage decreases to 235 mV, the fill factor to 0.15. The measured roughness of the ITO substrate was not changed during the oxygen plasma etching within the profilometer noise level of 5 nm. The conductance of the ITO substrate remained unchanged. The active layer thickness of all measured samples was about 230 nm.

Deposing a PEDOT:PSS layer on top of the treated ITO anode slightly improves the initial solar cell working efficiency. In contrast to a cell without PEDOT:PSS, the first ten seconds of oxygen plasma etching do not improve this value. Longer treatment durations result in an equivalent S-shaped current–voltage characteristic but with a constant V_{oc} level (not shown).

Due to the distinct treatment of the ITO anode, we focus on the properties of this metal–semiconductor interface to find the origin of the S-shaped deformation. In order to represent

parameter	symbol	value	unit
effective band gap	E_g	1.10	eV
charge carrier mobilities	μ_n, μ_p	$1.0 \cdot 10^{-8}$	m^2/Vs
active layer thickness	L	100	nm
generation rate	G	$6.0 \cdot 10^{27}$	1/m^3s
temperature	T	300	K
relative dielectric permittivity	ε_r	3.4	
effective density of states	N_c, N_v	$1.0 \cdot 10^{27}$	1/m^3
injection barriers:			
- cathode	Φ_n	0.0	eV
- anode	Φ_p	0.1	eV
surface recombination velocities:			
- minority (holes), cathode	S_p^c	$\to \infty$	m/s
- minority (electrons), anode	S_n^a	$\to \infty$	m/s
- majority (electrons), cathode	S_n^c	$\to \infty$	m/s
- majority (holes), anode	S_p^a	$1.0 \cdot 10^{-9}$	m/s

Table 6.1.: Parameter set for simulating S-shaped current–voltage characteristics shown in Fig. 6.2. References for the effective band gap, the mobilities and the relative dielectric permittivity are given in [106], [111], [55] and [131]. Infinite surface recombination velocities are set to a numeric value of 10^{50}m/s.

metal–semiconductor charge transfer processes in a general way, we use the surface recombination rate for electrons and holes according to Eqns. (3.33) and (3.34). Since these equations do not exclusively describe recombination, but also an extraction of charge carriers out of the semiconductor, it also can be considered as an extraction rate. In contrast to the thermionic emission theory, the amount of surface charges n is changed by the surface recombination velocity S, which defines the current transferred across the metal–semiconductor interface. As we consider an active material between two metallic electrodes, we assume four independent surface recombination velocities $S_{n,p}^{a,c}$, for electrons and holes at each electrode, as listed in Tab. 6.1.

A series of qualitative simulations were performed based on the parameter set listed in Tab. 6.1. We assumed a pure bimolecular Langevin recombination and constant charge carrier generation throughout the device. By limiting the majority charge carrier surface recombination velocities at the ITO contact (holes) from infinity (10^{50} m/s) stepwise down to 10^{-11} m/s, an equivalent S-shape was yielded. The results are shown in Fig. 6.2. Similar to the case without a PEDOT:PSS layer, the open circuit voltage was reduced from 609 to 360 mV in the simulation. The corresponding short circuit currents were diminished from 74.1 to 43.4 A/m^2, the fill factor from 0.41 to 0.18. Constant V_{oc} values were retrieved if the minority (electron) surface recombination velocity at the anode was limited as well.

6.2. Origin of the S-shaped deformation

Metal–organic junctions possess an intrinsic charge carrier density described by the injection barrier according to the thermionic emission theory (Eqns. (3.12) - (3.15)). No prediction on the amount of conducted charge is made with this parameter. If there are restrictions on the charge extraction process, this needs to be expressed by the surface recombination velocities (Eqns. (3.33), (3.34)). If a constant current that has to be transported through the interface is assumed, a reduction of the surface recombination velocity S has to be compensated by additional charges at the junction ($n - n_{th}$) in order to maintain the passed current. These piled-up charges therefore create an applied voltage dependent space charge region which modifies the energetic band structure of the device. The effect of constant majority surface recombination velocities at the anode creating a typical S-shaped current–voltage curve is shown in Fig. 6.2.

It is known from literature for planar semiconductor heterojunctions to cause equivalent S-shaped characteristics. The physical origin of this effect is depicted in the upper row of Fig. 6.3. The heterojunction is defined (I a) by the energy differences between the two LUMO (ΔE_{LUMO}) and the two HOMO energies (ΔE_{HOMO}) of both semiconductors directly at the interface. Driven by an electric field (I b), additional electrons above the intrinsic neutrality level can cross such an interface without a transport problem if they are transferred from the energetically unfavorable level to a more favorable one. However, a local potential well is created if the polarity of the applied voltage is changed (I c). This leads to the generation of a local space charge and creates an S-shaped current–voltage characteristic [117, 118, 132]. The same effect was observed in copper indium gallium diselenide (CIGS) devices where such S-shape behavior was attributed to by light filled traps in an intermediate cadmium sulfide layer which creates an illumination dependent energetic barrier [115]. In addition to the energy levels, any abrupt parameter change between two semiconductor layers, which results in a direction dependent current transport, is potentially able to create such an S-shape.

In device geometries such as bulk heterojunctions, without planar semiconductor heterojunction, this approach cannot be applied. Due to the constant metallic work function, metals are not able to create potential wells as shown in Fig. 6.3 (II). The injection barrier Φ_n (II a) defines the intrinsic charge carrier density at the interface by the Boltzmann equation (Eqn. (3.12)). Hence, creating a local space charge needs the definition of an additional parameter, the surface recombination velocity. If, under extraction conditions (II b) charges are transported faster towards the interface than they can be extracted, those charges will pile up and create a space charge which depends on the applied electric field. Under injection conditions (II c), the injection of charge carriers is reduced if the surface recombination velocity is assumed to be constant. A local depletion zone is created. The injection barrier at metal–organic interfaces is not able to create S-shapes on its own.

As depicted in Fig. 6.3 for electrons, this issue is true for holes as well. For moderately reduced values of $S_p^a = 10^{-4}$ m/s (Fig. 6.2), an S-shaped current–voltage characteristic is created at higher (positive) voltages. It does not significantly influence the solar cell efficiency parameters V_{oc}, J_{sc} or the fill factor. With a further decreased surface recombination velocity, the deformation approaches V_{oc} and creates a horizontal plateau of constant current density. Hence, all mentioned solar cell parameters are reduced.

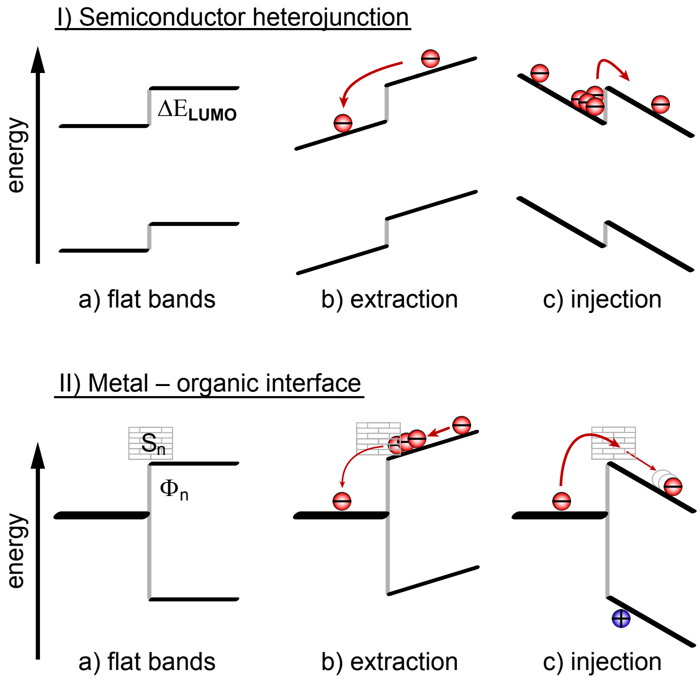

Figure 6.3.: Space charge accumulation in semiconductor devices. (Upper row, a) At a semiconductor heterojunction the two LUMO energy levels possess a work function difference of ΔE_{LUMO} at the interface. (b) Excess electrons cross this interface from an energetically unfavorable state to the more favorable one without restrictions. (c) If electrons are forced to overcome this energetic barrier in the opposite direction, a local potential well is established and electrons are piled up at the heterojunction. (Lower row, a) At a metal–organic interface the work function difference between the metal Fermi level and the semiconductor LUMO level Φ_n defines the intrinsic electron concentration at the interface. Due to the constant metal work function no potential well or space charge can be created. (b) By a finite surface recombination velocity S_n electron transport through the interface is limited. Electrons which are transported faster towards the interface than they are removed create a space charge. (c) The amount of injected charge carriers is reduced by finite surface recombination velocities which creates a local charge carrier depletion zone at the interface.

6.3. Energetic structure

The deformation of the current–voltage characteristics originates from the internal energetic band structure and charge carrier distributions of electrons and holes. Fig. 6.4 shows the device band structure under applied voltages of (a) $V_a = 300$ mV and (b) $V_a = 900$ mV, hence under extracting and injecting conditions, respectively. The energy levels of the LUMO and HOMO bands (E_{LUMO}, E_{HOMO}) are indicated by the thick solid lines, those of the quasi-Fermi levels E_{Fn}, E_{Fp} by the blue and red dashed lines. At the anode (left contact) a limiting surface recombination velocity of $S_p^a = 10^{-9}$ m/s is assumed. For comparison, the underlying gray lines show the same solar cell without such a limitation and therefore without an S-shaped deformation.

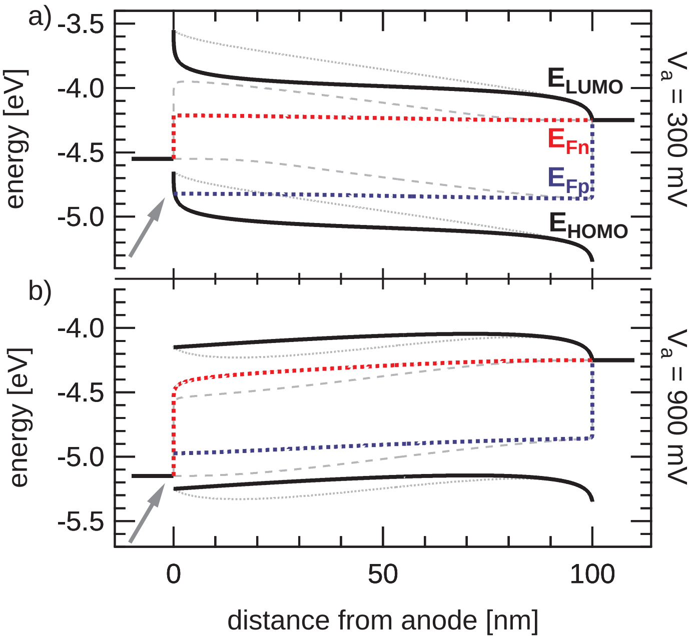

Figure 6.4.: Energy structure of a solar cell with the energetic levels of HOMO and LUMO (solid and dotted lines) as well as their corresponding quasi-Fermi levels E_{Fn} and E_{Fp} (dashed red and blue lines) under illumination. The thick lines indicate the structure under a surface recombination velocity of $S_p^a = 10^{-9}$ m/s. Thin lines correspond to perfectly conducing contacts ($S_p^a \to \infty$). In the case of hole injection by the anode (compare to Fig. 6.3 (II b)) at an applied voltage of 300 mV the quasi-Fermi level of holes split up at the anode. This generates a space charge combined with a significantly higher electric field close to the anode. Holes are injected into the bulk at a voltage of 900 mV by the anode (Fig. 6.3 (II c)). Due to the surface recombination, less majority charges are present at the interface and a hole depletion zone is created which decreases the local electric field. The cathode work function (right side) was set to a fixed value of -4.25 eV.

Within the solar cell working regime, charge carriers generated by light are extracted from the active layer into the metal electrodes. A reduced majority surface recombination velocity S_p^a limits an efficient holes extraction by the anode and holes are piled up at the interface (Fig. 6.4 (a)). Consequently, the quasi-Fermi level of holes is shifted towards its HOMO level at the anode interface which creates a quasi-Fermi level discontinuity between E_{Fp} and the anode work function. The interface hole density is higher than predicted by the thermionic emission theory. In addition to the already high hole concentration at the anode interface for infinite surface recombination velocities, additional majority charges will be added creating a space charge. Due to Coulombic interaction, these charges increase the local electric field at the contact and consequently reduce the potential drop inside the bulk of the semiconductor [133]. In a solar cell dominated by drift, charges are transported more slowly through the device, thus, increasing the probability of recombination.

At voltages above the built-in voltage V_{bi}, additional charges are injected into the semiconductor by the metal contacts (Fig. 6.4 (b)). A finite majority surface recombination velocity therefore will reduce the number of injected holes at the anode interface. Thus, the quasi-Fermi level for holes E_{Fp} at the interface is shifted away from E_{HOMO}. Within the interface region, fewer holes and more electrons are available (due to the limited bulk recombination rate). Consequently, the electric field at the interface is reduced and — as in case of Fig. 6.4 (b) — is even able to change signs. The transition between both cases creates an S-shaped kink in the current–voltage characteristics of organic solar cells and leads to a space charge limited current at higher voltages.

6.4. Influence on the open circuit voltage

With decreasing surface recombination velocity, the open circuit voltage drops according to Fig. 6.2. The band diagrams for (a) infinite and (b) finite ($S_p^a = 10^{-9}$ m/s) surface recombination velocities with their corresponding open circuit voltages of 0.61 V and 0.47 V are shown in Fig. 6.5. As in the case of charge carrier extraction the electric field at the anode is enhanced. Nevertheless, the quasi-Fermi level distributions change only slightly except for their split-up directly at the anode contact.

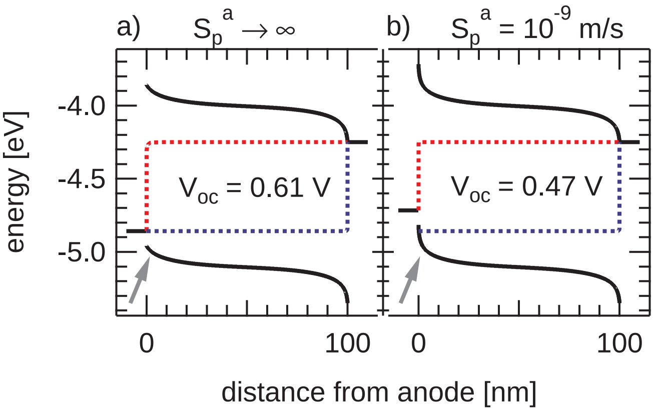

Figure 6.5.: Device band diagram at V_{oc} for surface recombination rates of (a) infinity and (b) $S_p^a = 10^{-9}$ m/s. Due to the condition of zero net current ($\vec{J} = \vec{j}_n + \vec{j}_p = 0$), holes pile up at the anode creating a space charge which reduces V_{oc}. The quasi-Fermi level distribution changes only slightly, but splits up directly at the anode. The band bending close to the anode is increased.

The total current at every location inside the device must be zero under open circuit conditions. Accordingly, the internal current densities for electrons and holes are equal and of different sign, $\vec{J}(x) = \vec{j}_n(x) + \vec{j}_p(x) = 0$. Since an unlimited (infinite) minority surface recombination always creates a steady diffusive recombination current towards the anode, this current has to be neutralized by an equivalent majority surface recombination current. If the surface recombination velocity according to Eqn. (3.33) is reduced, the condition of zero net current can only be fulfilled by an accumulation of majority charges at the surface. The space charge leads to an S-shaped current–voltage characteristic and reduces V_{oc} (Fig. 6.5). This is schematically summarized in Fig. 6.6.

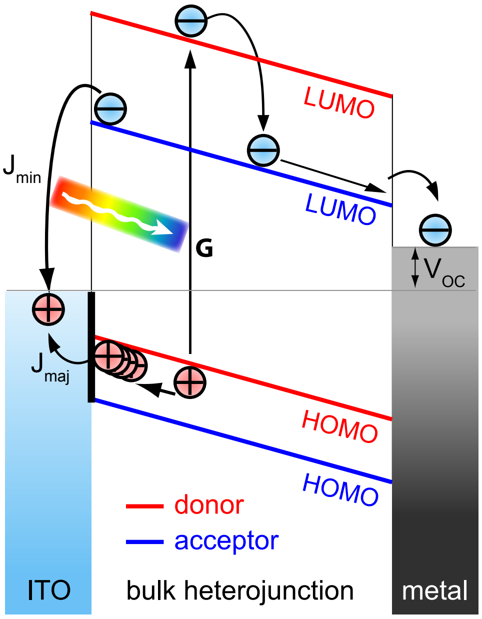

Figure 6.6.: Charge carrier dynamics in a BHJ device showing an S-shaped IV-characteristic. Excitons generated by light are separated and the charge carriers are transported towards the electrodes. Due to a reduced hole recombination velocity at the anode, holes pile up until the transferred current into the anode J_{maj} equals the amount of electrons which diffuse into the same contact J_{min}. V_{oc} is reduced due to the local space charge.

If minority and majority surface recombination velocities are simultaneously limited for the same contact, minority charge carriers are hindered to diffuse into the contact as well. The S-shape is still observable due to the charge carrier transport problems. However, V_{oc} is not reduced since the space charge is not required at V_{oc} conditions. This effect corresponds to the application of an electron blocking layer (PEDOT:PSS) on the ITO anode and is in agreement with the experimental results.

Two different V_{oc} regimes can be distinguished if the calculated V_{oc} is plotted against the limited majority (hole) surface recombination velocity at the anode. This is depicted in Fig. 6.7. The electron surface recombination velocity was set to infinity. V_{oc} remains constant at high majority surface recombination velocities whereas V_{oc} decreases logarithmically at lower values.

The open circuit voltage has already been separated into its components in Chap. 5. It was defined by the effective band gap E_g, the injection barriers Φ_n, Φ_p and the energy loss by the internal electric field E_{loss},

$$qV_{oc} = E_g - \Phi_n - \Phi_p - E_{loss}. \tag{6.1}$$

In analogy to Eqn. (5.8), the energy loss in proximity to the anode can be separated and approximated by

$$E_{loss} = \frac{k_B T}{q} \Big[\ln(p) \Big]_0^{x_{int}}. \tag{6.2}$$

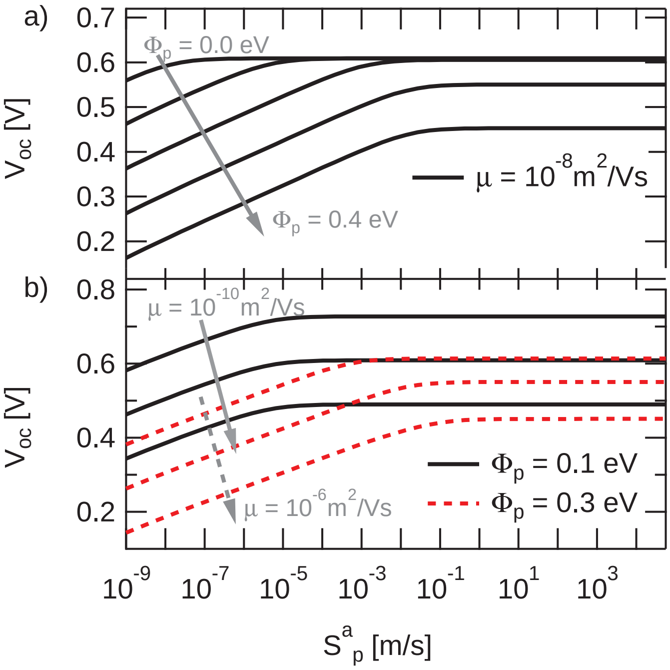

Figure 6.7.: Open circuit potential plotted versus the hole surface recombination velocity at the anode. Under the assumption of balanced charge carrier mobilities ($\mu_n = \mu_p$), (a) shows a variation of the anode injection barrier from 0.0 to 0.4 eV in steps of 0.1eV whereas (b) presents the same solar cell with constant injection barriers and charge carrier mobilities of 10^{-10} m^2/Vs, 10^{-8} m^2/Vs and 10^{-6} m^2/Vs. At high surface recombination velocities, no dependence of V_{oc} on the surface recombination velocity is observed. A reduction below a critical point results in a linear decrease of V_{oc} on the semi logarithmic scale. This is attributed to a logarithmic dependence of the local electric field at the contact on the majority charge carrier density.

The anode is located at $x = 0$. E_{loss} can be separated since the charge carrier density at the anode is the sum of thermally activated charge carriers (p_{th}) and accumulated charge carriers due to the reduced surface recombination ($p_{th} - p$),

$$E_{loss} = \frac{k_B T}{q} \left\{ \ln(p(x_{int})) - \left[\ln(p_{th}) + \ln\left(1 + \frac{p(0) - p_{th}}{p_{th}}\right)\right]\right\}. \tag{6.3}$$

In the squared bracket, the left summand represents the electric field in the solar cell (at the anode region) for Schottky contact and infinite surface recombination velocities. The effect of accumulated charges due to the limited majority surface recombination velocity is explicitly summarized in the right summand. Therefore, Eqn. (6.1) can be extended using the electrical field of a solar cell without limiting contacts $F_{(s \to \infty)}(x)$ and the separate influence of the majority surface recombination velocity at the anode. Since no additional holes are accumulated at the cathode, we retrieve

$$qV_{oc} = E_g - \Phi_n - \Phi_p - E_{loss\,(s\to\infty)} - \frac{k_B T}{q} \ln\left(1 + \frac{J_s}{qS_p^a p_{th}}\right). \tag{6.4}$$

The anode hole recombination velocity S_p^a, the number of thermally activated holes at the anode p_{th} and the minority surface recombination current J_s are required. Reduced minority surface recombination limits J_s and therefore prevents a decrease of V_{oc}.

Within the derived formalism of critical injection barriers Φ_c (Eqn. (5.17)) in Chapter 5, finite surface recombination velocities are easily incorporated. Since a local space charge effectively changes the band bending in the device, the critical injection barrier is modified to

$$\Phi_c^{anode} = -\frac{k_B T}{q} \ln\left(\frac{\sqrt{\frac{G}{k_F} - n_i^2} - \frac{J_s}{qS_p^a}}{N_v}\right). \tag{6.5}$$

The amount of effectively accumulated charge carriers due to the limited surface recombination velocity p_s is given by

$$p_s = \frac{J_s}{qS_p^a} N_v. \tag{6.6}$$

For high surface recombination velocities S_p^a, no significant space charge is generated at the contact. The amount of accumulated charges is small compared to the optically generated charge carrier densities. This corresponds to the horizontal plateaus in Fig. 6.7. As soon as p_s approaches the optical generated charge carrier density, the critical injection barrier increases logarithmically with the majority surface recombination velocity. Hence, V_{oc} is correspondingly reduced (Fig. 6.7).

6.5. Space charge limited current

In order to extract information on the type of charge transport, it is appropriate to set V_{oc} as the origin of the voltage axis. Subtracting V_{oc} as seen in the lower right section of Fig. 6.2 from the voltage axis and choosing a double logarithmic presentation for the calculated current–voltage curves (Fig. 6.8) reveals an ohmic ($J \propto V$) behavior at low voltages. At higher voltages it asymptotically changes towards a trap free space charge limited current (SCLC),

$$J_{SCLC} = \frac{9}{8}\mu\varepsilon_0\varepsilon_r \frac{V^2}{L^3}. \tag{6.7}$$

This kind of charge transport was intensively studied in the past [9, 134–137], although the origin of S-shaped current–voltage kinks was not described.

An S-shaped deformation created by a finite majority surface recombination velocity connects this behavior to the analytic SCLC prediction. Hence, in context of Fig. 6.8, an S-shape can be interpreted as a direct transition from an ohmic toward a space charge limited current.

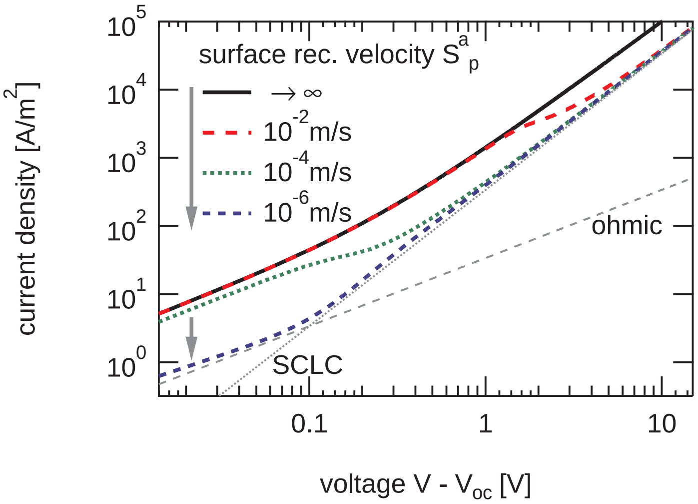

Figure 6.8.: Calculated current–voltage characteristics with V_{oc} set to voltage axis origin. The anode majority surface recombination velocity is reduced from infinity to 10^{-6} m/s. At voltages near V_{oc}, an ohmic transport regime (slope 1) can be found, which changes to a space charge limited current at higher voltages (slope 2). The transition between both transport regimes is indicated by an S-shaped deformation of the calculated characteristics.

6.6. Conclusion

S-shaped current–voltage characteristics are an often observed but not understood problem of BHJ solar cells. In this chapter, BHJ solar cells showing such deformations were reproducibly created by applying moisture containing oxygen plasma etching to the ITO substrate. Charging processes between different semiconductor layers could be excluded due to the absence of planar semiconductor heterojunctions. The S-shaped IV-curves were qualitatively reproduced by numeric simulations under the assumption of finite surface recombination velocities of holes at the anode.

By analyzing the calculated energetic band structure, we assign space charges created by the reduced majority surface recombination velocity as the origin of the characteristic deformation. Since injection barriers also change the charge carrier densities at the contacts, we could see both parameters affecting V_{oc}. However, only the surface recombination velocity which creates a local space charge depending on the transport direction of the charge carriers was able to create an S-shaped current–voltage characteristic. In agreement with observations for PHJ devices this leads to the conclusion that all S-shaped current–voltage characteristics are generated by direction dependent charge transport barriers.

An analytic approximation showed that the loss of V_{oc} caused by decreased majority surface recombination velocities can be countervailed by the reduction of the minority surface recombination velocity. Finally, we were able to show that the S-shape indicates the transit from an ohmic conductivity to a space charge limited current.

The presented results have been published in Ref. [129].

7. Optimization of the power conversion efficiency

A strong focus on gaining higher power conversion efficiencies can be observed in recent research on organic solar cells [8]. Since the first organic solar cells which converted far less than one percent of the incident light into electric power, state-of-the-art compounds are already able to yield above 10 % power conversion efficiency [138, 139]. Theoretically predicted by the Shockley–Queisser limit, efficiencies up to 33 % should be possible [10, 140]. However, it is not obvious how to design an optimal organic solar cell in order to extend the already achieved values.

In the previous discussions we have seen that the charge carrier densities and the injection barriers influence V_{oc}. However, an efficient charge transport which is necessary to obtain high photocurrents was not considered. The strong impact of the charge carrier mobilities is known from experiments. Higher mobilities facilitate fast charge extraction, but also increase charge carrier recombination. Electric field dependent charge carrier generation processes relate the optical generation of charge carriers to the electric field distribution in organic solar cells. In order to build an optimized solar cell, these interacting processes must be optimized.

The influence of the charge carrier mobility on the device performance is investigated in this chapter by extending previously published insights [141]. Therefore, the yields of the mobility dependent Langevin recombination as well as a field dependent charge carrier generation are analyzed. The dependences of V_{oc}, FF and J_{sc} on the charge carrier mobility are analyzed and a discussion on how to optimize the power conversion efficiency is made. Subsequently, experimentally found limitations of the Langevin recombination as well as the influence of finite surface recombination velocities are discussed.

7.1. Experimental

Two sets of current–voltage characteristics of BHJ solar cells were calculated in order to examine the maximum power conversion efficiency as a function of the charge carrier mobilities. The generation rate G was set to be constant, independent on the spatial position. The Langevin theory was used to account for nongeminate recombination processes,

$$R = \zeta\gamma\left(np - n_i^2\right). \tag{7.1}$$

This definition includes a experimentally observed reduction ζ of the Langevin recombination, which is explained in detail in Chaps. 3 and 8 [68, 142].

In parameter set A, an electric field dependent polaron pair separation was considered in terms of the Onsager–Braun theory. The net generation rate $U = PG - (1-P)R$ was

parameter	symbol	set A	set B	unit
temperature	T	300	300	K
layer thickness	L	115	100	nm
effective band gap	E_g	1.35	1.05	eV
relative dielectric permittivity	ε_r	3.4	4.0	
effective density of states	N_c, N_v	$1.0 \cdot 10^{27}$	$1.0 \cdot 10^{26}$	$1/\mathrm{m}^3$
generation rate	G	$4.15 \cdot 10^{27}$	$9.0 \cdot 10^{27}$	$1/\mathrm{m}^3\mathrm{s}$
injection barriers	Φ_n, Φ_p	(varied)	0.1	eV
Langevin				
-reduction factor	ζ	1 or 0.01	0.1	
Onsager–Braun				
-binding distance	a	1.3	—	nm
-decay rate	k_f	$1 \cdot 10^4$	—	s^{-1}

Table 7.1.: Parameters used for the efficiency simulations. Both parameter sets are based on P3HT:PC$_{61}$BM solar cells with a 1:1 weight ratio. Whereas the parameter set A represents a slightly thicker solar cell with a field dependent polaron pair separation, parameter set B assumes an electric field independent charge carrier.

consequently used to quantify the influence of the recombination by defining the

$$\text{recombination yield} = 1 - \frac{U}{PG}. \tag{7.2}$$

Note, that this definition is not unproblematic as the net generation rate G includes photogeneration but not the injection of excess charge carriers by an applied voltage. The recombination R however includes both. Hence, the recombination yield is normalized to the rate of purely photogenerated polarons PG.

The Langevin theory predicts a recombination rate which is directly proportional to the charge carrier mobility,

$$\gamma = \frac{q}{\varepsilon_0 \varepsilon_r}(\mu_n + \mu_p). \tag{7.3}$$

However, this relation is proven to be only valid for low-mobility semiconductors with mobilities smaller than approximately 10^{-4} m^2/Vs [9]. Yet, in comparable high-mobility inorganic compound semiconductors such as Cu(In,Ga)Se$_2$, charge carrier mobility independent recombination rates were observed [143]. A general overview of the underlying processes can be found in Ref. [144]. Thus, for parameter set B, the transition between a low and a high mobility regime in terms of recombination was assumed, separated at a critical mobility μ_{crit}. This defines the capped Langevin recombination prefactor γ,

$$\gamma = \begin{cases} \dfrac{q}{\varepsilon_0 \varepsilon_r}(\mu_n + \mu_p) & \text{if } \dfrac{\mu_n + \mu_p}{2} \le \mu_{crit} \\[2ex] \dfrac{q}{\varepsilon_0 \varepsilon_r}(2 \cdot \mu_{crit}) & \text{if } \dfrac{\mu_n + \mu_p}{2} > \mu_{crit}. \end{cases} \tag{7.4}$$

Finite surface recombination velocities S were assumed at the electrodes. For the purposes of this chapter, minority S_{min} and majority S_{maj} surface recombination velocities were summarized. Hence, minority and majority surface recombination velocities were symmetrically set for both contacts (i.e. $S_{min}^{anode} = S_{min}^{cathode}$ and $S_{maj}^{anode} = S_{maj}^{cathode}$).

The parameter sets A and B are listed in Tab. 7.1 and represent common values for thermally annealed P3HT:PC$_{61}$BM (ratio 1:1) solar cells. The reference mobilities for electrons and holes were set to 10^{-8} m^2/Vs with a ratio between electrons and holes (μ_n:μ_p) of unity [55]. The latter assumption of balanced electron and hole mobilities was maintained in all simulations.

7.2. Injection barriers and Langevin recombination

The power conversion efficiency of a bulk heterojunction solar cell versus the charge carrier mobility is shown in Fig. 7.1. An electric field dependent polaron pair dissociation according to parameter set A is assumed.

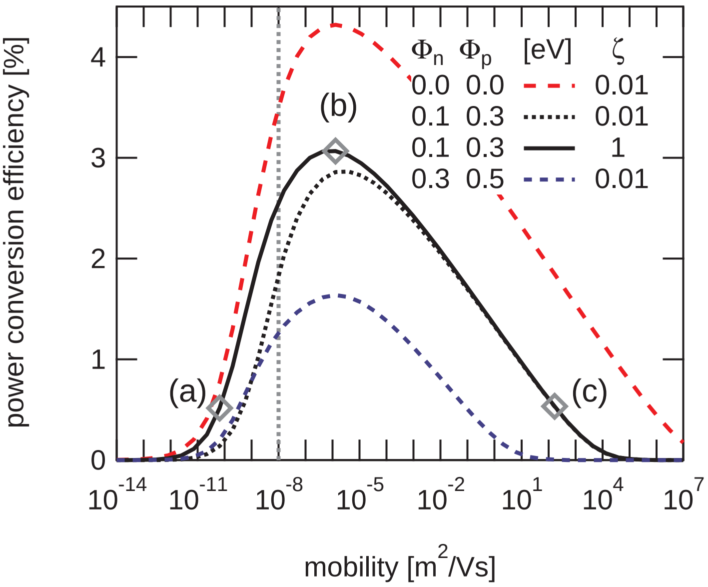

Figure 7.1.: Simulated power conversion efficiencies of BHJ solar cells as a function of the charge carrier mobility for multiple injection barriers at anode (Φ_n) and cathode (Φ_p) as well as recombination prefactors ζ. The simulated P3HT:PC$_{61}$BM device shows an optimal power conversion efficiency at a mobility around 10^{-6} m^2/Vs. The measured reference value of 10^{-8} m^2/Vs is marked by the vertical dotted line. The recombination reduction factor ζ as well as the injection barriers do not change this general trend.

A peak in the power conversion efficiency is observed at a specific mobility of about 10^{-6} m^2/Vs. Its relative position is almost independent of the injection barriers or of reductions of the Langevin recombination ζ. However, the absolute value is reduced by increasing injection barriers. The markers (a), (b) and (c) indicate solar cells with efficiencies of 0.5 %, maximal and again 0.5 % with increasing charge carrier mobilities. Unbalanced charge carrier mobilities are not considered since the lower of both values dominates and limits the power conversion efficiency of the solar cell (not shown).

The corresponding solar cell parameters, V_{oc}, FF and J_{sc} are depicted for two selected injection barrier combinations in Fig. 7.2. Starting from low mobilities with a maximal open circuit voltage, V_{oc} steadily decreases with a more efficient charge carrier transport. Higher charge carrier mobilities facilitate the recombination of charge carriers and V_{oc} is reduced. The photocurrent in contrast shows an inverse behavior with high values for well conducting materials. The resulting power conversion efficiency is an obvious trade-off between the opposing mobility dependencies of V_{oc} and J_{sc}.

The origin of the J_{sc} trends becomes visible by observing the solar cells polaron pair separation yield P as well as the recombination yield according to Eqn. (7.2). Both are shown in Fig. 7.3. Moderate charge carrier mobilities already generate a high polaron pair dissociation yield. An electric field dependent charge carrier generation should therefore not be a limiting factor for the device performance in reasonably efficient solar cells. The inefficient current extraction leads to a charge carrier accumulation at low mobilities. This results in a low J_{sc} and, vice versa, a high V_{oc}. The corresponding band structures and charge carrier density distributions at the maximum power point are illustrated in Fig. 7.4 for the mobilities marked in Fig. 7.1. However, the recombination yield remains high (Fig. 7.3). Consequently the solar cell is limited rather by the charge transport than by charge carrier recombination. At high mobilities the opposite occurs. The efficient charge carrier extraction maximizes J_{sc} but also limits V_{oc} due to a higher recombination and therefore reduced charge

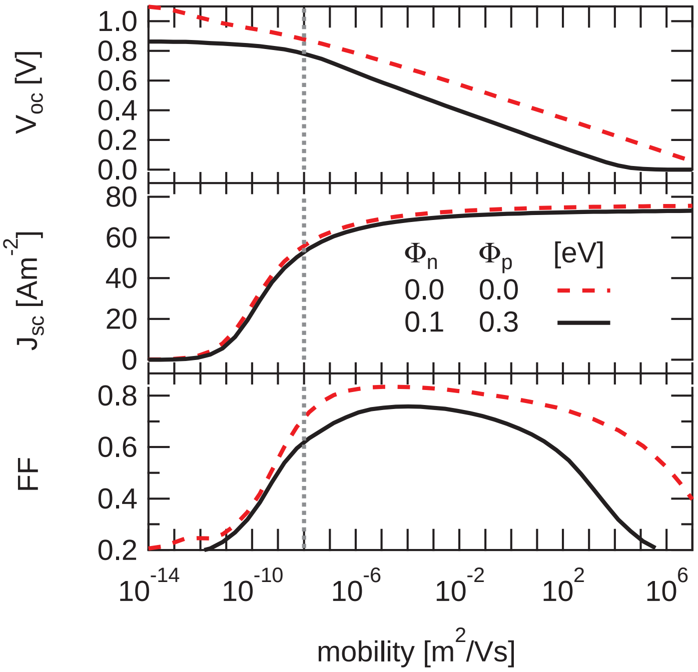

Figure 7.2.: Open circuit voltage, short circuit current and fill factor in dependence on the charge carrier mobility for two selected injection barrier combinations. The open circuit voltage and the short circuit current show an inverse behavior.

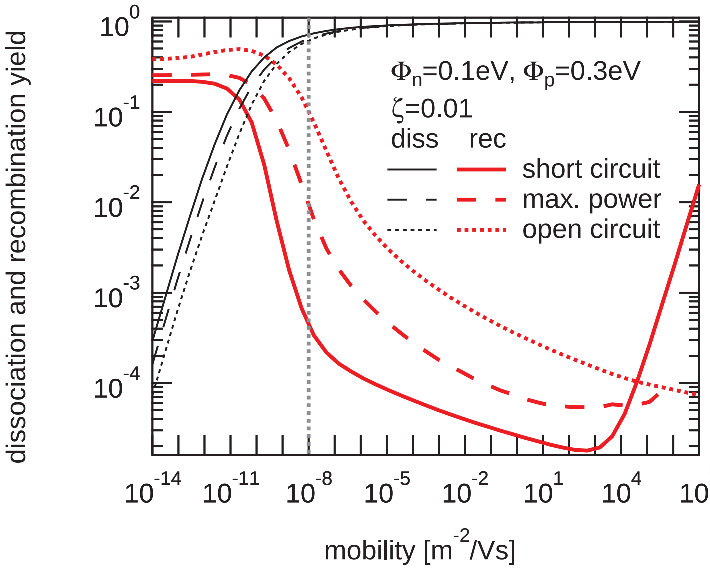

Figure 7.3.: Polaron pair dissociation and polaron recombination yields for injection barriers of 0.1 eV (cathode) and 0.3 eV (anode) in dependence on the charge carrier mobility for short circuit, maximum power point and open circuit conditions. The dissociation yield grows with increasing mobility.

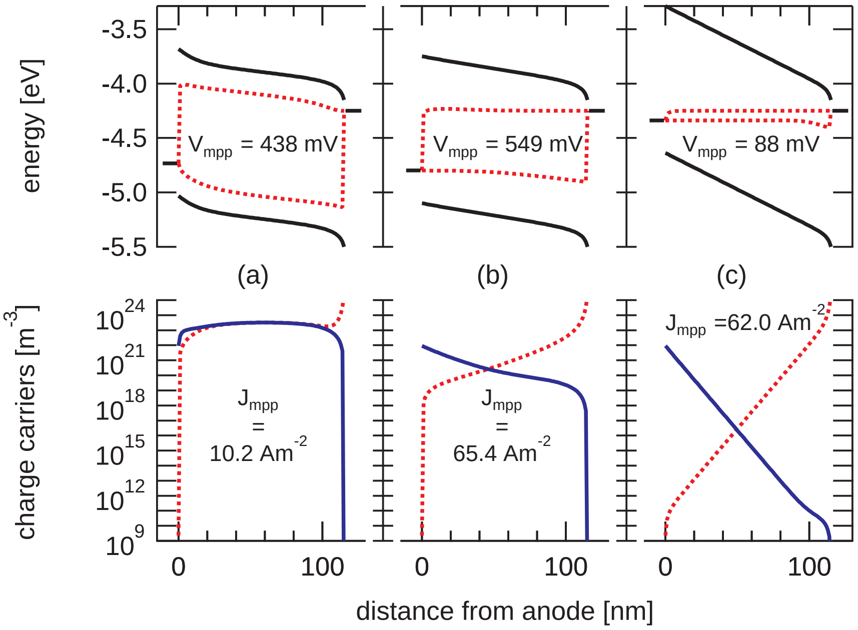

Figure 7.4.: In the upper row the HOMO and LUMO energies (solid lines) and the corresponding quasi-Fermi levels for electrons and holes (dotted lines) are shown for the three in Fig. 7.1 marked maximum power conversion efficiencies. The potential is normalized to an arbitrary cathode work function of -4.3 eV. The electron (solid lines) and hole (dashed lines) charge carrier density concentrations are depicted in the lower row.

carrier densities in the active layer.

The efficiency maximum of an organic solar cell is found at moderate charge carrier mobilities. For the maximum power point a high charging of the device combined with an efficient charge carrier extraction is crucial.

7.3. Limited charge carrier recombination

Limitations of the Langevin recombination as well as finite surface recombination velocities have to be considered for a more detailed picture. Therefore, parameter set B is used which also neglects the vanishing effects of a field dependent polaron pair separation.

The effect of a capped Langevin recombination for three selected surface recombination velocity combinations is shown in Fig. 7.5. The value of $S = 10^{-4}$ m/s is based on the model of Scott and Malliaras which describes mirror charge effects at metal–organic interfaces [82]. The importance of such a reduction especially for minority charges has already been emphasized [129, 145].

In the case of a non-limited Langevin recombination (solid lines), a finite minority surface recombination S_{min} enhances the maximum power conversion efficiency (Fig. 7.5). Whereas V_{oc} is barely improved, J_{sc} is increased by the suppressed surface recombination at the electrodes (Fig. 7.6). Conversely, the *FF* as well as J_{sc} are reduced by a space charge which is accumulated in the device by finite majority surface recombination velocities S_{maj}. However,

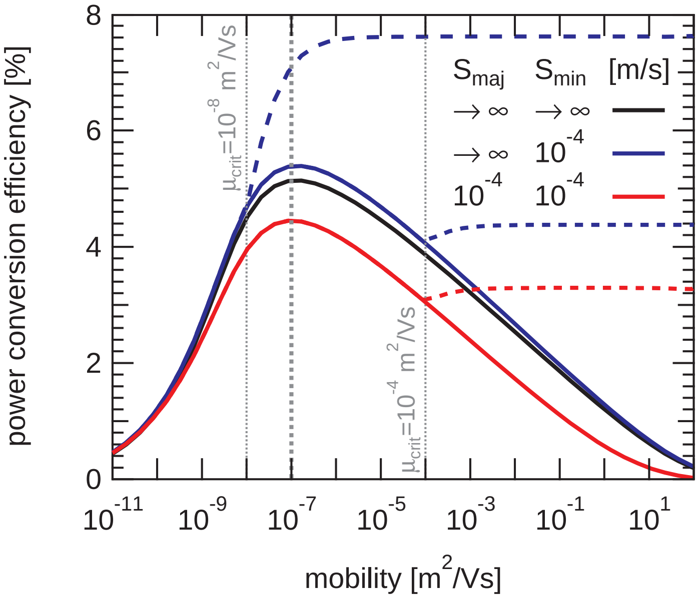

Figure 7.5.: Power conversion efficiency versus balanced charge carrier mobilities of a BHJ solar cell with limited surface recombination velocities (solid lines). Increased power conversion efficiencies are retrieved at higher mobilities for a capped Langevin recombination with critical mobilities of 10^{-8} m^2/Vs and 10^{-4} m^2/Vs (vertical lines). The maximum of the power conversion efficiency profiles of about 10^{-7} m^2/Vs remains unchanged. Not all improved trends (dashed lines) are shown.

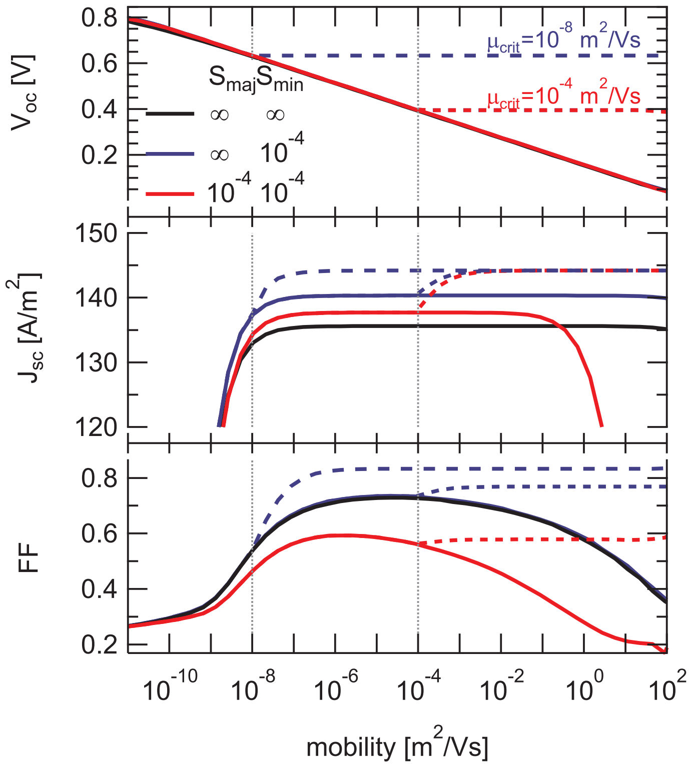

Figure 7.6.: Charge carrier mobility dependence of V_{oc}, J_{sc} and FF corresponding to Fig. 7.5. Slow majority surface recombination velocities limit the charge transport whereas the minority velocities reduce recombination losses at the electrodes. Only combinations which include finite minority surface recombination velocities and a capped Langevin recombination result in a considerable improvement in the power conversion efficiency.

the general trend of an optimal charge carrier mobility of about 10^{-7} m^2/Vs for parameter set B remains maintained.

A capped Langevin recombination rate according to Eqn. (7.4) can be additionally considered. Two independent critical mobilities were set to μ_{crit} of 10^{-4} m^2/Vs (realistic) and 10^{-8} m^2/Vs (reference) [9]. These values correspond to the thin vertical lines in Fig. 7.5 and 7.6. Not all improved trends (one of the red lines) are shown to aid clarity.

The open circuit voltage shows a linear dependence on the logarithmic mobility axis and drops linearly from 0.8 V at low mobilities to zero at higher mobilities. This observation is in accordance with Chap. 5 and represents the decreasing charge carrier density in the device. A capped Langevin recombination prefactor results in a constant V_{oc} above μ_{crit} if the surface recombination (S_{min} = 10^{-4} m/s) is suppressed. However, without a capped Langevin recombination, a passivated surface barely increases the charge carrier density in the device due to the implicitly higher surface recombination.

The capped Langevin recombination rate according to Eqn. (7.4) is limited if the charge carrier mobility exceeds the critical mobility μ_{crit}. An increase of J_{sc} around μ_{crit} is consequently expected. However, this is not observed without a limitation of the minority surface recombination velocity. It implies that charge carriers are well extracted from the solar cell and J_{sc} is consequently not limited by Langevin recombination. Only in the case of a finite minority surface recombination J_{sc} is enhanced at higher charge carrier mobilities. The minority charge carriers saved at the electrodes enhance the charge carrier density. For extraction they have to cross the active layer, which makes them prone to bulk recombination. Consequently J_{sc} is increased at mobilities above μ_{crit}. The formation of S-shaped current–voltage characteristics for finite majority charge carrier velocities combined with higher mobilities also decreases J_{sc} as depicted in Fig. 7.6 (solid red line).

7.4. Impact of surface recombination velocities

In addition to the selected surface recombination velocities in Fig. 7.5, S-shaped current–voltage characteristics suggest the existence of variable surface recombination velocities.

The intersection of Fig. 7.1 at a mobility of 10^{-7} m^2/Vs is shown in Fig. 7.7 for variable surface recombination velocities. The capped Langevin recombination does not change this general trend. The corresponding solar cell parameters V_{oc}, J_{sc} and FF are depicted in Fig. 7.8 for a critical mobility of $\mu_{crit} = 10^{-8}$ m^2/Vs. The band structures for open circuit and short circuit conditions are given in Fig. 7.9 for all marked positions.

The influence of finite minority surface recombination velocities S_{min} is equivalent to a surface passivation by electron and hole blocking layers at the cathode and anode. The charge carrier density rises by preventing charges from recombining at the electrodes and an enhanced V_{oc} is gained. The minority quasi-Fermi levels are not macroscopically connected to the work functions of the electrodes (Fig. 7.9 (b)) compared to the unaffected device (a).

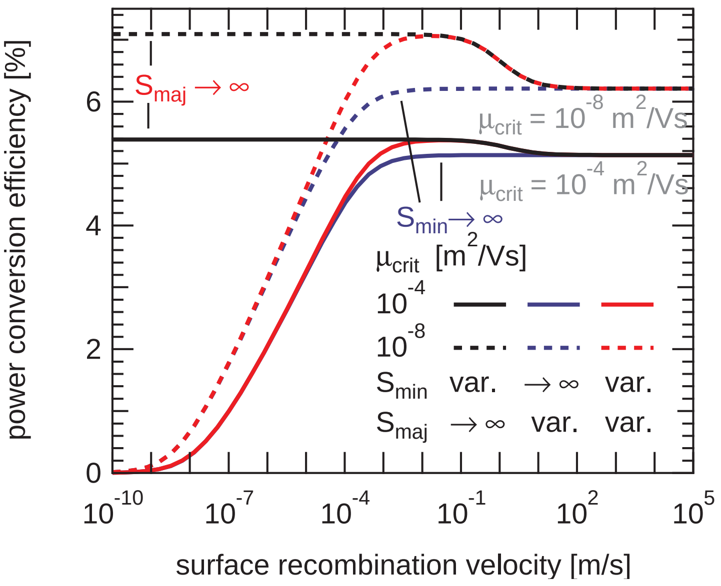

Figure 7.7.: The intersection of Fig. 7.1 at a charge carrier mobility of 10^{-7} m^2/Vs. It shows the influence of limited surface recombination velocities. A decreasing minority surface recombination velocity first improves the solar cell power conversion efficiency. An additional majority surface recombination dominates and reduces the power conversion efficiency at lower velocities.

Reduced majority surface recombination velocities S_{maj} represent a charge carrier transport barrier. As the charge transfer over the metal–organic interfaces is restricted, J_{sc} is reduced as soon as the accumulated charge carriers at the interface generate a repulsive electric field of sufficient size at the electrodes (Fig 7.9 (c)). The implicit larger band bending reduces V_{oc} and causes the fill factor to break down.

If minority and majority surface recombination velocities are simultaneously limited, the passivated surface is able to maintain V_{oc} according to Eqn. (6.4). Minority and majority charge carriers are more evenly distributed throughout the active layer. However, the limited transport of majority charge carriers directly results in a breakdown of J_{sc}. As the trigger levels of both effects differ due to the different amount of transported charges over the interfaces, this offers a possibility for device optimizations.

In a moderate surface recombination velocity regime (e.g. 0.1 m/s), non-perfect electrodes on organic solar cells help to increase the power conversion efficiency due to surface passivation, which increases V_{oc}. As this might not be easily viable in reality, electron and hole blocking layers on both sides of BHJ solar cells should always be considered as they will help to extend the device performance in a similar way. However, if the charge transport properties of metal–organic interfaces are experimentally controllable, problems caused by additional blocking layers as the consumption of internal electric field can be minimized.

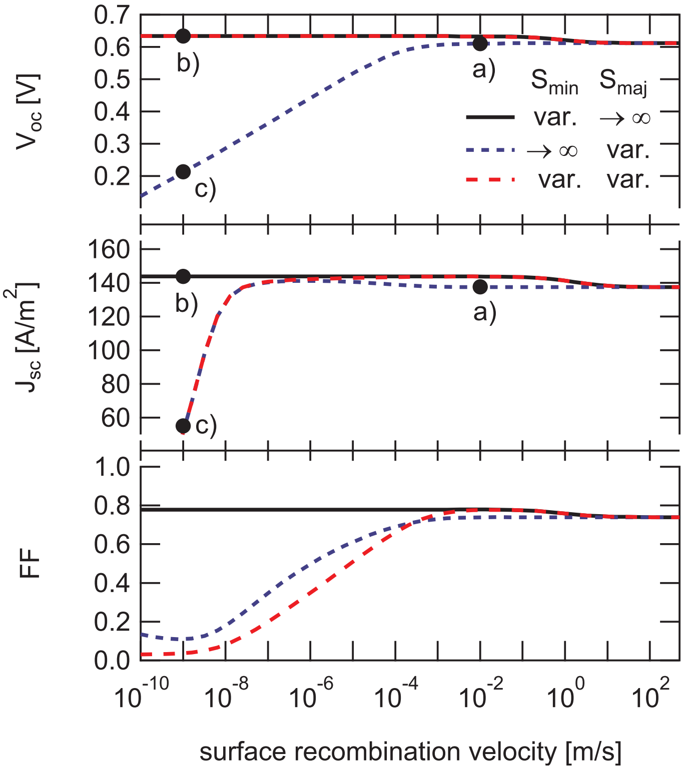

Figure 7.8.: Surface recombination velocity dependence of V_{oc}, J_{sc} and fill factor for a capped Langevin recombination ($\mu_{crit} = 10^{-8}$ m^2/Vs). J_{sc} but also V_{oc} is reduced by a finite majority surface recombination velocity S_{maj}. A reduced minority surface recombination S_{min} dominantly stabilizes and enhances V_{oc}.

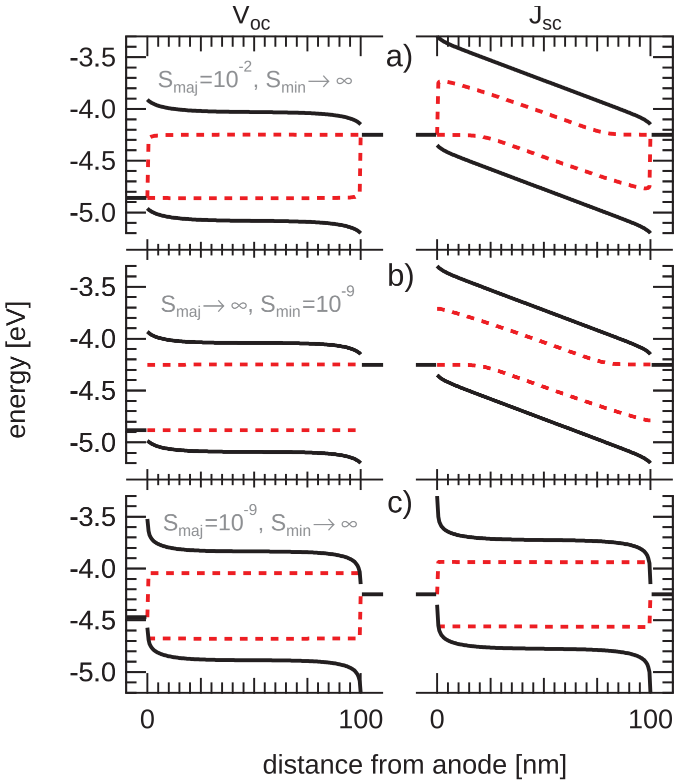

Figure 7.9.: Device band diagrams at V_{oc} (left) and J_{sc} (right) conditions for the surface recombination velocities marked in Fig. 7.8. Solid lines indicate the semiconductor LUMO (top) and HOMO (bottom) energies with the corresponding dotted quasi-Fermi levels for electrons and holes. A finite surface recombination velocity generates a (macroscopic) discontinuity of the quasi-Fermi levels and work functions of the electrodes.

7.5. Conclusion

A detailed analysis of the power conversion efficiency of BHJ solar cells was presented in this chapter. Injection barriers generally lower the power conversion efficiency whereas a reduction of the Langevin recombination rate as observed in experiments leads to an increase in device performance. However, both only slightly affect the power conversion efficiency of the device in contrast to the charge carrier mobilities. The maximum power conversion efficiency was shown to be a trade-off between J_{sc}, maximum for efficient charge transport conditions and V_{oc}, conversely optimal for high charge carrier densities within the active layer.

Charge carriers are accumulated in the device at low charge carrier mobilities and V_{oc} is enhanced. J_{sc} in contrast is low, rather due to the slow charge carrier extraction than recombination. At high charge carrier mobilities, charge carriers are efficiently extracted from the device, however the high recombination results in a low V_{oc}. The maximum power point requires an optimal combination of V_{oc} and J_{sc}. A maximum photocurrent should be extracted which still leaves a highly charged device. Consequently, a power conversion efficiency maximum is found for moderate charge carrier mobilities of about 10^{-7} to 10^{-8} Vs/m^2.

The Langevin recombination prefactor γ which is expected to saturate at higher mobilities was shown not to influence this trend. Limited minority surface recombination velocities passivate the metal electrodes by preventing surface recombination. The gained charge carrier densities increase V_{oc} and the device performance. In combination with a capped Langevin recombination, this can generate increased and mobility independent power conversion efficiencies for highly mobile semiconductors. Finite majority recombination velocities represent current transport barriers at the electrodes and therefore accumulate space charges at metal–organic interfaces which reduce J_{sc}. Moderate balanced surface recombination velocities of about 1.0 m/s however help to increase the device performance.

An enhancement of the charge carrier mobility from the state-of-the-art of approximately 10^{-8} m^2/Vs to about 10^{-6} m^2/Vs to 10^{-7} m^2/Vs as well as applying an optimal surface recombination velocity of around 0.1 m/s improved the power conversion efficiency by about 20 % to 40 % for both used parameter sets. All calculations have consistently shown that not high mobility semiconductors and perfect contacts will result in the most efficient solar cell, but rather the compounds offering an optimal compromise between an optimized J_{sc} and V_{oc}. One of the future goals of organic solar cell research should therefore be to find these optimal combinations. The presented results have been published in Ref. [146] and Ref. [121].

8. Charge carrier recombination in organic semiconductors

The Langevin theory is considered to be the dominant recombination mechanism for most applications in organic photovoltaics. Recent time transient measurements show however that the charge carrier densities in organic BHJ solar cells do not decay by the expected quadratic power law ($R \propto n^2$) but by seemingly much higher recombination orders [69, 78, 147]. The observed recombination rates are generally lower in comparison to the theoretical predictions. Thus, the dominating recombination mechanism is still under controversial discussion. In organic electronics, charge carrier recombination is assigned to geminate and nongeminate processes which occurs within the bulk of the semiconductor as well as at metal–organic interfaces [129, 148]. Whereas geminate recombination in general limits the charge carrier generation during the separation processes of bound electron–hole pairs [112, 149], nongeminate recombination occurs during the transport of free charges [69, 147] or at electrodes.

For low charge carrier mobilities such as found in organic semiconductors and illumination levels of about one sun, Langevin recombination is expected to be dominant [9, 62]. Current extraction experiments such as photo-CELIV (charge extraction by linearly increasing voltage) determine the recombination rate. However, the results lead to a clear overestimation of the recombination rate by the Langevin theory. As this effect has been known of for some time, various models have been proposed to explain this behavior [66, 150]. However, none of these models was able to predict the monitored temperature dependencies correctly.

Consequently, a series of numerical simulations are performed to determine the origin of mismatches between the Langevin theory and measurements. The probable origin of this deviation is found in the spatial distribution of recombination partners caused by selective contacts.

8.1. Existing models for a reduced recombination

In terms of the direct recombination of free charge carriers, the Langevin theory is widely believed to be the dominant recombination mechanism. This theory is based on a classical model of solved ions in aqueous solution. The recombination is defined as a function of the dielectric constant which is responsible for the strength of the Coulomb interaction as well as the mobilities of both recombination partners,

$$\gamma = \frac{q}{\varepsilon_0 \varepsilon_r} \left(\mu_n + \mu_p\right). \tag{8.1}$$

It describes the recombination of two independent charge carriers. Electron and hole have to find each other in order to recombine at a certain location. A general recombination model is defined by

$$R_{model} = k \left(np - n_i^2\right). \tag{8.2}$$

The Langevin recombination rate is obtained if k is substituted by the Langevin prefactor γ. According to the Langevin theory, the finding process of the recombination partners limits the charge carrier recombination [9]. The recombination itself is assumed to proceed much faster.

Since measured recombination rates are generally lower, several models have been presented to explain this difference. They are summarized in Fig. 8.1. In contrast to (a) the classical picture of charge carriers which are transported freely within their transport bands, Koster et al. (b) accounted for the phase separation of donor and acceptor molecules in BHJ solar cells [66]. Hence, charge carriers are only able to recombine at a heterointerface where the faster of the two charge carriers must wait for its recombination partner to approach. Consequently, the Langevin recombination is dominated by the mobility of the slower charge carrier,

$$\gamma_K = \frac{q}{\varepsilon_0 \varepsilon_r} \cdot \min\left(\mu_n, \mu_p\right). \tag{8.3}$$

A competing model by Adriaenssens and Arkhipov (Fig. 8.1 (c)) predicted a charge accumulation in local potential wells generated by potential fluctuations in one ambipolar effective medium. In order to recombine, one of both charges has to overcome the energy barrier ΔE to reach the spatial position of its recombination partner where both eventually recombine [150],

$$\gamma_A = \frac{q}{\varepsilon_0 \varepsilon_r} \exp\left(-\frac{\Delta E}{k_B T}\right) \left(\mu_n + \mu_p\right). \tag{8.4}$$

The spatial distance between electron and hole is neglected. For application in organic solar cells, the energy difference ΔE can be interpreted as the difference between either the LUMO or the HOMO levels of the involved donor and acceptor materials.

Recombination rates are determined by photo-CELIV experiments, for instance. During the measurement, a solar cell is illuminated by a laser pulse which generates free charge carriers within the active layer. After a delay time ranging from 100 nanoseconds to several milliseconds, the remaining excess charge carriers are extracted by an externally applied, linearly increasing voltage. The charge carrier density $n(t_{delay})$ and the charge carrier mobility μ are simultaneously determined by the shape of the detected signal [78, 147]. Ref. [151] is recommended as a general overview of the photo-CELIV experiment.

Subsequently, the recombination rate is accessible through two different approaches. Either the extracted charge carrier density and the mobility is inserted into the Langevin equation R_{ext} (Eqn. (8.2)) or the delay time dependent charge carrier density is interpreted by

$$R_{CELIV} = \frac{\mathrm{d}n(t_{delay})}{\mathrm{d}t_{delay}}. \tag{8.5}$$

Both procedures differ fundamentally. The retrieved value for charge carrier density and mobility denote the spatial average of all charges which were previously located in the device. In contrast, the time dependent change of the charge carrier density returns the spatial resolved recombination in the device before the extraction collects the remaining excess charge carriers.

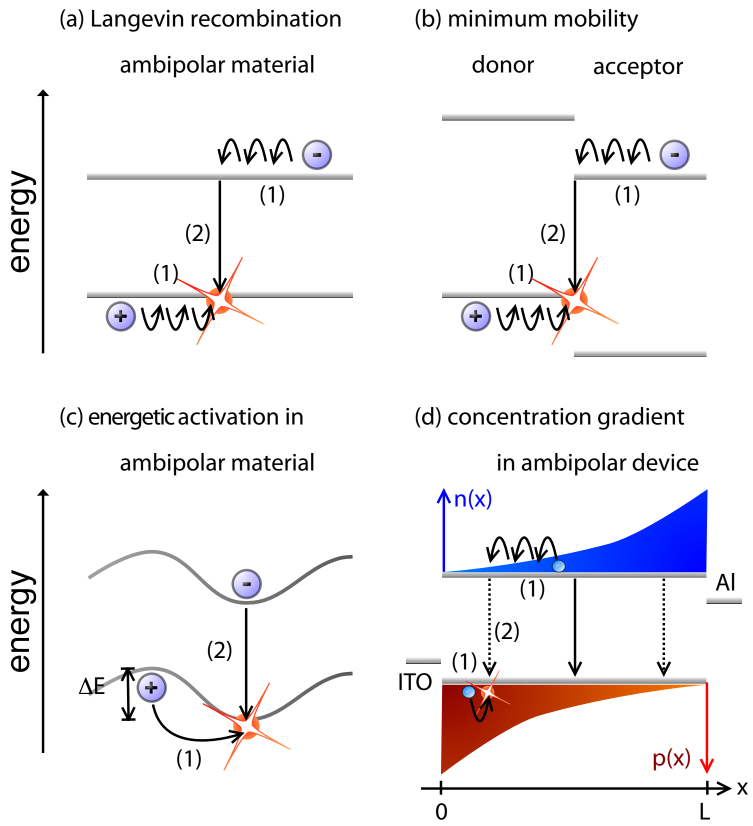

Figure 8.1.: Recombination models based on the Langevin recombination. In contrast to (a) the pure Langevin recombination, models considering (b) local spatial γ_K or (c) local energetic γ_A discontinuities predict reduced recombination rates. A reduced recombination is also generated by the (d) inverse distributions of electrons $n(x)$ and holes $p(x)$ caused by selective contacts. For all models, two recombination partners finding each other (1) is considered to be the limiting process. The actual recombination (2) is considered to be fast.

Such photo-CELIV experiments were performed on P3HT:PC$_{61}$BM BHJ solar cells with pristine and thermally annealed active layers [55, 147]. Subsequently, the deviations between both methods were determined. As a simple figure of merit, the reduction factor ζ is defined,

$$\zeta = \frac{R_{ext}}{R_{CELIV}}. \tag{8.6}$$

For pristine active layers, the deviation ζ shows a behavior which is rather temperature independent (not shown). However, a with temperature increasing deviation for annealed solar cells is observed [55, 147]. A similar result was found by Juška at al. [68]. The presented models as well as experimental data on the recombination mismatch are summarized in Fig. 8.2. The presented models by Koster and by Arkhipov predict inverse temperature behaviors.

The GDM model (Eqn. (2.5)) is commonly used to model the temperature dependence of the charge carrier mobility. It generally predicts an exponentially decreasing mobility with falling temperature, depending on the disorder factor σ. However, the opposing trends of the

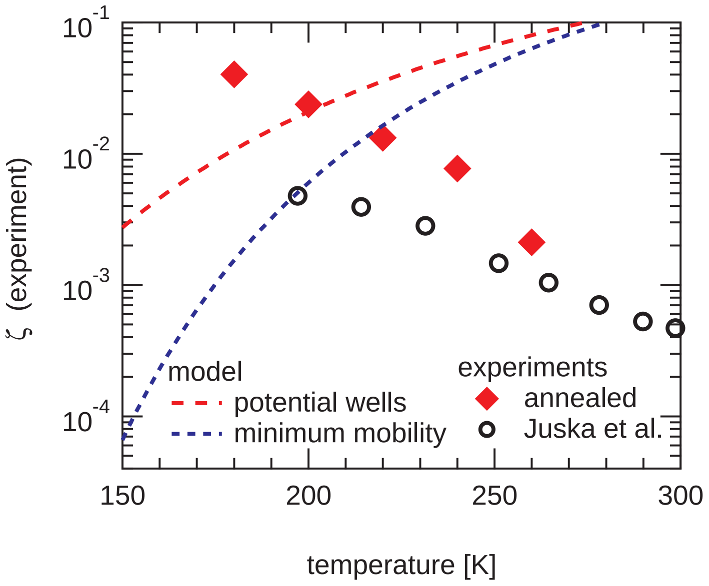

Figure 8.2.: Temperature dependence of the mismatch between the recombination rate calculated according to the Langevin theory using extracted charge carrier densities and the measured time dependent charge carrier density decay [55, 68]. In contrast to the measured mismatch, all models presented so far predict an inverse temperature behavior [66, 150].

presented models remain intact in contrast to the measurements.

8.2. The charge carrier gradient model

In order to pinpoint the origin of the found deviations, the basic differences between an experimental technique, a mathematic model and a device with boundary conditions must be carefully considered. Experiments which are used to determine the charge carrier concentration after a time delay mostly include a charge carrier extraction after a generation event. The amount of extracted charge carriers n_{ext} which were formally located in the device is yielded from the detected photocurrent. The obtained charge carrier density is commonly assumed to be equal for electrons and holes. The recombination rate is consequently defined as

$$R_{ext} = \gamma \, (n_{ext})^2 \,. \tag{8.7}$$

Thus, an implicit integration over the full thickness of the active layer is made in order to determine the average charge carrier density which was formerly distributed in the device. As a solar cell represents a macroscopic structure of several tens of nanometer thickness, all spatial information on the former charge carrier distribution is lost. The Langevin theory however requires that the recombination partners are at the same location. The recombination therefore depends on the distributions of electrons and holes and represents a potential source of systematic errors. The error approaches a significant value if the spatial charge carrier distributions in the active layer cannot be expected to be homogeneous.

In order to build a functioning BHJ solar cell, selective contacts are required. The active layer is consequently sandwiched between an anode and a cathode respectively with a low and a high work function. Such contacts generate an electric field and strong charge carrier gradients in the device. The charge carrier gradients are inversed for electrons and holes. Thus, a hole concentration which is orders of magnitude higher than the electron density is injected at the anode and conversely at the cathode. Neglecting a transport of photogenerated charges and assuming the validity of the thermionic emission theory, the charge carrier distributions under illumination at short circuit conditions are approximated well by

$$n(x) = n_n \exp\left(-\alpha \frac{x}{L}\right), \tag{8.8}$$

$$p(x) = p_p \exp\left(-\alpha \frac{L-x}{L}\right). \tag{8.9}$$

Here, $\alpha = \ln(n_n/n_p) = \ln(p_p/p_n)$, with the electron n_n and hole p_n densities at the cathode as well as n_p and p_p at the anode. The spatial position is denoted by x within the active layer of thickness L. Such typical profiles are schematically shown in Fig. 8.1(d) as well as the inset of Fig. 8.3. Charge carriers generated by optical excitation are treated as a constant, small additive term to both distributions. However, this will not influence the general trend. The theoretically defined recombination rate denotes the average of the spatially resolved discrete rates,

$$R_{theory} = \frac{1}{L}\gamma \int\limits_0^L \Big(n(x)\cdot p(x)\Big)\mathrm{d}x = \gamma\left(\overline{np}\right) \tag{8.10}$$

with known spatial distributions of electrons and holes. Thus, R_{theory} is comparable to the recombination rate yielded in photo-CELIV experiments, R_{CELIV}. From charge extraction experiments, only the separate integrals over the extracted electron and hole charge carrier densities are yielded,

$$R_{ext} = \frac{1}{L^2}\gamma \left(\int\limits_0^L n(x)\mathrm{d}x \cdot \int\limits_0^L p(x)\mathrm{d}x\right) = \gamma\left(\overline{n}\cdot\overline{p}\right). \tag{8.11}$$

The difference between both equations defines ζ according to Eqn. (8.6),

$$\zeta = \frac{\frac{1}{L}\int_0^L n(x)p(x)\mathrm{d}x}{\frac{1}{L}\int_0^L n(x)\mathrm{d}x \cdot \frac{1}{L}\int_0^L p(x)\mathrm{d}x}. \tag{8.12}$$

A basic approximation by Eqns. (8.8) and (8.9) reads

$$\zeta = \alpha^2 e^{-\alpha}\left(1-e^{-\alpha}\right)^{-2}. \tag{8.13}$$

The calculated reduction factor ζ versus the charge carrier gradient between cathode and anode is plotted in Figure 8.3. A symmetric distribution of electrons and holes was assumed. The mismatch between both methods increases with steeper charge carrier gradients. The

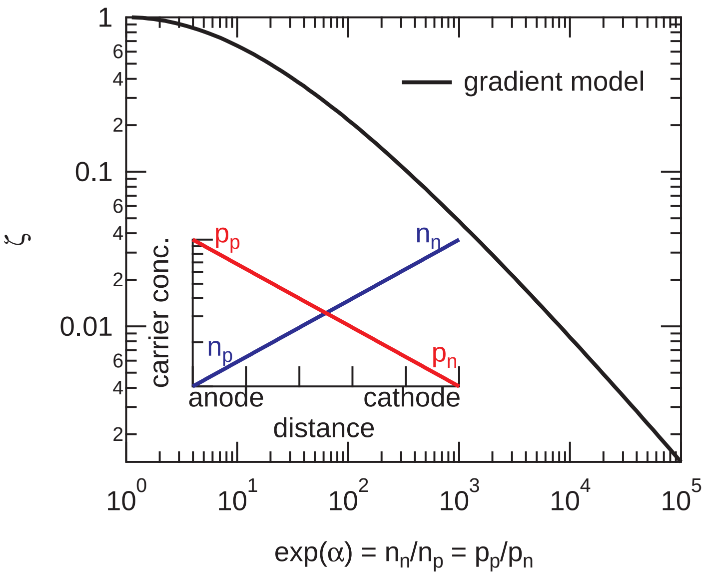

Figure 8.3.: Simple model on the origin of a recombination rate mismatch between theory and charge extraction experiments. An exponential distribution of electrons and holes between both contacts according to Eqn. (8.13) is assumed. The charge carrier gradients are depicted in the inset. The observed mismatch increases with steeper charge carrier gradients.

mismatch is consequently influenced by all parameters which change the charge carrier density distributions in the device. Most important, the model implies that ζ does not depend on a specific recombination mechanism, but on the distribution of the charge carriers in the device.

8.3. Numerical validation

In order to validate the charge carrier gradient model, a number of numeric simulations were performed. The parameter set is listed in Tab. 8.1. Mirror charge effects at the metal–organic interfaces were included in order to define a more realistic device. They are described according to the common model of Scott and Malliaras [82]. For simplicity, only the electric field independent contribution was considered,

$$S = 16\pi\varepsilon_0\varepsilon_r(k_BT)^2\mu/q^3. \tag{8.14}$$

The charge carrier generation was set to be homogeneous throughout the device, combined with a non-reduced Langevin recombination. The dependence of the charge carrier mobility on temperature was considered by the GDM model (Eqn. (2.5)) [14].

The spatial electron and hole distributions are shown in Fig. 8.4 for (a) J_{sc}, (b) V_{oc} and (c) V_{bi} conditions. Photo-CELIV measurements are performed under the latter condition in order to achieve flat LUMO and HOMO bands. However, due to selective contacts which create band bending, flat-band conditions generally do not exist in organic solar cells [152]. In all cases, a ζ smaller than unity is calculated according to Eqn. (8.12). Thus, charge extraction

parameter	symbol	value	unit
effective band gap	E_g	1.10	eV
charge carrier mobilities	μ_n, μ_p	$1.0 \cdot 10^{-8}$	$\mathrm{m^2/Vs}$
active layer thickness	L	100	nm
generation rate	G	$6.0 \cdot 10^{27}$	$\mathrm{1/m^3s}$
temperature	T	300	K
relative dielectric permittivity	ε_r	3.4	
effective density of states	N_c, N_v	$1.0 \cdot 10^{26}$	$\mathrm{1/m^3}$
injection barriers			
- cathode	Φ_n	0.1	eV
- anode	Φ_p	0.1	eV

Table 8.1.: Simulation parameters for explaining a reduced Langevin recombination. The temperature dependent mobility was calculated using the GDM model with an disorder parameter σ = 75meV [14].

experiments usually generate severe overestimations of the recombination rate if the yielded average charge carrier densities are directly inserted into the recombination equation.

The charge carrier gradients are strongest at short circuit conditions. They are reduced with increasing applied voltage due to transported charge carriers. Similarly, high mobilities create steeper gradients. The polaron recombination probability is at its maximum in the middle of the ambipolar active layer whereas it is at its lowest directly at the contacts.

The different interpretations of the charge carrier distributions, either by multiplying the average charge carrier densities $\overline{n} \cdot \overline{p}$ or by using the spatially resolved recombination partner density $\overline{np}$, are shown in Fig. 8.5 (a) for different mobilities. As low injection barriers create strong charge carrier gradients, the mismatch in terms of the ζ-factor (b) is high. The recombination rates R_{theory} are shown in (c) together with the corresponding overestimated rates,

$$R_{theory} = \frac{R_{ext}}{\zeta} = \gamma n_{ext}^2. \tag{8.15}$$

The charge carrier densities are more and more homogeneously distributed with increasing illumination. Thus, the gradients are lowered and ζ gradually converges to unity.

The experimentally observed temperature dependence of the mismatch factor is well reproduced by the simulation as shown in Fig. 8.6. In contrast to the previously mentioned models, the reduction factor decreases with higher temperatures due to an improved charge carrier mobility. The decreasing mismatch with growing applied voltage also matches the observations by Juška et al. [78].

However, the measured reduction factors still differ by a constant factor of 0.1 to 0.005 from the theoretical result. This additional reduction is independent of electric field, temperature or illumination. Thus, the ζ-factor is composed out of two shares,

$$\zeta(T,F,G) = \zeta_{gradient}(T,F,G) \cdot \zeta_{static}. \tag{8.16}$$

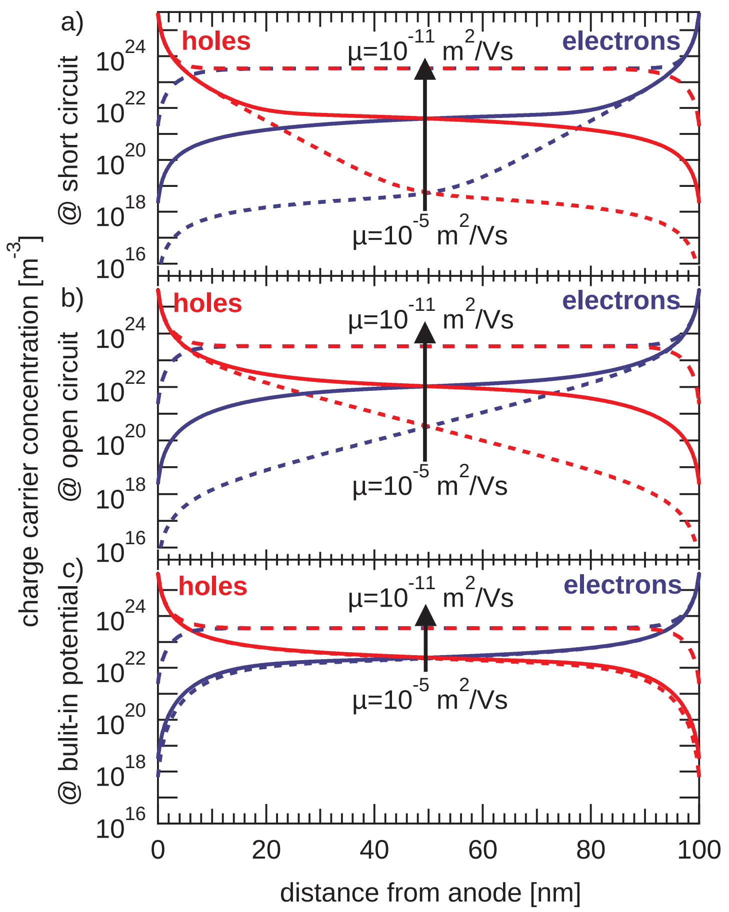

Figure 8.4.: Simulated charge carrier distributions for (a) short circuit, (b) open circuit and (c) built-in potential conditions at an illumination of 1 sun. The influence of balanced mobilities of $\mu = 10^{-5}$ m^2/Vs (short dashed lines), 10^{-8} m^2/Vs (solid lines) and 10^{-11} m^2/Vs (long-dashed lines) is shown in each graph. Electron and hole concentrations are highest at the cathode and anode, respectively, due to selective contacts.

The first part, as a function of temperature, electric field and illumination is fully explained by the gradient model. The remaining constant share was not predicted by the numeric simulation. Hence, its origin must go beyond the included models. Different dielectric constants for donor and acceptor molecules or semiconductor phase separations are for example possible origins [153].

A temperature independent reduction factor based on variable dielectric constants was proposed by Szmytkowski [154],

$$\zeta_{Szm.} = \left| \frac{\varepsilon_d - \varepsilon_a}{\varepsilon_d + \varepsilon_a} \right| . \tag{8.17}$$

With typical values for the relative permittivity of the donor ε_d of 3.4 for P3HT and ε_a of 4.0 for the acceptor PC$_{61}$BM, a constant reduction factor of 0.08 is yielded. However, there is as

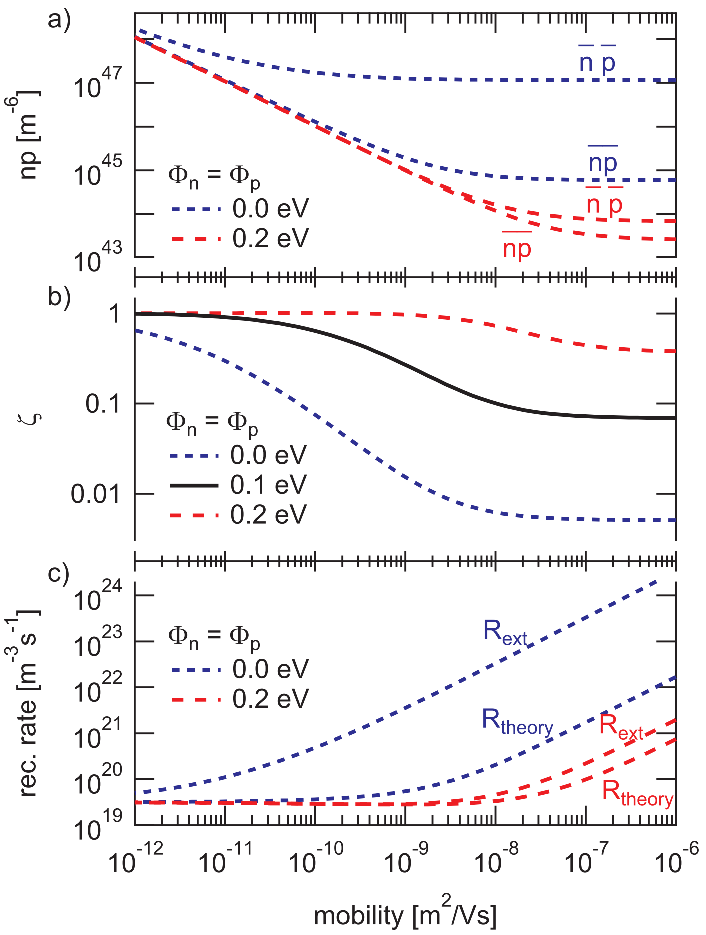

Figure 8.5.: Differences in the analyses of recombination rates under variation of the charge carrier mobility. The shown dependencies were calculated at built-in potential conditions enabling a direct comparison with the photo-CELIV experiment. The amount of extractable charges is obtained from charge extraction measurements. Any spatial information on the former charge carrier distribution is therefore lost. The recombination rate R_{ext} (a) is therefore determined by the sums of extracted charge carriers $\overline{n} \cdot \overline{p}$. In contrast, the theory R_{theory} actually requires the sum of the (spatially distributed) recombination partners $\overline{np}$. The mismatch (b) between both scenarios defines the recombination reduction factor ζ. The deviation intensifies with increasing charge carrier mobility as the charge carrier gradients become steeper. The correlated recombination rates $R_{ext} = R_{theory}/\zeta$ are depicted in (c).

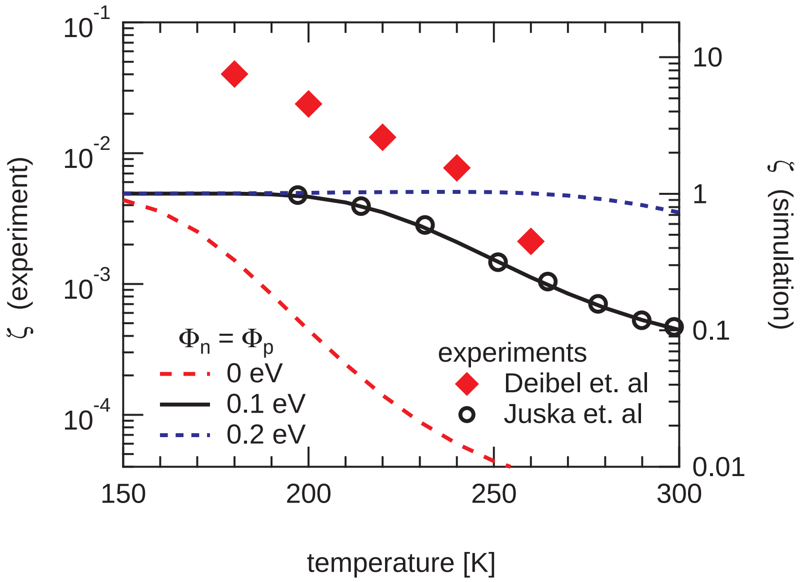

Figure 8.6.: Comparison of the temperature dependent recombination reduction factor ζ determined by photo-CELIV (symbols, as Fig. 8.2) as well as by the simulation with selected injection barriers (lines). The temperature dependence is well matched. A static, temperature independent share to ζ remains.

yet no known experimental proof of this theory.

Constant reductions of the Langevin recombination between 0.1 and 1 have been reported by Monte Carlo simulations of electron and hole hopping transport in blended semiconductors [155]. This deviation is based on energetic disorder, domain sizes and imbalanced mobilities. Also, a further constant reduction was proposed which is based on deep trapped charge carriers, which are known to appear in organic semiconductors in large numbers [156, 157].

Finally, also shallowly trapped charges that are excluded from recombination in larger domains would generate a similar effect and probably cause recombination orders higher than two [80].

8.4. Conclusion

A mismatch between two different methods to determine the recombination rate from photo-CELIV measurements was observed. The recombination rate in organic BHJ solar cells was measured by the decay time dependent charge carrier concentration. Additionally, the recombination rate can be calculated if the extracted charge carrier densities are inserted into the Langevin equation. However, the latter option systematically overestimates the measured recombination rates. Models explaining this difference already existed. However, they all predicted an inverse and therefore incorrect temperature dependence of the observed deviation. Consequently, a new model based on the distribution of recombination partners within the ambipolar active layer was introduced. Such inhomogeneous distributions of electrons and holes will be inevitably generated by selective contacts.

The spatial charge carrier distributions were calculated by numeric simulations and were interpreted in analogy to the CELIV experiment. Thus, the charge carrier density was used to determine the spatially resolved recombination rate in the device. In addition, the total amount of extractable excess charge carriers was calculated and inserted into the Langevin equation. This approach is equivalent to a charge carrier extraction experiment. A recombination rate mismatch was observed between both methods which was identical to the experiment. All dependencies on temperature, illumination and applied voltage were qualitatively reproduced.

A remaining static share of the reduction factor was not predicted by the presented simulation. Deviations in the dielectric permittivities of donor and acceptor could be the origin. Also the morphology of the blended active material is a possible source. The morphology was recently shown to cause recombination orders above two [38, 80, 158].

The spatial distribution of recombination partners in BHJ solar cells can be expected to be strongly inhomogeneous for most organic BHJ solar cells. This should always be considered if charge extraction experiments are performed as it can lead to severe misinterpretations in terms of the recombination rate. The charge carrier gradients originate from selective contacts which are required to generate an electric field in the solar cell. The resulting spatially inhomogeneous recombination rate applies to all nongeminate recombination processes. Thus, a mismatch will be observed even if the Langevin recombination is not the dominating recombination mechanism.

In comparison to organic semiconductors, inorganic semiconductors generally do not have such strong charge carrier gradients due to their high doping concentrations. Experimental methods which are well established to detect the type of recombination in inorganic devices are therefore error-prone as soon as they are based on charge extraction. Reliable results can only be achieved if the charge carrier gradients are additionally considered. Thus, experimental results said to uniquely prove a trap-assisted SRH recombination in organic bulk heterojunction solar cells are fully reproducible assuming a pure Langevin recombination [159–161].

The results presented in this chapter have been published in Ref. [67].

9. Conclusion

Within the last ten years, organic solar cells have evolved from a scientifically challenging project into a technology currently yielding power conversion efficiencies of above 10 %. Even though the commercial market is still dominated by inorganic solar cells, the outstanding progress of organic photovoltaics has already bred the first commercially available products [8]. Assuming a comparable development in coming years, an affordable alternative to relatively expensive inorganic solar cells and panels will be developed [7].

Organic solar cells show a distinct current response to an applied voltage. These current–voltage characteristics are of crucial importance since they determine the power conversion efficiency of the solar cell. The curves are the result of a complex interplay between charge carrier generation, recombination and transport, among others. In order to interpret such measurements, a way to mathematically describe and predict current–voltage characteristics was looked for.

This goal was achieved by solving the drift–diffusion equation for electrons and holes, combined with Poisson and continuity equations. The description of an organic solar cell is valid if this equation system is extended by appropriate density of states distributions, boundary conditions as well as models for charge carrier generation and recombination. However, this equation system cannot be solved analytically. A one-dimensional numerical simulation was therefore developed. The simulation was written in the object oriented C++ programming language in order to create a fast and parallelized program that is easily extendible. The accessibility of the source code offers the chance to include necessary but also new or uncommon physical models in contrast to expensive commercial alternatives. With the help of this simulation program, current problems of organic photovoltaic research were subsequently investigated.

Different dependencies of V_{oc} on the illumination intensity were measured for BHJ and PHJ solar cells. The behavior could be reproduced by the simulation and was attributed to the charge carrier density distributions. Electrons and holes in PHJ solar cells are well separated from each other due to the pure semiconductor layers. Recombination is only possible directly at the heterointerface. Charge carriers in BHJ devices, in contrast, reside together in one effective layer and recombination is enabled throughout the active layer. The recombination rate is therefore lower in PHJ solar cells which results in higher charge carrier densities and a higher V_{oc} at high illumination intensities for such devices. The more equally distributed charge carrier densities in BHJ devices are advantageous at low illumination levels where recombination is less important. Thus, an intersection between the V_{oc} vs. illumination trends of both devices is observed [108].

Subsequently, an analytical formulation was developed in order to describe V_{oc}. Changing the injection barriers in the simulation led to three different V_{oc} regimes for both solar cell types. A constant V_{oc} is found if the injected charge carrier densities from the electrodes exceed the optically generated charge carrier density. Injected charge carriers diffuse into the semiconductor and generate an electric field which deters optically generated excess charge carriers in the bulk of the device. Bulk recombination consequently dominates V_{oc} in this regime. The electric field vanishes for higher injection barriers, which leads to a significant contribution of surface recombination to the total recombination rate. V_{oc} is limited by the injection barriers in this case. In PHJ solar cells, less minority charge carriers are located in the pure material layers due to the higher band gaps. This restricts surface recombination due to the lack of recombination partners and V_{oc} is less dependent on the injection barriers. Injection barriers (Φ_n, Φ_p) as well as the effective band gap E_g could be estimated from temperature dependent V_{oc} measurements [109].

From time to time, organic solar cells show S-shaped deformations in their current–voltage characteristics. Such deformations lead to a simultaneous reduction of V_{oc}, J_{sc} and the fill factor. Oxygen plasma treatments of the ITO anode were reproducibly able to create such deformations in BHJ solar cells. However, none of the models used for inorganic semiconductors applies. As injection barriers could be excluded as a possible origin, the influence of surface recombination was considered as a possible reason for the S-shape. Due to a reduced surface recombination velocity of holes at the anode, a space charge is created which generates the S-shape [129].

The device power conversion efficiency was shown to be a trade-off between V_{oc} and J_{sc}. The V_{oc} profits from high charge carrier densities in the solar cell, whereas J_{sc} requires good charge transport and charge extraction properties. With increasing mobility, the extracted photocurrent rises even though the recombination rate of free charge carriers is enhanced. Thus, J_{sc} is barely limited by recombination in contrast to V_{oc}, which decreases with rising mobility. At the maximum power point, a preferably high charging of the device must coincide with good charge carrier extraction. A charge carrier mobility of 10^{-6} to 10^{-7} $\mathrm{m^2/Vs}$ was shown to optimally balance these properties which results in optimal power conversion efficiencies [146].

The Langevin recombination is known from experiments to be limited at higher charge carrier mobilities [9]. This effect does however not significantly influence the previously determined optimal mobility for the power conversion efficiency. However, both metal electrodes can severely influence the performance of an organic solar cell. A limitation of the charge extraction at the electrodes by finite majority surface recombination velocities leads to a severe breakdown of J_{sc}. In contrast, V_{oc} is enhanced by preventing minority charge carriers from recombining at the surfaces. Since both effects occur at different surface recombination velocities, the effect can be used to further optimize the power conversion efficiency. Electrodes with limited surface recombination velocities of about 0.1 m/s instead of perfect contacts with infinitely fast transitions between the metal–organic interfaces result in more efficient solar cells [121].

Finally, an approach to explain a major discrepancy between measured and theoretically predicted Langevin recombination rates was presented. It was shown that charge carrier gradients generated by selective contacts have to be considered. Hence, recombination is a spatially site-selective process and has to be calculated accordingly. Charge extraction experiments yield the sum of all excess charge carriers in a device without information on their original distribution. This results in a systematic overestimation of the recombination if charge carrier densities deduced in such a way are inserted into rate equations [67, 160].

In addition to these main contributions, additional results have been obtained during recent years. This includes the attribution of a symmetry point in photocurrent measurements to quasi-flat bands inside BHJ solar cells [152]. The influence of doping and deep traps on current–voltage characteristics was discussed [156] as well as the influence of deep traps for solar cells printed on paper [7]. These results have been incorporated in the previous chapters.

The power of numerical drift–diffusion simulations was demonstrated by these examples. Especially in combination with experimental measurements unknown ties of organic photovolatics can be revealed. Thus, extending the use of such techniques in future will help to gain an even better picture of reality than the one yielded today.

Zusammenfassung

Organische Solarzellen entwickelten sich innerhalb der letzten Jahre, ausgehend von wissenschaftlicher Grundlagenforschung, zu einer Technologie, die heute mehr als 10 % des einfallenden Sonnenlichts in elektrischen Strom konvertiert. Obwohl der Markt für Solarzellen noch immer von Modulen aus anorganischen Materialien dominiert wird, sind bereits heute erste Produkte aus organischen Halbleitern kommerziell verfügbar. Bei einer vergleichbaren Entwicklung über die nächsten Jahre, entsteht so unaufhaltsam eine kostengünstige Alternative zu den relativ teuren Solarzellenmodulen aus anorganischen Materialien [7, 8].

Solarzellen verwandeln einfallendes Sonnenlicht in einen elektrischen Strom, der als Funktion der angelegten elektrischen Spannung extrahiert werden kann. Mit Hilfe dieser Strom-Spannungs-Kennlinien kann die Effizienz einer Solarzelle bestimmt werden. Diese Kennlinien entstehen durch ein komplexes Zusammenspiel von Ladungsträgergeneration, -rekombination und -transport in den aktiven Halbleiterschichten. Um Messungen an organischen Solarzellen besser interpretieren zu können und um Vorhersagen über Ihr Verhalten bei sich ändernden Bedingungen zu treffen, wurde nach einer Möglichkeit gesucht diese Strom-Spannungs-Kennlinien mathematisch zu beschreiben.

Ein Ansatz hierfür, der in dieser Arbeit umgesetzt wurde, stellt das gleichzeitige Lösen der Drift-Diffusions-Gleichungen, der Kontinuitätsgleichungen sowie der Poissongleichung für Elektronen, Löcher und Exzitonen dar. Organische Solarzellen werden mit diesem Gleichungssystem beschrieben, indem entsprechende Randbedingungen, Zustandsdichteverteilungen und Modelle für die Ladungsträgergeneration sowie -rekombination hinzugefügt werden. Das resultierende Gleichungssystem ist jedoch nicht mit analytischen Methoden lösbar. Daher musste ein numerischer Ansatz entwickelt werden, der das Gleichungssystem in einer Dimension iterativ löst. Ein schnelles und leicht zu erweiterndes Simulationsprogramm wurde, basierend auf der objektorientierten Programmiersprache C++ entwickelt. Im Gegensatz zu relativ teuren kommerziellen Alternativen erlaubt die Verfügbarkeit des Quellcodes die Definition von gebräuchlichen aber ebenso neuen physikalischen Modellen, die nach Belieben kombinierbar sind. Im Anschluss konnte diese Simulation dazu verwendet werden aktuelle Fragestellungen der Forschung an organischen Solarzellen zu bearbeiten.

Die gemessenen offenen Klemmspannungen V_{oc} von *planar-* (PHJ) und *bulk-heterojunction* (BHJ) Solarzellen zeigen abweichende Abhängigkeiten von der Beleuchtungsstärke. Mit Hilfe der Simulation konnte dieses Verhalten reproduziert werden und auf die Verteilungen der Ladungsträgerdichten in den Solarzellen zurückgeführt werden. In PHJ Solarzellen befinden sich Elektronen und Löcher in zwei unterschiedlichen, voneinander getrennten Materialschichten. Eine Rekombination von Ladungsträgern ist somit nur an deren direkter Grenzfläche möglich. In einer BHJ Solarzelle befinden sich im Gegensatz dazu alle Ladungsträger in einer effektiven Schicht womit, insbesondere bei hohen Beleuchtungsintensitäten, die Rekombinationsrate erhöht ist. Dies führt zu geringeren Ladungsträgerdichten und damit zu einem erniedrigten V_{oc} im Vergleich mit PHJ Solarzellen. Im Gegensatz dazu führen die ausgeglichenen Verteilungen der Ladungsträgerdichten bei geringen Beleuchtungsintensitäten zu einem geringeren internen elektrischen Feld in BHJ Solarzellen und somit zu einem V_{oc} welches das von PHJ Solarzellen übersteigt. Der Einfluss der Rekombination ist in diesem Fall gering. Somit kann ein Schnittpunkt der beiden beleuchtungsabhängigen V_{oc} Verläufe beobachtet werden [108].

Im darauffolgenden Schritt wurde eine analytische Beschreibung für V_{oc} entwickelt. Durch Änderungen der Injektionsbarrieren in der Simulation konnten drei unabhängige Einflussbereiche auf V_{oc} gefunden werden. Solange die Injektionsbarrieren gering sind und die injizierten Ladungsträgerdichten die optisch Generierten übersteigt, bleibt V_{oc} konstant. Ladungsträger diffundieren in diesem Fall von den Elektroden in die Halbleiterschicht und erzeugen dabei ein elektrisches Feld, das optisch erzeugte Überschussladungsträger von den Elektroden fern hält. Diese Überschussladungsträger rekombinieren somit im Volumen der aktiven Schicht. Mit steigenden Injektionsbarrieren verschwindet dieses elektrische Feld. Ladungsträger diffundieren somit ohne Einschränkungen zu den Elektroden, die nun als Rekombinationszentren für Oberflächenrekombination dienen. V_{oc} wird in diesem Fall direkt von den Injektionsbarrieren limitiert. PHJ Solarzellen sind im Allgemeinen weniger anfällig für Änderungen der Injektionsbarrieren. Durch ihre größeren optischen Energielücken befinden sich weniger Minoritätsladungsträger in den reinen Halbleiterschichten. Da ein Stromtransport zu den Elektroden aufgrund der fehlenden Minoritäten unterbunden ist, bleibt V_{oc} zunächst länger konstant. Aus temperaturabhängigen V_{oc} Messungen konnte die effektive Bandlücke E_g sowie die Injektionsbarrieren (Φ_n, Φ_p) von BHJ und PHJ Solarzellen bestimmt werden [109].

Strom-Spannungs-Kennlinien organischer Solarzellen zeigen von Zeit zu Zeit S-förmige Deformationen. Solche Deformationen oder auch Gegendioden führen zu einer gleichzeitigen Reduktion von V_{oc}, dem Kurzschlussstrom J_{sc} sowie dem Füll Faktor. In BHJ Solarzellen können diese Deformationen beispielsweise durch eine Sauerstoffplasma-Behandlung der Anode (ITO) erzeugt werden. Keiner der etablierten Erklärungsansätze für solche Deformationen trifft in diesem Fall jedoch zu. Da Injektionsbarrieren als mögliche Ursache ausgeschlossen werden können, wurde der Einfluss von reduzierten Oberflächenrekombinationsraten untersucht. Aufgrund einer begrenzten Oberflächenrekombinationsgeschwindigkeit sammeln sich Löcher an der Anode an, die eine Raumladungszone erzeugen und so für das S-förmige Verhalten verantwortlich sind [129].

Zudem konnte gezeigt werden, dass der optimale Wirkungsgrad einer organischen Solarzelle stets einen Kompromiss zwischen optimiertem V_{oc} und optimiertem J_{sc} darstellt. Während V_{oc} durch hohe Ladungsträgerdichten in einer Solarzelle gesteigert wird, profitiert J_{sc} von guten Ladungstransport- und damit Extraktionseigenschaften. Mit steigender Beweglichkeit der Ladungsträger steigt J_{sc} während V_{oc} sinkt. Beide Größen verhalten sich somit gegenläufig bei Mobilitätsänderungen. Am Punkt maximaler Leistung muss eine möglichst hohe Aufladung der Solarzelle mit einer ebenfalls guten Ladungsträgerextraktion zusammenfallen. In organischen Solarzellen führt dieser Kompromiss zu einer optimalen Solarzelleneffizienz bei Ladungsträgermobilitäten zwischen 10^{-6} und 10^{-7} m^2/Vs. Höhere oder niedrigere Ladungsträgerbeweglichkeiten führen zu einer deutlichen Abnahme des Wirkungsgrades organischer Solarzellen [146].

Bei hohen Ladungsträgerbeweglichkeiten ist die Langevin-Rekombination dafür bekannt in eine von der Mobilität unabhängige Rate überzugehen [9]. In organischen Solarzellen beeinflusst dieser Effekt jedoch nicht die zuvor bestimmten optimalen Beweglichkeiten für eine maximale Solarzelleneffizienz. Jedoch können die Elektroden maßgeblichen Einfluss auf die Effizienz nehmen. Eine Limitierung der Oberflächenrekombinationsgeschwindigkeit an den Elektroden für Majoritäten führt zu einer starken Reduzierung von J_{sc} aufgrund der schlechten Ladungsträgerextraktionseigenschaften einer solchen Solarzelle. V_{oc} wird im Gegensatz dazu von einer begrenzten Oberflächenrekombination von Minoritäten erhöht. Da beide Effekte bei unterschiedlichen Geschwindigkeiten der Oberflächenrekombination auftreten, kann dieser Effekt benutzt werden um die Effizienz einer Solarzelle zu steigern. Elektroden mit einer begrenzten Oberflächenrekombinationsgeschwindigkeit von 0.1 m/s für Elektronen und Löcher maximieren die Effizienz der Solarzelle. Bei höheren Transfergeschwindigkeiten rekombinieren Ladungsträger in den Elektroden, bei niedrigeren Geschwindigkeiten werden Raumladungszonen an den Kontakten aufgebaut. Elektronen- und lochleitende Schichten erzeugen vor Kathode und Anode einen vergleichbaren oberflächenpassivierenden Effekt [121].

Schließlich wurde versucht einen systematischen Unterschied zwischen gemessenen und theoretisch bestimmten Rekombinationsraten zu erklären. So konnte gezeigt werden, dass der Einfluss von selektiven Kontakten auf die Volumenrekombination berücksichtigt werden muss. Folglich muss die Rekombination als ortsaufgelöster Prozess betrachtet und ebenso bestimmt werden. Ladungsextraktionsexperimente liefern stets die Summe aller Überschussladungsträger, die sich in einer Solarzelle befinden. Informationen über ihre vorherige Verteilung in der Solarzelle gehen bei der Messung verloren. Werden solche Messergebnisse blind in eigentlich ortsaufgelöste Ratengleichungen eingesetzt, führt dies zu einer systematischen Überschätzung der real existierenden Rekombination in organischen Solarzellen [67, 160].

Durch die hier gezeigten Beispiele konnten Anwendungsbereiche einer numerischen Drift-Diffusion-Simulation aufgezeigt werden. Insbesondere in Kombination mit experimentellen Messungen konnten zuvor nicht offensichtliche Zusammenhänge in organischen Solarzellen erkannt und erklärt werden. Eine Ausweitung der Nutzung solcher Methoden kann somit dabei helfen, das bereits heute gute Verständnis von organischen Halbleitern stetig weiter zu verbessern.

Bibliography

[1] M. A. Green, K. Emery, Y. Hishikawa, W. Warta, and E. D. Dunlop, “Solar cell efficiency tables (version 40),” Prog. Photovolt. **20**, 5 (2012).

[2] H. Shirakawa, E. J. Louis, A. G. MacDiarmid, C. K. Chiang, and A. J. Heeger, “Synthesis of electrically conducting organic polymers: halogen derivatives of polyacetylene, $(CH)_x$,” J. Chem. Soc. **16**, 578 (1977).

[3] H. W. Kroto, J. R. Heath, S. C. O’Brien, R. F. Curl, and R. E. Smalley, “C60: Buckminsterfullerene,” Nature **318**, 162–163 (1985).

[4] N. S. Sariciftci, L. Smilowitz, A. J. Heeger, and F. Wudl, “Photoinduced electron-transfer from a conducting polymer to buckminsterfullerenes,” Science **258**, 1474 (1992).

[5] C. Lungenschmied, G. Dennler, H. Neugebauer, S. N. Sariciftci, M. Glatthaar, T. Meyer, and A. Meyer, “Flexible, long-lived, large-area, organic solar cells,” Sol. Energy Mat. Sol. Cells **91**, 379 (2007).

[6] T. Loewenstein, M. Rudolph, M. Mingebach, K. Strauch, Y. Zimmermann, A. Neudeck, S. Sensfuss, and Derck Schlettwein, “Textile-compatible substrate electrodes with electrodeposited zno—a new pathway to textile-based photovoltaics,” Chem. Phys. Chem. **11**, 783 (2010).

[7] A. Hübler, B. Trnovec, T. Zillger, M. Ali, N. Wetzold, M. Mingebach, A. Wagenpfahl, C. Deibel, and V. Dyakonov, “Printed Paper Photovoltaic Cells,” Adv. Ener. Mater. **1**, 1018 (2011).

[8] R. F. Service, “Outlook brightens for plastic solar cells,” Science **332**, 293 (2011).

[9] M. Pope and C. E. Swenberg, *Electronic Processes in Organic Crystals and Polymers* (Oxford University Press, USA, 2nd edition, 1999).

[10] G. Dennler, M. C. Scharber, and C. J. Brabec, “Polymer–fullerene bulk–heterojunction solar cells,” Adv. Mater. **21**, 1323 (2009).

[11] D. R. Gamota, R. Brazis, K. Kalyanasundaram, and J. Zhang, eds., *Printed organic and molecular electronics* (Kluwer Academic Publishers, 2004).

[12] R. E. Peierls, *Quantum Theory of Solids* (Oxford University Press, 2001).

[13] S. M. Sze and Kwok K. Ng, *Physics of semiconductor devices, Third edition* (John Wiley & Sons, Inc., 2007).

[14] H. Bässler, "Charge transport in disordered organic photoconductors," phys. stat. sol. (b) **175**, 15 (1993).

[15] P. W. Anderson, "Absence of diffusion in certain random lattices," Phys. Rev. **109**, 1492 (1958).

[16] R. A. Marcus, "On the theory of oxidation-reduction reactions involving electron transfer," J. Chem. Phys. **24**, 966 (1956).

[17] N. F. Mott, "Conduction in non-crystalline materials," Phil. Mag. **19**, 835–852 (1969).

[18] V. I. Arkhipov, E. V. Emelianova, and G. J. Adriaenssens, "Variable-range hopping within a fluctuating potential landscape," J. Phys.: Condens. Matter **12**, 2021 (2000).

[19] P. M. Borsenberger, L. T. Pautmeier, and H. Bässler, "Nondispersive-to-dispersive charge-transport transition in disordered molecular solids," Phys. Rev. B **46**, 12145 (1992).

[20] E. M. Conwell, "Impurity band conduction in germanium and silicon," Phys. Rev. **103**, 51–60 (1056).

[21] A. Miller and E. Abrahams, "Impurity conduction at low concentrations," Phys. Rev. **120**, 745 (1960).

[22] W. F. Pasveer, J. Cottaar, C. Tanase, R. Coehoorn, P. A. Bobbert, P. W. M. Blom, D. M. de Leeuw, and M. A. J. Michels, "Unified description of charge-carrier mobilities in disordered semiconducting polymers," Phys. Rev. Lett. **94**, 206601 (2005).

[23] H. Houili, E. Tutiš, I. Batistić, and L. Zuppiroli, "Investigation of the charge transport through disordered organic molecular heterojunctions," J. Appl. Phys. **100**, 033702 (2006).

[24] G. Schnönherr, R. Eiermann, and H. Bässler, "Dispersive exciton transport in a hopping system with gaussian energy distribution," Chem. Phys. **52**, 287 (1980).

[25] S. M. Tuladhar, M. Sims, J. Kirkpatrick, R. C. Maher, A. J. Chatten, D. D. C. Bradley, J. Nelson, P. G. Etchegoin, C. B. Nielsen, P. Massiot, W. N. George, and J. H. G. Steinke, "Influence of alkyl chain length on charge transport in symmetrically substituted poly(2,5-dialkoxy- p-phenylenevinylene) polymers," Phys. Rev. B **79**, 035201 (2009).

[26] O. Rubel, S. D. Baranovskii, P. Thomas, and S. Yamasaki, "Concentration dependence of the hopping mobility in disordered organic solids," Phys. Rev. B **69**, 014206 (2004).

[27] D. Monroe, "Hopping in exponential band tails," Phys. Rev. Lett. **54**, 146 (1985).

[28] F. W. Schmidlin, "Theory of trap-controlled transient photoconduction," Phys. Rev. B **16**, 2362 (1977).

[29] C. Tanase, E. J. Meijer, P. W. M. Blom, and D. M. de Leeuw, “Unification of the hole transport in polymeric field–effect transistors and light–emitting diodes,” Phys. Rev. Lett. **91**, 216601 (2003).

[30] V. I. Arkhipov, E. V. Emelianova, and G. J. Adriaenssens, “Effective transport energy versus the energy of most probable jumps in disordered hopping systems,” Phys. Rev. B **64**, 125125 (2001).

[31] A. Rudenko and V. I. Arkhipov, “Drift and diffusion in materials with traps I,” Phil. Mag. B **45**, 177 (1982).

[32] V. I. Arkhipov and A. Rudenko, “Drift and diffusion in materials with traps II,” Phil. Mag. B **45**, 189 (1982).

[33] S. Selberherr, *Analysis and Simulation of Semiconductor Devices* (Springer-Verlag, New York, 1984).

[34] G. A. H. Wetzelaer, L. J. A. Koster, and P. W. M. Blom, “Validity of the Einstein relation in disordered organic semiconductors,” Phys. Rev. Lett. **107**, 06605 (2011).

[35] R. Jankowiak, K. D. Rockwitz, and H. Baessler, “Absorption spectroscopy of amorphous tetracene,” J. Phys. Chem. **87**, 552 (1983).

[36] N. Tessler, Y. Preezant, N. Rappaport, and Y. Roichman, “Charge transport in disordered organic materials and its relevance to thin-film devices: A tutorial review,” Adv. Mater. **21**, 2741 (2009).

[37] T. Kirchartz, B. E. Pieters, J. Kirkpatrick, U. Rau, and J. Nelson, “Recombination via tail states in polythiophene:fullerene solar cells,” Phys. Rev. B **83**, 115209 (2011).

[38] J. C. Blakesley and D. Neher, “The relationship between energetic disorder and open-circuit voltage in bulk heterojunction organic solar-cells,” Phys. Rev. B **84**, 075210 (2011).

[39] C. Deibel and V. Dyakonov, “Polymer–fullerene bulk heterojunction solar cells,” Rep. Prog. Phys. **73**, 096401 (2010).

[40] C. W. Tang, “Two-layer organic photovoltaic cell,” Appl. Phys. Lett. **48**, 183 (1986).

[41] V. I. Arkhipov and H. Baessler, “Exciton dissociation and charge photogeneration in pristine and doped conjugated polymers,” Phys. Stat. Sol. A **201**, 1152 (2004).

[42] Y. Preezant and N. Tessler, “Carrier heating in disordered organic semiconductors,” Phys. Rev. B **74**, 235202 (2006).

[43] L. W. Barbour, R. D. Pensack, M. Hegadorn, S. Arzhantsev, and J. B. Asbury, “Excitation transport and charge separation in an organic photovoltaic material: Watching excitations diffuse to interfaces,” J. Phys. Chem. C **112**, 3926 (2008).

[44] E. Collini and G. D. Scholes, “Coherent intrachain energy migration in a conjugated polymer at room temperature,” Science **323**, 369 (2009).

[45] T. R. Clarke and J. R. Durrant, “Charge photogeneration in organic solar cells,” Chem. Rev. **110**, 6736 (2010).

[46] E. L. Frankevich, A. A. Lymarev, I. Sokolik, F. E. Karasz, S. Blumstengel, R. H. Baughman, and H. H. Hörhold, “Polaron-pair generation in poly(phenylene vinylene),” Phys. Rev. B **46**, 9320 (1992).

[47] J.-L. Brédas, J. E. Norton, J. Cornil, and V. Coropceanu, “Molecular understanding of organic solar cells: The challenges,” Acc. Chem. Res. **42**, 1691 (2009).

[48] J. Behrends, A. Sperlich, A. Schnegg, T.l Biskup, C. Teutloff, K. Lips, V. Dyakonov, and R. Bittl, “Direct detection of photoinduced charge transfer complexes in polymer fullerene blends,” Phys. Rev. B **85**, 125206 (2012).

[49] J. Kern, S. Schwab, C. Deibel, and V. Dyakonov, “Binding energy of singlet excitons and charge transfer complexes in MDMO-PPV:PCBM solar cells,” phys. stat. sol. (RRL) **5**, 254 (2011).

[50] I. A. Howard, R. Mauer, M. Meister, and F. Laquai, “Effect of morphology on ultrafast free carrier generation in polythiophene:fullerene organic solar cells,” J. Am. Chem. Soc. **132**, 14866 (2010).

[51] M. Mingebach, S. Walter, V. Dyakonov, and C. Deibel, “Direct and charge transfer state mediated photogeneration in polymer-fullerene bulk heterojunction solar cells,” Appl. Phys. Lett. **100**, 193302 (2012).

[52] G. Yu, J. Gao, J. C. Hummelen, F. Wudl, and A. J. Heeger, “Polymer photovoltaic cells: enhanced efficiencies via a network of internal donor–acceptor heterojunctions,” Science **270**, 1789 (1995).

[53] F. Padinger, R. S. Rittberger, and N. S. Sariciftci, “Effects of postproduction treatment om plastic solar cells,” Adv. Funct. Mater. **13**, 85 (2003).

[54] S. E. Shaheen, C. J. Brabec, and N. S. Sariciftci, “2.5% efficient organic plastic solar cells,” Appl. Phys. Lett. **78**, 841 (2001).

[55] A. Baumann, J. Lorrmann, C. Deibel, and V. Dyakonov, “Bipolar charge transport in poly(3-hexyl thiophene)/methanofullerene blends: A ratio dependent study,” Appl. Phys. Lett. **93**, 252104 (2008).

[56] J. C. Blakesley and N. C. Greenham, “Charge transfer at polymer-electrode interfaces: The effect of energetic disorder and thermal injection on band bending and open-circuit voltage,” J. Appl. Phys. **106**, 034507 (2009).

[57] J. C. Maxwell, “A dynamical theory of the electromagnetic field,” Phil. Trans. R. Soc. Lond. **155**, 459 (1865).

[58] L. Onsager, “Initial recombination of ions,” Phys. Rev. **54**, 554–557 (1938).

[59] C. L. Braun, “Electric field assisted dissociation of charge transfer states as a mechanism of photocarrier production,” J. Chem. Phys. **80**, 4157–4161 (1984).

[60] L. J. A. Koster, E. C. P. Smits, V. D. Mihailetchi, and P. W. M. Blom, "Device model for the operation of polymer/fullerene bulk heterojunction solar cells," Phys. Rev. B **72**, 085205 (2005).

[61] A. Petersen, A. Ojala, T. Kirchartz, T. A. Wagner, F. Würthner, and U. Rau, "Field-dependent exciton dissociation in organic heterojunction solar cells," Phys. Rev. B **85**, 245208 (2012).

[62] L. J. A. Koster, M. M. Wienk, K. Maturová, and R. A. J. Janssen, "Quantifying bimolecular recombination losses in organic bulk heterojunction solar cells," Adv. Mater. **23**, 1670 (2011).

[63] L. Tzabari and N. Tessler, "Shockley-Read-Hall recombination in P3HT:PCBM solar cells as observed under ultralow light intensities," J. Appl. Phys. **109**, 064501 (2011).

[64] P. Langevin, "Recombinaison et mobilites des ions dans les gaz," Ann. Chim. Phys. **28**, 433 (1903).

[65] J. Kniepert, M. Schubert, J. C. Blakesley, and D. Neher, "Photogeneration and recombination in P3HT/PCBM solar cells probed by time–delayed collection field experiments," J. Phys. Chem. Lett. **2**, 700 (2011).

[66] L. J. A. Koster, V. D. Mihaletchi, and P. W. M. Blom, "Bimolecular recombination in polymer/fullerene bulk heterojunction solar cells," Appl. Phys. Lett. **88**, 052104 (2006).

[67] C. Deibel, A. Wagenpfahl, and V. Dyakonov, "Origin of reduced polaron recombination in organic semiconductor devices," Phys. Rev. B **80**, 075203 (2009).

[68] G. Juška, K. Arlauskas, J. Stuchlik, and R. Osterbacka, "Non-Langevin bimolecular recombination in low-mobility materials; Amorphous and nanocrystalline semiconductors - science and technology - proceedings of the 21st international conference on amorphous and nanocrystalline semiconductors - science and technology," J. Non-Cryst. Sol. **352**, 1167 (2006).

[69] C. G. Shuttle, B. O'Regan, A. M. Ballantyne, J. Nelson, D. D. C. Bradley, J. de Mello, and J. R. Durrant, "Experimental determination of the rate law for charge carrier decay in a polythiophene: Fullerene solar cell," Appl. Phys. Lett. **92**, 093311 (2008).

[70] W. Shockley and W. T. Read, "Statistics of the recombination of holes and electrons," Phys. Rev. **87**, 835 (1952).

[71] R. N. Hall, "Electron–hole recombination in germanium," Phys. Rev. **87**, 387 (1952).

[72] W. Klix, *Numerische Simulation elektronischer Bauelemente* (Der Andere Verlag, 2004).

[73] R. C. I. MacKenzie, C. G. Shuttle, M. L. Chabinyc, and J. Nelson, "Extracting microscopic device parameters from transient photocurrent measurements of P3HT:PCBM solar cells," Adv. Ener. Mater. **2**, 662 (2012).

[74] L. Tzabari and N. Tessler, “Erratum: “shockley read hall recombination in p3ht:pcbm solar cells as observed under ultra low light intensities”,” J. Appl. Phys. **112**, 029902 (2012).

[75] J. Hubin, A. V. Shah, and E. Sauvain, “Effects of dangling bonds on the recombination function in amorphous semiconductors,” Phil. Mag. Lett **66**, 115 (1992).

[76] T. W. Herring, S.-Y. Lee, D. R. McCamey, P. C. Taylor, K. Lips, J. Hu, F. Zhu, A. Madan, and C. Boehme, “Experimental discrimination of geminate and non-geminate recombination in a-Si:H,” Phys. Rev. B **79**, 195205 (2009).

[77] H. Murata, C.D. Merritt, and Z.H. Kafafi, “Emission mechanism in rubrene-doped molecular organic light-emitting diodes: direct carrier recombination at luminescent centers,” IEEE J. Sel. Top. Quantum Electron. **4**, 119 (1998).

[78] G. Juška, K. Genevičius, N. Nekrašas, G. Sliaužys, and G. Dennler, “Trimolecular recombination in polythiophene:fullerene bulk heterojunction solar cells,” Appl. Phys. Lett. **93**, 143303 (2008).

[79] A. Förtig, J. Rauh, V. Dyakonov, and C. Deibel, “Shockley equation parameters of P3HT:PCBM solar cells determined by transient techniques,” Phys. Rev. B **86**, 115302 (2012).

[80] T. Kirchartz and J. Nelson, “Meaning of reaction orders in polymer:fullerene solar cells,” Phys. Rev. B **86**, 165201 (2012).

[81] A. S. Grove, *Physics and Technology of Semiconductor Devices* (John Wiley & Sons, Inc., 1967).

[82] J. Campbell Scott and George G. Malliaras, “Charge injection and recombination at the metalic–organic interface,” Chem. Phys. Lett. **299**, 115 (1999).

[83] R. J. LeVeque, *Finite Difference Methods for Ordinary and Partial Differential Equations* (SIAM, Society for Industrial and Applied Mathematics, 2007).

[84] W. H. Press, S. A. Teukolsky, W. T. Vetterling, and B. P. Flannery, *Numerical Recipes 3rd Edition: The Art of Scientific Computing* (Cambridge University Press, 2007).

[85] M.S. Mock, *Analysis of Mathematical Models of Semiconductor Devices* (Boole Press Limited, 1983).

[86] A. DeMari, “An accurate numerical steady–state one–dimensional solution of the p-n junction,” Solid-State Electron. **11**, 33 (1968).

[87] A. DeMari, “An accurate numerical one–dimensional solution of the p-n junction under arbitrary transient conditions,” Solid-State Electron. **11**, 1021 (1968).

[88] H. K. Gummel, “A self–consistent iterative scheme for one–dimensional steady state transistor calculations,” IEEE Transactions on Electron Devices **11**, 455 (1964).

[89] E. Anderson, Z. Bai, C. Bischof, S. Blackford, J. Demmel, J. Dongarra, J. Du Croz, A. Greenbaum, S. Hammarling, A. McKenney, and D. Sorensen, *LAPACK Users' Guide*, 3rd ed. (Society for Industrial and Applied Mathematics, Philadelphia, PA, 1999).

[90] D. L. Scharfetter and H. K. Gummel, "Large–signal analysis of a silicon read diode oscillator," IEEE Trans. on Electron. Devices **16**, 64 (1969).

[91] J. E. Sutherland and J. R. Hauser, "A computer analysis of heterojunction and graded composition solar cells," IEEE Trans. on Electron. Devices **ED-24**, 365 (1977).

[92] A. Gerrard and J. M. Burch, *Introduction to Matrix Methods in Optics* (Dover Pubn Inc., 1994).

[93] P. Yeh, *Optical Waves in Layered Media* (John Wiley & Sons, 2005).

[94] Z. Knittl, *Optics of Thin Films* (John Wiley & Sons Ltd, London, 1976).

[95] L. A. A. Pettersson, L. S. Roman, and O. Inganäs, "Modeling photocurrent action spectra of photovoltaic devices based on organic thin films," J. Appl. Phys. **86**, 1 (1999).

[96] R. Storn and K. Price, "Differential evolution – a simple and efficient heuristic for global optimization over continuous spaces," J. Global Optim. **11**, 341 (1997).

[97] D. Cheyns, J. Poortmans, P. Heremans, C. Deibel, S. Verlaak, B. P. Rand, and J. Genoe, "Analytical model for the open–circuit voltage and its associated resistance in organic planar heterojunction solar cells," Phys. Rev. B **77**, 165332 (2008).

[98] L. J. A. Koster, V. D. Mihailetchi, R. Ramaker, and P. W. M. Blom, "Light intensity dependence of open–circuit voltage of polymer:fullerene solar cells," Appl. Phys. Lett. **86**, 123509 (2005).

[99] C. J. Brabec, A. Cravino, D. Meissner, N. S. Sariciftci, T. Fromherz, M. T. Rispens, L. Sanchez, and J. C. Hummelen, "Origin of the open circuit voltage of plastic solar cells," Adv. Funct. Mater. **11**, 374 (2001).

[100] M. C. Scharber, D. Mühlbacher, M. Koppe, P. Denk, C. Waldauf, A. J. Heeger, and C. J. Brabec, "Design rules for donors in bulk–heterojunction solar cells — towards 10% energy–conversion efficiency," Adv. Mater. **18**, 789 (2006).

[101] A. Wilke, J. Endres, U. Hörmann, J. Niederhausen, R. Schlesinger, J. Frisch, P. Amsalem, J. Wagner, M. Gruber, A. Opitz, A. Vollmer, W. Brütting, A. Kahn, and N. Koch, "Correlation between interface energetics and open circuit voltage in organic photovoltaic cells," Appl. Phys. Lett. **101**, 233301 (2012).

[102] S. Braun, W. R. Salaneck, and M. Fahlman, "Energy-level alignment at organic/metal and organic/organic interfaces," Adv. Mater. **21**, 1450 (2009).

[103] V. D. Mihailetchi, P. W. M. Blom, J. C. Hummelen, and M. T. Rispens, “Cathode dependence of the open-circuit voltage of polymer:fullerene bulk heterojunction solar cells,” J. Appl. Phys. **94**, 6849 (2003).

[104] K. Vandewal, K. Tvingstedt, A. Gadisa, O. Inganäs, and J. V. Manca, “Relating the open-circuit voltage to interface molecular properties of donor:acceptor bulk heterojunction solar cells,” Phys. Rev. B **81**, 125204 (2010).

[105] C. Deibel, T. Strobel, and V. Dyakonov, “Role of the charge transfer state in organic donor–acceptor solar cells,” Adv. Mater. **22**, 4097 (2010).

[106] K. Vandewal, A. Gadisa, W. D. Oosterbaan, S. Bertho, F. Banishoeib I. Van Severen, L. Lutsen, T. J. Cleij, D. Vanderzande, and J. V. Manca, “The relation between open-circuit voltage and the onset of photocurrent generation by charge-transfer absorption in polymer: Fullerene bulk heterojunction solar cells,” Adv. Funct. Mater. **18**, 2064 (2008).

[107] C. M. Ramsdale, J. A. Barker, A. C. Arias, J. D. MacKenzie, R. H. Friend, and N. C. Greenham, “The origin of the open–circuit voltage in polyfluorene–based photovoltaic devices,” J. Appl. Phys. **92**, 4266 (2002).

[108] A. Förtig, A. Wagenpfahl, T. Gerbich, D. Cheyns, V. Dyakonov, and C. Deibel, “Nongeminate recombination in planar and bulk heterojunction organic solar cells,” Adv. Ener. Mater. **2**, 1483 (2012).

[109] D. Rauh, A. Wagenpfahl, C. Deibel, and V. Dyakonov, “Relation of open circuit voltage to charge carrier density in organic bulk heterojunction solar cells,” Appl. Phys. Lett. **98**, 133301 (2011).

[110] B. Rand, D. Burk, and S. Forrest, “Offset energies at organic semiconductor heterojunctions and their influence on the open-circuit voltage of thin-film solar cells,” Phys. Rev. B **75**, 115327 (2007).

[111] D. Veldman, S. C. J. Meskers, and R. A. J. Janssen, “The energy of charge–transfer states in electron donor–acceptor blends: Insight into the energy losses in organic solar cells,” Adv. Funct. Mater. **19**, 1939 (2009).

[112] C. Deibel, T. Strobel, and V. Dyakonov, “Origin of the efficient polaron pair dissociation in polymer–fullerene blends,” Phys. Rev. Lett. **103**, 036402 (2009).

[113] K. Vandewal, K. Tvingstedt, A. Gadisa, O. Inganäs, and J. V. Mancad, “On the origin of the open–circuit voltage of polymer–fullerene solar cells,” Nature Mater. **8**, 904 (2009).

[114] Z.-L. Guan, J. B. Kim, H. Wang, C. Jaye, D. A. Fischer, Y.-L. Loo, and A. Kahn, “Direct determination of the electronic structure of the poly(3-hexylthiophene):phenyl-[6,6]-c61 butyric acid methyl ester blend,” Org. Electron. **11**, Direct determination of the electronic structure of the poly(3–hexylthiophene):phenyl–[6,6]–C61 butyric acid methyl ester blend (2010).

[115] I. L. Eisgruber, J. E. Granata, J. R. Sites, J. Hou, and J. Kessler, "Blue-photon modification of nonstandard diode barrier in $CuInSe_2$ solar cells," Solar Energy Materials and Solar Cells **53**, 367–377 (1998).

[116] A. Kumar, S. Sista, and Y. Yang, "Dipole induced anomalous S-shape I-V curves in polymer solar cells," J. Appl. Phys. **105**, 094512 (2009).

[117] C. Uhrich, R. Schueppel, A. Petrich, M. Pfeiffer, K. Leo, E. Brier, P. Kilickiran, and P. Baeuerlel, "Organic thin–film photovoltaic cells based on oligothiophenes with reduced bandgap," Adv. Funct. Mater. **17**, 2991 (2007).

[118] K. Schulze, C. Uhrich, R. Schüppel, K. Leo, M. Pfeiffer, E. Brier, E. Reinold, and P. Bäuerle, "Efficient vacuum–deposited organic solar cells based on a new low–bandgap oligothiophene and fullerene C60s," Adv. Mater. **18**, 2872 (2006).

[119] R. Häusermann, E. Knapp, M. Moos, N. A. Reinke, T. Flatz, and B. Ruhstaller, "Coupled optoelectronic simulation of organic bulk–heterojunction solar cells: Parameter extraction and sensitivity analysis," J. Appl. Phys. **106**, 104507 (2009).

[120] T. Kirchartz, J. Mattheis, and U. Rau, "Detailed balance theory of excitonic and bulk heterojunction solar cells," Phys. Rev. B **78**, 235320 (2008).

[121] A. Wagenpfahl, C. Deibel, and V. Dyakonov, "Organic solar cell efficiencies under the aspect of reduced surface recombination velocities," IEEE J. Sel. Top. Quantum Electron. **16**, 1759 (2010).

[122] D. W. Sievers, V. Shrotriya, and Yang Yang, "Modeling optical effects and thickness dependent current in polymer bulk–heterojunction solar cells," J. Appl. Phys. **100**, 114509 (2006).

[123] S. V. Novikov, D. H. Dunlap, V. M. Kenkre, P. E. Parris, and A. V. Vannikov, "Essential role of correlations in governing charge transport in disordered organic materials," Phys. Rev. Lett. **81**, 4472 (1998).

[124] S. Lacic and O. Inganäs, "Modeling electrical transport in blend heterojunction organic solar cells," J. Appl. Phys. **97**, 124901 (2005).

[125] G. A. Buxton and N. Clarke, "Computer simulation of polymer solar cells," Modelling Simul. Mater. Sci. Eng. **15**, 13 (2007).

[126] J. S. Kim, M. Granström, R. H. Friend, N. Johansson, W. R. Salaneck, N. Johansson, W. R. Salaneck, and F. Caciallia, "Indium tin oxide treatments for single- and double-layer polymeric light-emitting diodes: The relation between the anode physical, chemical, and morphological properties and the device performance," J. Appl. Phys. **84**, 6859 (1998).

[127] K. L. Puvis, G. Lu, J. Schwartz, and S. L. Bernaske, "Surface characterization and modification of indium tin oxide in ultrahigh vacuum," J. Am. Chem. Soc. **122**, 1808 (2000).

[128] V. M. Bermudez, A. D. Berry, H. Kim, and Alberto Pique, "Functionalization of indium tin oxide," Langmuir **22**, 11113 (2006).

[129] A. Wagenpfahl, D. Rauh, C. Deibel, and V. Dyakonov, "S-shaped current voltage characteristics of organic bulk heterojunction solar devices," Phys. Rev. B **82**, 115306 (2010).

[130] D. Rauh, *Impact of Polaron Recombination and Doping on Organic Solar Cells*, Ph.D. thesis, Fakultat für Physik und Astronomie, Universität Würzburg (2013).

[131] N. Persson, H. Arwin, and O. Inganas, "Optical optimization of polyfluorene-fullerene blend photodiodes," J. Appl. Phys. **97**, 034503 (2005).

[132] C. Uhrich, D. Wynands, S. Olthof, M. K. Riede, K. Leo, S. Sonntag, B. Maennig, and M. Pfeiffer, "Origin of open circuit voltage in planar and bulk heterojunction organic thin–film photovoltaics depending on doped transport layers," J. Appl. Phys. **104**, 043107 (2008).

[133] V. D. Mihailetchi, P. W. M. Blom, J. C. Hummelen, and M. T. Rispens, "Cathode dependence of the open–circuit voltage of polymer:fullerene bulk heterojunction solar cells," J. Appl. Phys. **94**, 6849 (2003).

[134] B. Bohnenbuck, E. von Hauff, J. Parisi, C. Deibel, and V. Dyakonov, "Current-limiting mechanisms in polymer diodes," J. Appl. Phys. **99**, 024506 (2006).

[135] V. D. Mihailetchi, J. Wildeman, and P. W. M. Blom, "Space–charge limited photocurrent," Phys. Rev. Lett. **94**, 126602 (2005).

[136] V. I. Arkhipov, P. Heremans, E. V. Emelianova, and G. J. Adriaenssens, "Space–charge–limited currents in materials with gaussian energy distributions of localized states," Appl. Phys. Lett. **79**, 4154 (2001).

[137] S. C. Jain, W. Geens, A. Mehra, V. Kumar, T. Aernouts, J. Poortmans, R. Mertens, and M. Willander, "Injection- and space charge limited–currents in doped conducting organic materials," J. Appl. Phys. **89**, 3804 (2001).

[138] T. A. Skotheim (Ed.), *Handbook of Conducting Polymers* (Dekker, New York, 1986).

[139] Martin A Green, Keith Emery, Yoshihiro Hishikawa, Wilhelm Warta, and Ewan D Dunlop, "Solar cell efficiency tables (version 39)," Prog. Photovolt. **20**, 12–20 (2012).

[140] W. Shockley and J. J. Queisser, "Detailed balance limit of efficiency of p–n junction solar cells," J. Appl. Phys. **32**, 510 (1961).

[141] M. M. Mandoc, L. J. A. Koster, and P. W. M. Blom, "Optimum charge carrier mobility in organic solar cells," Appl. Phys. Lett. **90**, 133504 (2007).

[142] C. Deibel, A. Baumann, J. Lorrmann, and V. Dyakonov, "Polaron pair dissociation and polaron recombination in polymer: Fullerene solar cells," in *Mat. Res. Soc. Symp. Proc.* (2008).

[143] H.-J. Lewerenz and H. Jungblut, *Photovoltaik: Grundlagen und Anwendungen* (Springer, Berlin, 1995).

[144] C. Brabec, U. Scherf, and V. Dyakonov, *Organic Photovoltaics: Materials, Device Physics, and Manufacturing Technologies* (Wiley-VCH Verlag, 2008).

[145] T. Kirchartz, B. E. Pieters, K. Taretto, and U. Rau, “Electro–optical modeling of bulk heterojunction solar cells,” J. Appl. Phys. **104**, 094513 (2008).

[146] C. Deibel, A. Wagenpfahl, and V. Dyakonov, “Influence of charge carrier mobility on the performance of organic solar cells,” phys. stat. sol. (RRL) **2**, 175 (2008).

[147] C. Deibel, A. Baumann, and V. Dyakonov, “Polaron recombination in pristine and annealed bulk heterojunction solar cells,” Appl. Phys. Lett. **93**, 163303 (2008).

[148] Z. E. Ooi, R. Jin, J. Huang, Y. F. Loo, A. Sellinger, and J. C. de Mello, “On the pseudo-symmetric current–voltage response of bulk heterojunction solar cells,” J. Mater. Chem. **18**, 1605 (2008).

[149] V. D. Mihailetchi, L. J. A. Koster, and P. W. M. Blom, “Effect of metal electrodes on the performance of polymer:fullerene bulk heterojunction solar cells,” Appl. Phys. Lett. **85**, 970 (2004).

[150] G. J. Adriaenssens and V. I. Arkhipov, “Non-Langevin recombination in disordered materials with random potential distributions,” Sol. State Comm. **103**, 541 (1997).

[151] A. Baumann, J. Lorrmann, D. Rauh, C. Deibel, and V. Dyakonov, “A new approach of probing the mobility and lifetime of photogenerated charge carriers in organic solar cells under real operating conditions,” Adv. Mater. **24**, 4281 (2012).

[152] M. Limpinsel, A. Wagenpfahl, M. Mingebach, C. Deibel, and V. Dyakonov, “Photocurrent in bulk heterojunction solar cells,” Phys. Rev. B **81**, 085203 (2010).

[153] G. A. Buxton and N. Clarke, “Predicting structure and property relations in polymeric photovoltaic devices,” Phys. Rev. B **74**, 085207 (2006).

[154] J. Szmytkowski, “Analysis of the image force effects on the recombination at the donor–acceptor interface in organic bulk heterojunction solar cells,” Chem. Phys. Lett. **470**, 123 (2009).

[155] C. Groves and N. C. Greenham, “Bimolecular recombination in polymer electronic devices,” Phys. Rev. B **78**, 155205 (2008).

[156] J. Schafferhans, A. Baumann, A. Wagenpfahl, C. Deibel, and V. Dyakonov, “Oxygen doping of P3HT:PCBM blends: Influence on trap states, charge carrier mobility and solar cell performance,” Org. Electron. **11**, 1693 (2010).

[157] J. Schafferhans, A. Baumann, C. Deibel, and V. Dyakonov, “Trap distribution and the impact of oxygen–induced traps on the charge transport in poly(3-hexylthiophene),” Appl. Phys. Lett. **92**, 093303 (2008).

[158] J. Bisquert and V. S. Vikhrenko, “Interpretation of the time constants measured by kinetic techniques in nanostructured semiconductor electrodes and dye–sensitized solar cells,” J. Phys. Chem. B **108**, 2313 (2004).

[159] R. A. Street, S. Cowan, and A. J. Heeger, “Experimental test for geminate recombination applied to organic solar cells,” Phys. Rev. B **82**, 121301(R) (2010).

[160] C. Deibel and A. Wagenpfahl, “Comment on “interface state recombination in organic solar cells”,” Phys. Rev. B **82**, 207301 (2010).

[161] R. A. Street, “Reply to “comment on ‘interface state recombination in organic solar cells’ ”,” Phys. Rev. B **82**, 207302 (2010).

Part III.

Appendix

A. List of Abbreviations

Abbreviation	Description
a-Si	amorphous silicon
Ag	silver
Al	aluminum
AM1.5	sun spectrum on earth filtered by 1.5 atmospheres
BB	band bending
BCP	bathocuproine
BHJ	bulk heterojunction (solar cell)
bisPCBM	bis-[6,6]-phenyl C61 butyric acid methyl ester
Ca	calcium
CELIV	charge extraction by linearly increasing voltage
CIGS	copper indium gallium diselenide
CT	charge transfer
CuPc	copper phthalocyanine
DOS	density of states
GaAs	gallium arsenide
GDM	Gaussian disorder model
GDOS	Gaussian density of states
HOMO	highest occupied molecular orbital
ITO	indium tin oxide
LUMO	lowest unoccupied molecular orbital
LCAO	linear combination of atomic orbitals
MDMO:PPV	poly(2-methoxy-5(3’,7’-dimethylloctyloxy)-1,4-phenylene-vinylene)
MTR	multiple trapping and release
OLED	organic light emitting diode
P3HT	poly(3-hexylthiophene)
$PC_{61}BM$	[6,6]-phenyl C61 butyric acid methyl ester
$PC_{71}BM$	[6,6]-phenyl C71 butyric acid methyl ester
PCDTBT	Poly[[9-(1-octylnonyl)-9H-carbazole-2,7-diyl]-2,5-thiophenediyl-2,1,3-benzothiadiazole-4,7-diyl-2,5-thiophenediyl]
PEDOT:PSS	poly(3,4-ethylenedioxythiophene):(polystyrenesulfonate)
PHJ	planar heterojunction

Abbreviation	Description
PPV	poly(p-phenylenevinylene)
SCLC	space charge limited current
Si	silicon
SRH	Shockley-Read-Hall recombination
TCO	transparent conducting oxide
VRH	variable range hopping

B. List of Symbols

Symbol	Description
α	angle of light incidence
a	polaron pair binding distance
b	argument of Bessel function
$B(x)$	Bernoulli function
c	speed of light
$C(x)$	effective doping concentration
$\delta\Psi$	error of electric potential
$\delta\mathrm{n}$	error of electron density
$\delta\mathrm{p}$	error of hole density
d	layer thickness
D_n	electron diffusion coefficient
D_p	hole diffusion coefficient
D_x	exciton diffusion coefficient
ε	convergence criterion
ε_0	dielectric permittivity of vacuum
ε_r	relative permittivity
η	power conversion efficiency
E	energy
E_b	Coulomb binding energy
E_F	Fermi energy
E_{Fn}	quasi-Fermi energy electrons
E_{Fp}	quasi-Fermi energy holes
E_i	intrinsic Fermi energy or specific energetic state
E_j^+	electric field component of light propagating from left to right through layer j
E_j^-	electric field component of light propagating from right to left through layer j
E_{loss}	lost energy due to band bending
E_g	(effective) band gap
E_{tr}	transport energy
ζ	Langevin reduction factor

Symbol	Description
f_{FD}	Fermi-Dirac distribution
F	electric field
FF	fill factor
γ	Langevin recombination factor
G	generation rate
h	lattice spacing
I_{ij}	transfer integral
$\boldsymbol{I}_{ij}$	interface matrix
J	total current density
J_1	first order Bessel function
J_{mpp}	current at maximum power point
J_n	electron current density
J_{oc}	total current density at open circuit conditions
J_{surf}	surface recombination current
J_p	hole current density
J_{sc}	short circuit current
κ	extinction coefficient
k	recombination rate
k_B	Boltzmann constant
k_D	dissociation rate
k_F	decay rate
k_x	decay rate of excitons
λ	wavelength
$\lambda + 1$	recombination order
L	active layer thickness
$\boldsymbol{L}_i$	layer matrix
μ_{crit}	critical mobility
μ_n	electron mobility
μ_p	hole mobility
n	electron density
$\tilde{n}$	complex refraction index
n'	(real) refraction index
n_c	conductive electrons
N_c	effective density of states of the conduction band
n_{ext}	extracted (averaged) charge carrier density
n_i	intrinsic charge carrier density
n_{inj}	injected electron density at interface

Symbol	Description
n_n	electron density at cathode
n_p	electron density at anode
n_t	trapped electrons
n_{th}	thermally activated electron density
N_t	amount of trap states
N_v	effective density of states of the valance band
Φ_c	critical injection barrier
Φ_n	injection barrier at cathode
Φ_p	injection barrier at anode
Ψ	electrical potential
φ_n	quasi-Fermi potential electrons
φ_p	quasi-Fermi potential holes
p	hole density
p_{inj}	injected hole density at interface
p_n	hole density at cathode
p_p	hole density at anode
p_{th}	thermally activated hole density
P	generation probability
P_{mpp}	maximum power (point) of a solar cell
q	elementary charge
Q_j	number of absorbed photons of one wavelength
r	distance between two charges
r_c	Coulomb binding radius
r_{ij}	Fresnel reflection coefficient
R	recombination rate
R_{ij}	spatial distance
σ	disorder parameter of Gaussian distribution
Σ	spatial disorder
$\boldsymbol{S}$	scattering matrix
S_{min}	minority surface recombination velocity
S_{maj}	majority surface recombination velocity
S_n	electron surface recombination velocity
S_p	hole surface recombination velocity
τ	lifetime
τ_x	exciton lifetime
ϑ	ratio between trapped and free electrons
Θ_n	band parameter LUMO

Symbol	Description
Θ_p	band parameter HOMO
t	time
t_{ij}	Fresnel transmission coefficient
T	temperature
U	net recombination rate
v_{th}	thermal velocity
V_{bi}	built-in potential
V_{mpp}	voltage at maximum power point
V_{oc}	open circuit voltage
x	spatial position
x_{int}	spatial location of the heterointerface (PHJ) or of equal electron and hole concentrations (BHJ)
X	exciton density
ζ	Langevin reduction factor

C. List of Publications

Refereed articles

1. Influence of charge carrier mobility on the performance of organic solar cells, C. Deibel, **A. Wagenpfahl**, and V. Dyakonov, *phys. stat. sol. (RRL)*, **2**, 175 (2008).

2. Origin of reduced polaron recombination in organic semiconductor devices, C. Deibel, **A. Wagenpfahl**, and V. Dyakonov, *Phys. Rev. B*, **80**, 075203 (2009).

3. Polaron recombination in pristine and annealed bulk heterojunction solar cells, C. Deibel, A. Baumann, **A. Wagenpfahl**, and V. Dyakonov, *Synth. Met.*, **159**, 2345 (2009).

4. Photocurrent in bulk heterojunction solar cells, M. Limpinsel, **A. Wagenpfahl**, M. Mingebach, C. Deibel and V. Dyakonov, *Phys. Rev. B*, **81**, 085203 (2010).

5. S-shaped current-voltage characteristics of organic solar devices, **A. Wagenpfahl**, D. Rauh, M. Binder, C. Deibel, and V. Dyakonov, *Phys. Rev. B*, **82**, 115306 (2010).

6. Oxygen doping of P3HT:PCBM blends: Influence on trap states, charge carrier mobility and solar cell performance, J. Schafferhans, A. Baumann, **A. Wagenpfahl**, C. Deibel, and V. Dyakonov, *Org. Electron.*, **11**, 1693 (2010).

7. Organic solar cell efficiencies under the aspect of reduced surface recombination velocities, **A. Wagenpfahl**, C. Deibel, and V. Dyakonov, *IEEE J. Sel. Top. Quantum Electron.*, **16**, 1759 (2010).

8. Comment on „Interface state recombination in organic solar cells“, C. Deibel, and **A. Wagenpfahl**, *Phys. Rev. B*, **82**, 207301 (2010).

9. Relation of open circuit voltage to charge carrier density in organic bulk heterojunction solar cells, D. Rauh, **A. Wagenpfahl**, C. Deibel, and V. Dyakonov, *Appl. Phys. Lett.*, **98**, 133301 (2011).

10. Printed paper photovoltaic cells, A. Hübler, B. Trnovec, T. Zillger, M. Ali, N. Wetzold, M. Mingebach, **A. Wagenpfahl**, C. Deibel, and V. Dyakonov, *Adv. Ener. Mat.*, **1**, 1018 (2011).

11. Bimolecular Recombination in Planar and Bulk Heterojunction Organic Solar Cells, A. Förtig, **A. Wagenpfahl**, T. Gerbich, D. Cheyns, V. Dyakonov, and C. Deibel, *Adv. Ener. Mat.*, **2**, 1483 (2012).

Conference talks

1. Numerical simulation on S-shaped organic bulk–heterojunction solar cell current–voltage characteristics, **A. Wagenpfahl**, D. Rauh, M. Binder, C. Deibel, and V.Dyakonov, *International Simulation Workshop on Organic Electronics and Photovoltaics*, Winterthur, Switzerland (2010).
2. Numerical simulation on S-shaped organic bulk–heterojunction solar cell current–voltage characteristics, **A. Wagenpfahl**, D. Rauh, M. Binder, C. Deibel, and V.Dyakonov, *DPG Spring Meeting 2010*, Regensburg, Germany (2010).
3. Recombination processes in disordered organic bulk–heterojunction solar cells, **A. Wagenpfahl**, V. Dyakonov, and C. Deibel, *MRS Fall Meeting*, Boston, USA (2011).
4. Recombination processes in disordered organic bulk–heterojunction solar cells, **A. Wagenpfahl**, V. Dyakonov, and C. Deibel, *DPG Spring Meeting*, Berlin, Germany (2012).

Poster presentations

1. Numerical simulation of organic bulk–heterojunction solar cells, **A. Wagenpfahl**, C. Deibel, and V. Dyakonov, *DPG Spring Meeting*, Berlin, Germany (2008).
2. Surface effects on organic solar cell characteristics, **A. Wagenpfahl**, C. Deibel, and V. Dyakonov, *DPG Spring Meeting*, Dresden, Germany (2009).
3. Simulations of the impact of energetic disorder on the charge carrier recombination, **A. Wagenpfahl**, J. Lorrmann, M. Ruf and, C. Deibel, *2nd International Conference Organic Photovolatics*, Würzburg, Germany (2011).

Conference proceedings

1. Implications of a reduced polaron recombination on polymer:fullerene solar cells, C. Deibel, **A. Wagenpfahl**, A. Baumann, and V. Dyakonov, *Proc. SPIE*, **7052**, 70520N (2008).
2. Bulk vs. surface recombination in polymer-fullerene solar cells, C. Deibel, T. Strobel, **A. Wagenpfahl**, M. Limpinsel, M. Mingebach, and V. Dyakonov, *Proc. SPIE*, **7416**, 74160Q (2009).

Danksagung

An dieser Stelle möchte ich mich ganz herzlich bei Allen bedanken, die mich während meiner Zeit beruflich wie privat begleitet haben und so zum erfolgreichen Gelingen dieser Arbeit beigetragen haben. Mein ganz besonderer Dank gilt hierbei:

- Prof. Dr. Vladimir Dyakonov für die Ermöglichung dieser Arbeit am Lehrstuhl für Experimentelle Physik VI, für die aufwendige Erstellung zahlreicher Gutachten sowie seine sehr freundliche und äußerst hilfreiche Unterstützung bei der Korrektur dieser Arbeit. Ohne seine kompetente Unterstützung wäre mein Auslandsaufenhalt nicht möglich gewesen und ich freue mich bereits heute auf eine hoffentlich interessante Verteidigung dieser Arbeit.

- Prof. Dr. Jean Geurts, der sich freundlicherweise als Zweitgutachter zur Verfügung gestellt hat.

- Prof. Dr. Karl Mannheim dafür, dass er sehr kurzfristig als dritter Prüfer eingesprungen ist.

- PD Dr. Carsten Deibel für die exzellente Unterstützung und Betreuung über die letzten Jahre, nicht nur in physikalischen Fragen. Nicht zuletzt dürfen auch seine großen Bemühungen und seine Verbindungen für meinen Amerikaaufenthalt nicht vergessen werden.

- Prof. Dr. Mike D. McGehee für seine großzügige Gastfreundschaft und dafür, dass ich in Stanford sehr viel über Gruppenführung und taktische Ziele wissenschaftlicher Arbeit von ihm lernen durfte.

- Prof. Dr. Jens Plaum für zahlreiche interessante und spannende Diskussionen.

- Meinen Bürokollegen mit denen ich in den letzten Jahren viel Freude im In- und Ausland haben durfte, insbesondere Jens Lorrmann, Julien Gorentflot und Moritz Liedkte. Mein besonderer Dank gilt dabei Markus Mingebach, Andreas Baumann und Alexander Förtig die viel Zeit investiert haben diese Arbeit Korrektur zu lesen.

- Dave Sills für die schnelle Rettung in der Not und viele Verbesserungsvorschläge die nicht jeder hätte machen können.

- Christoph Wick für die aufwendige Programmierung der graphischen Benutzeroberfläche der Simulation.

- Dem gesamten Lehrstuhl der EP VI für die ausgezeichnete Arbeitsatmosphäre und den vielen lustigen Weihnachts- und Grillfeiern.

- Allen Freunden und Bekannten, die bislang nicht namentlich erwähnt wurden.

Auch darf meine Mutter nicht unerwähnt bleiben, die mich in der letzten Zeit oftmals mit Essen versorgt hat und mir so das Schreiben dieser Arbeit angenehmer gestaltet hat. Nicht zuletzt möchte ich auch meiner Freundin Elke danken, die mich grade und besonders in dieser schwierigen Zeit immer wieder liebevoll unterstützt hat und mich auf den richtigen Weg zurückgebracht hat. Dir habe ich wirklich viel zu verdanken.

Eidesstattliche Erklärung

Erklärung gemäß § 5 Abs. 2 Ziff. 2, 3 und 5
der Promotionsordnung
in der Fassung vom 22. September 2003
der Fakultät für Physik und Astronomie
der Julius-Maximilians-Universität Würzburg

Hiermit versichere ich an Eides statt, dass ich die vorgelegte Dissertation selbstständig und ohne Hilfe Dritter angefertigt habe. Neben den angegebenen Quellen wurden keine weitern Quellen und Hilfsmittel benutzt.

Die vorgelegte Dissertation wurde bisher weder vollständig noch in Teilen einer anderen Hochschule mit dem Ziel einen akademischen Grad zu erwerben vorgelegt.

Am 17. September 2008 wurde mir von der Julius-Maximilians-Universität Würzburg der akademische Grad „Diplom-Physiker Univ.“ verliehen. Weitere akademische Grade habe ich weder erworben noch zu erwerben versucht.

Die vorgelegte Dissertation wurde von Prof. Dr. Vladimir Dyakonov betreut.

Würzburg, den 24. Juni 2013

Alexander Johannes Wagenpfahl